II/VI metastable sulphides: Fundamental studies of MBE growth, characterization and nanostructure formation.

By

Richard T Moug BSc (Hons.)

Submitted for the degree of Doctor of Philosophy

Heriot-Watt University

School of Engineering and Physical Sciences

August 2009

Abstract

This thesis presents a fundamental study of II-VI metastable sulfides. Details of the growth by Molecular Beam Epitaxy (MBE) and characterization of CrS,ZnS,MgS, and ZnMgSSe structures on GaP and GaAs substrates are presented.

Multilayer structures of ZnS/CrS and ZnMgS/CrS were grown on GaP substrates and characterized using X-ray interference. Asymmetric X-ray spectra indicated the presence of mosaic structure in the layers. A discussion on solutions to the disordered surface is presented. Superlattice structures were designed to contain 100Å of CrS. These samples were sent to the Polish academy of science for further analysis of magnetic properties.

The surface morphology of zinc blende MgS layers grown on ZnSe buffer layers has been investigated by AFM. Nanowire formation is studied as a function of flux ratio and MgS layer thickness. Typical wire dimensions were found to be 0.6μm (length), 900Å (width), and 20Å (height). The method of wire formation is consistent with an anisotropic relaxation of the MgS layer by mismatch dislocations leading to a surface instability by the Asaro-Tiller-Grinfield mechanism.

RHEED patterns from zincblende MgS (100) surfaces have been observed during growth, annealing and both during and after irradiation of the surface with an Mg flux. The results are compatible with the c(2x2) surface being formed from a ZnMgS alloy which converts to a pure MgS 4x1 reconstruction on Mg irradiation.

Samples containing ZnMgSSe alloy were grown and analyzed by X-ray Interference. The alloy composition was found to be $Zn_{0.20}Mg_{0.80}S_{0.64}Se_{0.36}$. Samples with this composition are shown to be single phase using transmission electron microscopy. Structures with $Zn_{0.20}Mg_{0.80}S_{0.64}Se_{0.36}$ barriers were grown with ZnSe quantum wells and CdSe quantum dots, and showed good quantum confinement. The incorporation of $Zn_{0.20}Mg_{0.80}S_{0.64}Se_{0.36}$ in an epitaxial lift off technology has also been demonstrated.

Acknowledgments

I would like to thank my supervisor Kevin Prior for his expert advice and support over the last 4 years. The enthusiasm Kevin has for the subject has meant that it has been a pleasure to be part of the Heriot-Watt MBE group.

Thanks also to Richard Warburton and Arran Curran of the Nano-Optics group at Heriot-Watt for supplying the PL measurements presented in this thesis.

My gratitude extends to the Departamento de Cienciadelos Materialese Ingeniería Metalúrgica y Química Inorgánica, Universidad de Cádiz for their TEM analysis of my structures.

One important member of the MBE group who has continually encouraged me through those difficult down times is our head R.A, Christine Bradford. Thank you for all your advice and for ensuring I had a smile on my face (most of the time). Our newest member Ian Davidson also requires thanks for continuing the PL work started by Arran Curran.

Office member's old and new thank you for ensuring that I never make the mistake of leaving my PC unlocked when leaving the room. Thanks to Spyros for making sure the office smells like Starbucks, thanks to Ian for providing some of the funniest music out, and thanks to Keith for those extremely sparse moments of comedy gold.

My three closest friends Fiona Sutherland, Ryan Warburton, and Christopher Sprought have been incredibly supportive during the entire span of this PhD. They have encouraged when needed and celebrated when required. Special thanks are needed for Fiona, my longest standing friend, for still putting up with me especially during this write up.

Thanks is also required to the Special Operation Group members Def Munky, XIII Munky, Irn Munky, and Disco King for making sure I rose to the Call of Duty, for keeping my aims true and my in targets in sight……. Hoorah!

And finally to my parents Elli and Terry, you have supported me so much over the years so all I have to say is thanks for not giving up!

Table of Contents

List of Figures.

Chapter 1

Introduction.

1.1 MBE Growth.

Developed in the late 1960's [1], Molecular Beam Epitaxy (MBE) has progressed to state of the art growth facilities used for industrial production of high quality semiconductor III-V devices. The use of elemental sources, the high monolayer precision attainable, and *in situ* monitoring techniques such as RHEED (Reflection High Energy Electron Diffraction) have been key factors in the success of MBE. Improvements on the original MBE capabilities include: multiple 6" holding platens, fully automatic wafer transfer for high throughput levels, high volume effusion cells, long up-times and excellent run-to-run repeatability.

Since its development numerous studies have focused on the industrial capabilities of MBE; improving yield, reducing cost, and increasing efficiency. One of the key advantages of MBE growth is that it utilises high purity, elemental sources. This allows for previously unexplored materials to be quickly and easily investigated.

The majority of MBE research is focused on the development of III-V materials and structures with the successful, commercial production of visible-Infra Red, Light Emitting Diodes (LEDs) and Laser Diodes (LDs). The emission wavelength of these devices is however limited to ~ 600-2000 nm due to the band gaps of the III-V materials. By investigating wide band gap II-VI materials, emission wavelength at the Blue-UV spectrum are obtainable. Because of this in the 1980's a large amount of research was dedicated to the fabrication of II-VI based semiconductor devices culminating with the demonstration of room temperature continuous wave blue lasers [2].

1.2 Overview of II-VI thin film growth.

One of the initial areas of interest for II-VI semiconductors was the optimisation of ZnSe epilayers grown on GaAs substrates [3]. Subsequent studies involved the development of ZnSe based LED's [4] and LD's [5], however, inherent problems with p-type doping hindered any significant progress. Point defects and difficulties with ohmic contacts further complicated the realisation of commercially viable devices [6,7]. Commercial research into II-VI optoelectronic devices diminished with the introduction of wide-bandgap GaN based structures that overcame the inherent issues associated with II-VI devices.

Although the realisation of II-VI based optoelectronic devices did not occur, many groups remained in the field of II-VI research. The majority of research today is involved in the study of the spectroscopic properties of II-VI nanostructures. The wide bandgaps associated with materials like ZnSe provide excellent exciton confinement when incorporated into low dimensional structures such as Quantum Wells (QW) and Quantum Dots (QD) [8,9].

Interesting physical phenomena associated with II-VI materials have led to other active areas of interest. Spintronics and dilute magnetic semiconductors (DMS) are two such areas [10]. Using transition metal (Cr, Mn, Fe) containing materials the electron spin state can be manipulated with the possibility of providing devices that have reduced power consumption with higher data transport and storage.

1.3 II-VI Research at Heriot-Watt University.

Research at Heriot-Watt started in 1988 with the donation of an MBE machine from British Telecom. The HW MBE group were one of the first in Europe to demonstrate a 77k ZnSe/ZnCdSe blue laser in 1992 [11].

Work in recent years has been focused on the development of II-VI metastable sulphides grown on both GaAs and GaP substrates [12]. The use of compound ZnS has allowed the growth of metastable MgS in the zinc blende structure [13] and subsequently transition metal sulphides such as MnS, MnCrS, and CrS have been investigated with the possibility of demonstrating ferromagnetic and anti-ferromagnetic

properties [14]. Intense PL (photoluminescence) emission has been demonstrated in both MgS/ZnSe and MgS/CdSe low dimensional structures [8,9]. Experimental studies on MgS have led to new II-VI technologies being developed such as a novel lift off technique in order to investigate room temperature polaritons [15].

Current research at HW is involved in developing these well studied materials into useful structures, for example a spin current detector. However, work on new materials continues with an appraisal of the use of ZnMgSSe as a direct replacement for MgS in wide band gap nanostructures. This work is covered in this thesis and is presented in more detail in chapter 5.

1.4 Heriot-Watt MBE system.

The MBE system at Heriot-Watt consists of two Vacuum Generators V80H growth chambers separated by a preparation chamber and denoted HWA and HWC. Chamber HWC is a replacement for HWB which was removed in summer 2007. Schematic diagrams of the two chambers are shown in figure 1.1. and 1.2

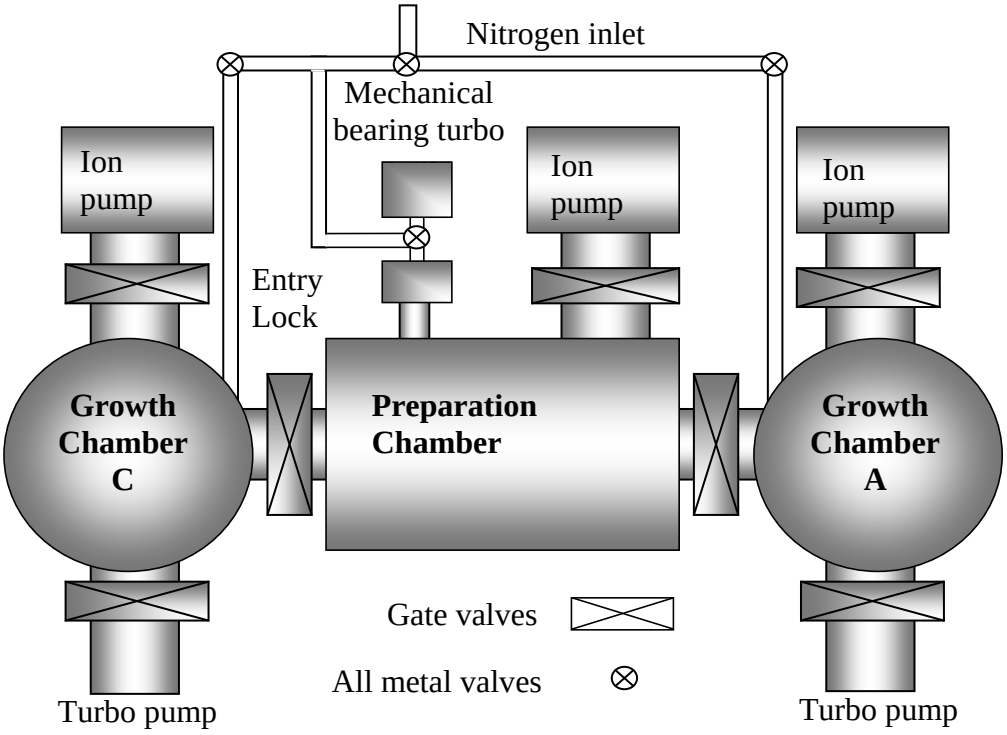

Figure 1.1 *Top elevation of the HW V80H MBE system highlighting the external components such as the ion pumps and the nitrogen venting inlet.*

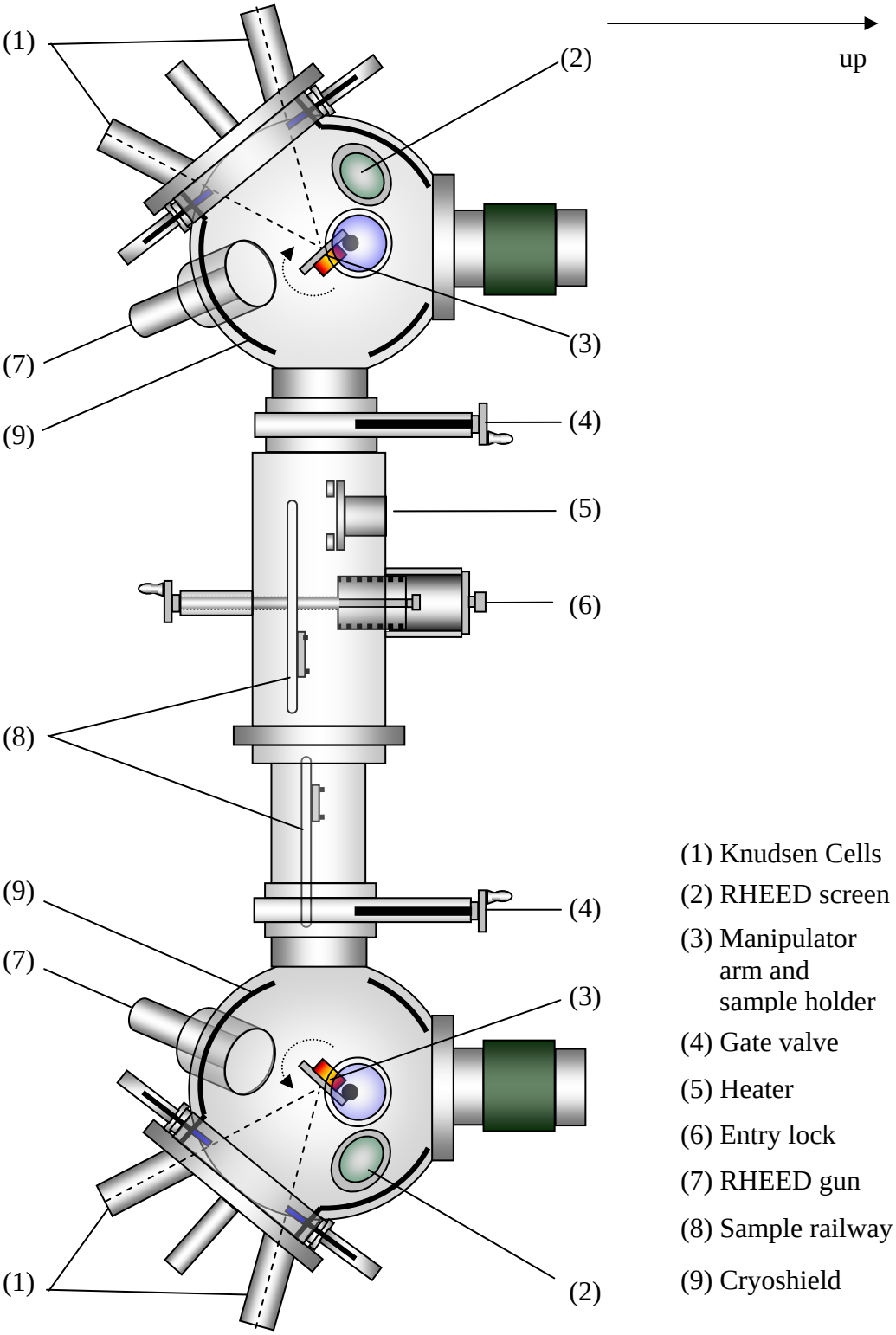

Figure 1. 2 *Side elevation of the same setup with emphasis on the internal components in the chambers.*

Chamber A is predominantly used for the growth of transition metal sulphides such as CrS and MnCrS. Chamber C is used for structures without any residual transition metal doping such as the previously mentioned spin current detector and lift off structures. The samples presented in this thesis were grown in both HWA and HWC and in the forthcoming chapters will be denoted with the prefixes HWA and HWC.

1.5 Outline of thesis.

This thesis presents a study of the growth and characterisation of II-VI metastable sulphides.

Chapter two introduces the characterisation techniques used throughout this thesis. An introduction to the scattering theory of solids is presented and its application in X-ray diffraction from thin films and RHEED is discussed. The operation of both X-ray and RHEED experiments are discussed together with the interpretation of the data obtained. Atomic force and Transmission Electron Microscopy are discussed along with the experimental setup used for Photoluminescence measurements.

Chapter three is a discussion of the growth and characterisation of (Zn,Cr)S layers deposited on GaP substrates. This chapter demonstrates some of the main issues that arise when attempting to grow on GaP substrates in a II-VI growth chamber. A discussion is presented as to the cause of some of these problems and the attempts made to overcome them.

Chapter four focuses on the MgS (100) surface utilizing both AFM and RHEED to obtain quantative values for surface features which develop under certain growth conditions. AFM was used to measure the dimensions and distribution density of 1D features on the MgS surface. By investigating the RHEED patterns information was gathered about the behaviour of elemental species arriving at the surface. Theoretical models were compared to experimental data and results discussed.

Chapter five investigates the structural properties and uses of MgS-rich ZnMgSSe barriers. The growth and characterisation of QW and QD with ZnMgSSe barriers are presented. Determination of the alloy composition is found using X-ray Interference

measurements. The incorporation of this material into epitaxial lift-off structures is demonstrated through a variety of photoluminescence measurements.

The final chapter is a summary of the work covered in this thesis, including directions for future work.

1.6 References.

[1] A.Y. Cho, M.B. Panish, I. Hayashi, 3rd. Int Symp. On Gallium Arsenide and Related Compounds, The Institute of Physics, Conference Series 9 (1970) 18

[2] S. Itoh, K. Nakano, A. Ishibashi, J. Cryst. Growth 214/215 (2000) 1029-1034

[3] T. Yao, Y. Miyoshi, Y. Makita and S. Maekawa, Jap. J. Appl. Phys. 16 (1977) 369-373

[4] D. B. Eason, Z. Yu, W. C. Hughes, W. H. Roland, C. Boney, J. W. Cook, Jr., J. F. Schetzina, G. Cantwell, W. C. Harsch, J. Vac. Sci. Technol, B, 13, 2 (1995) 711-715

[5] S. Taniguchi, T. Hino, S. Itoh, K. Nakano, N. Nakayama, A. Ishibashi, M. Ikeda, Electronic Letters, 32, 6, (1996) 552-553

[6] G. Horsburgh, K. A. Prior, W. Meridith, I. Galbraith, B. C. Cavenett, G. Lacey, A. G. Cullis, C. R. Whitehouse, P. Parbrook, P. Möck and K. Mizuno, Appl. Phys. Lett. 72 (1998), 3148

[7] Y. Fan, J. Han, L.He, J. Sarie, R. L. Gunshor, M. M. Hagerott, H. Jean, A. V. Nurmikko, J. C. Hua and N. Otsuka, Appl. Phys. Lett. 61 (1992), 3160.

[8] C. Bradford, C.B. O'Donnell, B. Urbaszek, A. Balocchi, C. Morhain, K.A. Prior, B.C. Cavenett, J Cryst Growth 227–228 (2001) 634–638

[9] C. Bradforda, B. Urbaszeka, M. Funato, A. Balocchia, T.C.M. Grahama, E.J. McGhee, R.J. Warburton, K.A. Prior, B. Cavenet. J of Cryst Growth 251 (2003) 581–585.

[10] Handbook on Semiconductors, Vol.3b, T. Dietl, (Diluted Magnetic Semiconductors), Chapter17, ed. T. Moss and S. Mahajan, North-Holland, 1992.

[11] S.Y. Wang, I. Hauksson, J. Simpson, H. Stewart, S.I.A. Adams, J.M. Wallace, Y. Kawakami, K.A. Prior, B.C. Cavenett, Appl. Phys. Lett. 61 (1992) 506

[12] S.A. Telfer, C. Morhain, B. Urbaszek, C. O'Donnell, P. Tomasini, A. Balocchi, K.A. Prior, B.C. Cavenett, J Cryst Growth, 214, 215, (2000) 197-201

[13] C. Bradford, C. B. O'Donnell, B. Urbaszek, A. Balocchi, C. Morhain, K. A. Prior, and B.C. Cavenett, Appl. Phys. Lett. 76, (2000) 3929.

[14] L. David, K.A. Prior, Phys Stat Sol. B, 243, 4, (2006) 778–781

[15] A. Curran, J.K. Morrod, K.A. Prior, A.K. Kar, R.J. Warburton, Semiconductor Sci. and Technol. 22 (2007) 1189

Chapter 2

Characterisation techniques used in the growth of II-VI semiconductors.

2.1 Introduction.

There are many characterisation techniques employed to probe the nature of semiconductor materials. These include non-destructive techniques such as X-ray Diffraction and Interference (XRD, XRI respectively)[1,2] Photoluminescence spectroscopy (PL)[3,4,5], Atomic Force Microscopy (AFM)[6,7], and Reflection High Energy Electron Diffraction (RHEED)[8,9,10] and, destructive techniques such as Secondary Ion Mass Spectroscopy (SIMS)[11], Transmission Electron Microscopy (TEM)[12] and Electrochemical Current Voltage (CV) measurements[13]. In this thesis the preferred methods of characterising II-VI semiconductors are the non-destructive techniques, XRI, RHEED, AFM and PL. However, when necessary, TEM was undertaken, but carried out at the University of Cadiz so will not be discussed in great detail.

2.2 Scattering of waves by periodic atomic arrangements; an introduction to X-ray and RHEED.

As two of the most important characterisation techniques (RHEED and XRI) rely on an understanding of scattering of waves in solids this section deals with an overview of the theories underlying them. There are three main scattering processes that are used in the characterisation of solids, they are: X-ray, Electron, and Neutron scattering. For this

section only X-ray and electron scattering will be discussed as these relate directly to XRI and RHEED techniques.

One of the important factors when considering scattering effects is the path difference generated when an incident wavefront encounters scattering centres. If first we define an incident wave with amplitude A(r)

$$A(r) = A_0 \exp(i\mathbf{K}\cdot\mathbf{r}) \qquad \text{Equation 2.1}$$

Where **K** is the wave vector and **r** is the vector defining the change in position of the point of interest P from the origin O. shown in figure 2.1.

The wavevector K lies normal to the wave fronts (loci of equal phase) and has a magnitude of ;

$$|\mathbf{K}| = \frac{2\pi}{\lambda} \qquad \text{Equation 2.2}$$

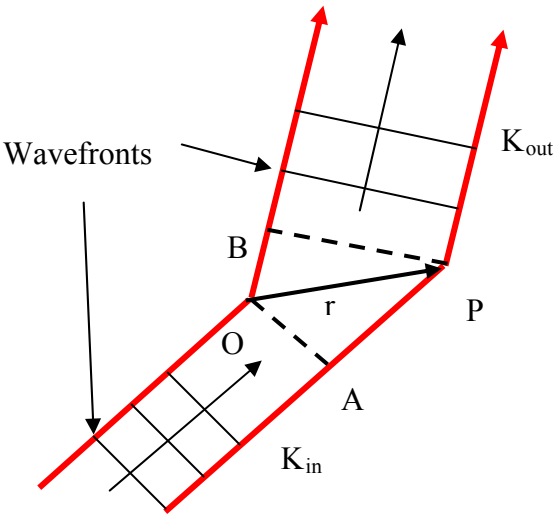

Figure 2. 1 *Wavefront diagram showing incident wavevector* ***K_{in}*** *and scattered wavevector* ***K_{out}*** ***with scattering occurring at points O and P.***

Now, if we define the scattering from an incident wave with wavevector $\mathbf{K}_{in}$ and the scattered wave by $\mathbf{K}_{out}$ then this can be used to determine the phase difference between the incident and scattered waves. It can be seen that the incident wave has wavefronts in phase with the points A and O, and similarly for the scattered wave at B and P. The phase differences AP and OB are:

$$\begin{aligned} AP &= \mathbf{r} \cdot \mathbf{K}_{in} \\ OB &= \mathbf{r} \cdot \mathbf{K}_{out} \end{aligned}$$ Equation 2.3

So the net phase difference, i.e. OP can be found by:

$$\varphi = OP = OB - AP = \mathbf{r} \cdot \mathbf{K}_{out} - \mathbf{r} \cdot \mathbf{K}_{in} = \mathbf{r} \cdot (\mathbf{K}_{out} - \mathbf{K}_{in}) = \mathbf{r}.\mathbf{K}$$ Equation 2.4

The angle between $\mathbf{K_{in}}$ and $\mathbf{K_{out}}$ is defined as 2θ while **K** is commonly known as the scattering vector (figure 2.2). This description relies on a kinematic treatment of the scattering in the solid. It is considered that all scattering is elastic, i.e. there is no exchange of energy between the wave and the solid. In addition, there is no absorption of the wave. This allows for the first relationship needed for an understanding of the scattering geometry.

$$\mathbf{K}_{out} = \mathbf{K}_{in} + \mathbf{K}$$ Equation 2.5

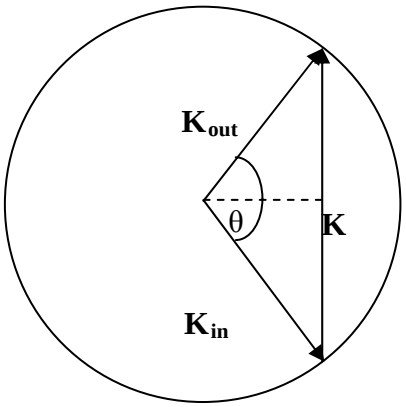

Figure 2. 2 *Ewald spere, defined by the radius* $|\boldsymbol{K_{in}}|=|\boldsymbol{K_{out}}|$.

Also, each scattering centre in the solid is treated as an independent scattering source [14]. From this a sphere encompassing all incident and diffracted wavevectors can be constructed. This is known as the Ewald sphere (figure 2.2). The magnitude of the sphere is defined in equation 2.6.

$$|\mathbf{K}_{in}| = |\mathbf{K}_{out}| = \frac{2\pi}{\lambda}$$ Equation 2.6

It can be seen from simple geometry that the magnitude of the scattering vector is related to θ by:

$$|\mathbf{K}| = \frac{4\pi}{\lambda} sin\theta \qquad \text{Equation 2.7}$$

Equation 2.6 leads to the magnitude of the Ewald sphere encompassing all possible wavevectors. As there is a *1/λ* relationship for all **K** vectors, this sphere resides in reciprocal space.

2.2.1 Scattering from 3D structures.

For this section the X-ray scattering will be discussed, however much the same analysis applies to neutron and electron scattering.

The scattering amplitude for a scattered waves is proportional to the electron density at the scattering point. Referring to figure 2.1, at point *P* there is an electron density denoted by $\rho(\mathbf{r})$. In volume dV around *P* there are $\rho(\mathbf{r})dV$ electrons scattering the wave. If the scattering is proportional to the number of electrons then for an incident wave of amplitude A_0 there will be a scattered wave with amplitude dA where:

$$|dA| = A_0 \rho(\mathbf{r}) dV \qquad \text{Equation 2.8}$$

For X-ray scattering both the amplitude and the phase of the scattered wave has been determined. By combining both the phase and amplitude (equations 2.4 and 2.8) and integrating over all the volumes the amplitude of the scattered wave can be found.

$$A(\mathbf{K}) = \int_{volume} dA = A_0 \int_{volume} \rho(\mathbf{r}) \exp(i\mathbf{K} \cdot \mathbf{r}) dV \qquad \text{Equation 2.9}$$

To determine the scattering from a single atom the volume of interest is the volume containing the atom, and the scattering factor of the atom for a given **K** is given by the function $f(\mathbf{K})$ where:

$$f(\mathbf{K}) = \int_{atom} \rho(\mathbf{r}) \exp(i\mathbf{K} \cdot \mathbf{r}) dV \qquad \text{Equation 2.10}$$

For a volume much greater than the size of one atom, the simplest method is to assign all volumes dV to an atom, and the integration can be sum over all atoms within the volume. $N_{tot.}$ This leads to the equation 2.11.

$$A(\mathbf{K}) = A_0 \sum_{i=1}^{Ntot} \exp(i\mathbf{K} \cdot \mathrm{r_i}) f_i(\mathbf{K}) \qquad \text{Equation 2.11}$$

Here $f_i(\mathbf{K})$ is the scattering factor and $\mathbf{r}_i$ is the vector describing the position of the i^{th} atoms nucleus with respect to the origin.

This is a general equation which can be made more usable if the symmetry in crystals is used to determine atomic positions of atoms in relation to one another.

2.2.2 Conditions for diffraction in symmetric solids.

If we consider a crystal consisting of a parallelepiped of sides $N_{\mathbf{a}}xN_{\mathbf{b}}xN_{\mathbf{c}}$ unit cells with **a**, **b** and **c** representing the unit cell vectors starting at the origin (0,0,0). The unit cells can be numbered in each direction, thus, any particular atom can be associated with unit cells (n_1, n_2, n_3). The $\mathbf{r_i}$ value previously used for the position of the nucleus with respect to the origin has to be replaced to take the unit cell position into consideration. Thus:

$$\mathbf{r_i} = n_1\mathbf{a} + n_2\mathbf{b} + n_3\mathbf{c} + \mathbf{r_i''} \qquad \text{Equation 2.12}$$

Where, $\mathbf{r_i''}$ is the vector to the i^{th} atom from the origin of the unit cell containing it. This can then be substituted into equation 2.11 generating a modified amplitude function. In this case we now sum over the all the atoms in the unit cell, then the all the cells in three dimensions which generates a 4 termed expression for the amplitude of the scattered wave.

$$A(\mathbf{K}) = A_0 \sum_{n_1=0}^{N_i} \exp(i\mathbf{K} \cdot n_1\mathbf{a}) \sum_{n_2=0}^{N_2} \exp(i\mathbf{K} \cdot n_2\mathbf{b}) \sum_{n_3=0}^{N_3} \exp(i\mathbf{K} \cdot n_3\mathbf{c}) \sum_{i=1}^{n} \exp(iK \cdot \mathbf{r}_i'') f_i(\mathbf{K})$$

Equation 2.13

This equation breaks down into two distinct parts: the first three terms are related to the lattice geometry and are quantitive, the last however does not depend on lattice geometry but rather the atoms positions within the unit cell. By considering just the first terms it can be seen that these are geometric progressions and can be rearranged into the form:

$$\sum_{n_1=0}^{N_i} \exp(i\mathbf{K}\cdot n_1\mathbf{a}) = \frac{1-\exp(i\mathbf{K}\cdot N_1\mathbf{a})}{1-\exp(i\mathbf{K}\cdot\mathbf{a})} \qquad \text{Equation 2.14}$$

Considering just the first terms in equation 2.13 then the intensity of the scattered wave can be found from the magnitude squared, such that:

$$I(\mathbf{K}) = \left|A(\mathbf{K})\right|^2 \propto \left|\frac{1-\exp(i\mathbf{K}\cdot N_1\mathbf{a})}{1-\exp(i\mathbf{K}\cdot\mathbf{a})}\right|^2 \qquad \text{Equation 2.15}$$

Furthermore;

$$\left|\frac{1-\exp(i\mathbf{K}\cdot N_1\mathbf{a})}{1-\exp(i\mathbf{K}\cdot\mathbf{a})}\right|^2 = \frac{\sin^2\left(\frac{\mathbf{K}\cdot N_i\mathbf{a}}{2}\right)}{\sin^2\left(\frac{\mathbf{K}\cdot\mathbf{a}}{2}\right)} \qquad \text{Equation 2.16}$$

If this is repeated for the other lattice vectors then it becomes apparent that the intensity of the scattered wave is modulated by a $\sin^2$ function in **a**, **b** and **c** directions [15]. This equation is crucial to highlight as the majority of studies undertaken in this thesis rely on this modulation in order to model structures that are being investigated. It is also important as it can highlight some of the conditions that constrain the allowed scattering vectors. Because of the sinusoidal nature of the equation there are only certain **K** values that will generate a finite scattering intensity. In the limit where N_i is large there will only be a finite intensity when the denominator is zero, i.e. when,

$$\frac{\mathbf{K}\cdot\mathbf{a}}{2} = h\pi \qquad \text{Equation 2.17}$$

With h as an integer.

Then $I(\mathbf{K}) = 0$ for all **K** values, other than when $\mathbf{K}\cdot\mathbf{a} = 2\pi h$. This is the first of three similar equations derived from the three lattice dependent terms of equation 2.13 known as the first Laue equations and which are usually represented in the form

$$\begin{aligned} \mathbf{K}\cdot\mathbf{a} &= 2\pi h \\ \mathbf{K}\cdot\mathbf{b} &= 2\pi k \\ \mathbf{K}\cdot\mathbf{c} &= 2\pi l \end{aligned} \qquad \text{Equation 2.18}$$

From the unit vectors in real space **a**, **b**, and **c,** we define reciprocal unit vectors $\mathbf{a}^*$, $\mathbf{b}^*$ and $\mathbf{c}^*$ as:

$$\mathbf{a}^* = \frac{\mathbf{b}\times\mathbf{c}}{\mathbf{a}.(\mathbf{b}\times\mathbf{c})},\ \mathbf{b}^* = \frac{\mathbf{c}\times\mathbf{a}}{\mathbf{b}.(\mathbf{c}\times\mathbf{a})},\ \mathbf{c}^* = \frac{\mathbf{a}\times\mathbf{b}}{\mathbf{c}.(\mathbf{a}\times\mathbf{b})} \qquad \text{Equation 2.19}$$

For a set of planes (*hkl*) the reciprocal lattice vector defining these planes is given by

$$\mathbf{d}^*_{\mathrm{hkl}} = h\mathbf{a}^* + k\mathbf{b}^* + l\mathbf{c}^* \qquad \text{Equation 2.20}$$

Substituting this into the first Laue equation as a value for **K** we can show that $\mathbf{d}^*_{hkl}\cdot\mathbf{a} = 2\pi h$ therefore $\mathbf{d}^*_{hkl} = \mathbf{K}$ is a solution to the Laue equations.

From equation 2.7 we know that:

$$|\mathbf{K}| = \frac{4\pi}{\lambda}sin\theta$$

Substituting $\mathbf{d}^*_{hkl} = \mathbf{K}$ into equation 2.7 where $\left|\mathbf{d}^*_{hkl}\right| = 2\pi/\mathrm{d}_{hkl}$ gives:

$$\lambda = 2d_{hkl}\sin\theta \qquad \text{Equation 2.21}$$

This equation is commonly known as the Bragg equation [16] and is the keystone to the setup of all X-ray measurements. By deriving this condition the allowed angles and crystal planes can be defined, limiting the range angles where by diffraction will occur. There are however other structural factors and systematic absences derived from the crystal structure that need to be incorporated in to the scattering theory of solids in order to achieve a more complete treatment.

2.2.3 Structure factor and systematic absences.

For the materials presented in this thesis it is important to consider the structure factor. This structure can be derived from the Laue conditions and equation 2.15 giving a value for the intensity as:

$$I(hkl) = A_0^2V^2\left|\sum_{i=1}^{n}\exp(i\mathbf{K}\cdot\mathbf{r}_i'')f_i(\mathbf{K})\right|^2 \qquad \text{Equation 2.22}$$

Where V is the volume of the crystal.

$$\mathbf{K} \cdot \mathbf{r_i''} = 2\pi(hx_i + ky_i + lz_i) \qquad \text{Equation 2.23}$$

We can express equation 2.22 as:

$$I(hkl) = A_0^2 V^2 \left|F(hkl)\right|^2 \qquad \text{Equation 2.24}$$

Where *F(hkl)* is the structure factor and can be written explicitly as:

$$F(hkl) = \sum_{i=1}^{n} \exp(2\pi i(hx_i + ky_i + lz_i)_i) f_i(\mathbf{K}) \qquad \text{Equation 2.25}$$

Using equation 2.24 it can be shown that for any non-primative lattice there will be systematic absences, i.e. sets of *(hkl)* for which *F(hkl)* = 0. For the cubic-F lattice, this means that non-zero intensities are only obtained when *hkl* are all even or all odd. For all the samples presented in this thesis the (400) plane is chosen as it provides the most intense diffracted peaks. Other planes such as the (115) plane are discussed briefly in chapter 3.

2.2.4 Thin layer diffraction.

One of the important relationships that come out of this treatment is the $\sin^2$ intensity modulation demonstrated in equation 2.16. When applied to thin layers when N_i is small the scattering will be intense over a range of values $\mathbf{K} \cdot \mathbf{a}$ near where the Bragg condition is fulfilled. Therefore we can expect broad peaks from thin layers and narrow peaks from thick layers, with measurable narrowing of the peaks even when $N \approx 100$.

Around the Bragg peak there will be a series of subsidiary peaks with a spacing inversely proportional to the thickness of the layer. These subsidiary peaks are known as Pendellösung fringes and occur repeatedly during the analysis done during this thesis, allowing measurement of the material thickness for very thin layers. This is especially important when developing new materials of unknown properties and has been demonstrated by our group in the generation of MgS containing structures [17]. XRI is used extensively in chapter 3 for the development of CrS to gain a measure of thickness and ZnMgSSe in chapter 5 to quantify the composition and thickness of these new materials.

Modulation of the Pendellösung fringes arises in XRI samples when a phase change is introduced as X-rays are passed through two similar layers separated by a second material. If the two materials differ in strain there can be enough interference introduced to produce observable changes in the Pendellösung fringes. There are however limits to this method due to the relationship between the strain mismatch between materials and the phase change introduced by the spacer layer. The phase change $\delta\varphi$ introduced by the plane of the central layer is given by:

$$\delta\varphi = 2\pi\, m^* \qquad \text{Equation 2.26}$$

Where m* is the fractional lattice parameter mismatch between the spacer and cladding layers, given by:

$$m^* = \frac{a_{cladding} - a_{spacer}}{a_{spacer}} \qquad \text{Equation 2.27}$$

For N planes of the central material equation 2.26 becomes:

$$\delta\varphi = 2\pi\, N\, m^* \qquad \text{Equation 2.28}$$

The spacer layer thickness is represented by the thickness of one plane, given by d_{hkl}, multiplied by the number of planes N:

$$t = d_{hkl} N = \frac{a}{4} N \qquad \text{Equation 2.29}$$

Assuming a 400 reflection, and combining Equations 2.28 and 2.29 gives:

$$\delta\varphi = 8\pi \frac{t}{a} m^* \qquad \text{Equation 2.30}$$

Holloway [18] suggests that the minimum layer thickness that can be resolved corresponds to a phase change of $\pi/16$. Therefore the constraint for the structure mismatch becomes:

$$m^* \geq \frac{1}{128} \frac{a}{t} \qquad \text{Equation 2.31}$$

Giving a minimum resolvable thickness of:

$$t \geq \frac{1}{128}\frac{a}{m^*}$$ Equation 2.32

This tells us for a given set of lattice parameters there is a finite thickness where fringes will be observed.

2.2.5 Dynamical theory of X-rays.

In the research contained in this thesis all characterisation using X-rays was done using simulation software to accurately model the structure under investigation. The programs that have been developed to do this modelling are based on a more precise method for treatment of the X-rays, known as the Dynamical theory which will be discussed briefly in this section.

One of the considerations that is omitted from the kinematic theory is the absorption of waves through the material. In the dynamic theory the incident and diffracted beams are considered as one entity that continually transfers energy from one wave to the other [19,20]. It is considered that the incident and diffracted beams set up a standing wave in the crystal, resulting from equal but opposite wavefunctions. If the nodes of this wave lie in the same position in the crystal very little absorption can occur. This is contrary to initial expectations as it is expected that a wave travelling through a medium will impart some energy to surrounding material. However it is observed experimentally that transmission through the crystal is possible in certain directions when it is expected to be absorbed. The kinematic theory cannot explain this phenomenon, whereas the dynamic theory can.

This theory relies on the inclusion of a Fourier component of charge density in the material that is related to the reciprocal lattice spacing. By doing this the crystal is no longer treated as a 3D volume of scattering centres but rather a system with a periodic dielectric constant. Dynamic theory allows for software analysis of rocking curve spectra produced when a crystal is irradiated by X-rays and scanned over an angular range centred at the Bragg angle. The dynamic theory has been developed further by Takagi and Taupin [21,22] but this treatment is beyond the scope of this discussion.

2.2.6 X-ray Experimental system.

A schematic diagram of the Heriot Watt X-ray diffraction system is shown in figure 2.3. Currently the system in place is a BEDE 200 system running in conjunction with BEDE RADS simulation software.

The X-rays are generated from electron bombardment of a copper target and therefore produce radiation most intense at the Cu Kα line (1.54 Å). Emitted radiation is non-coherent and radiates in all directions, and to confine the radiation, it is only allowed to emit from a small diameter beryllium window. Collimation of the radiation is achieved *via* a single crystal of silicon, aligned so that a small etched channel is in line with the incident radiation. Only radiation with the correct angle for diffraction will be collimated and transmitted, all other angles are absorbed by the Si [23]. As the only requirement for transmission is that the Bragg condition is fulfilled, there are a range of wavelengths that can be transmitted. A broad spectral beam is produced which needs to pass through a monochromator in order to select a specific wavelength to be irradiated onto the sample. By using the (333) reflection of a (111) orientated crystal, a specific wavelength can be selected. In much the same way the collimator crystals will only allow transmission of radiation that satisfies the Bragg angle, the monochromator is setup so that only one wavelength will fulfill the Bragg angle and as such will only transmit that specific wavelength.

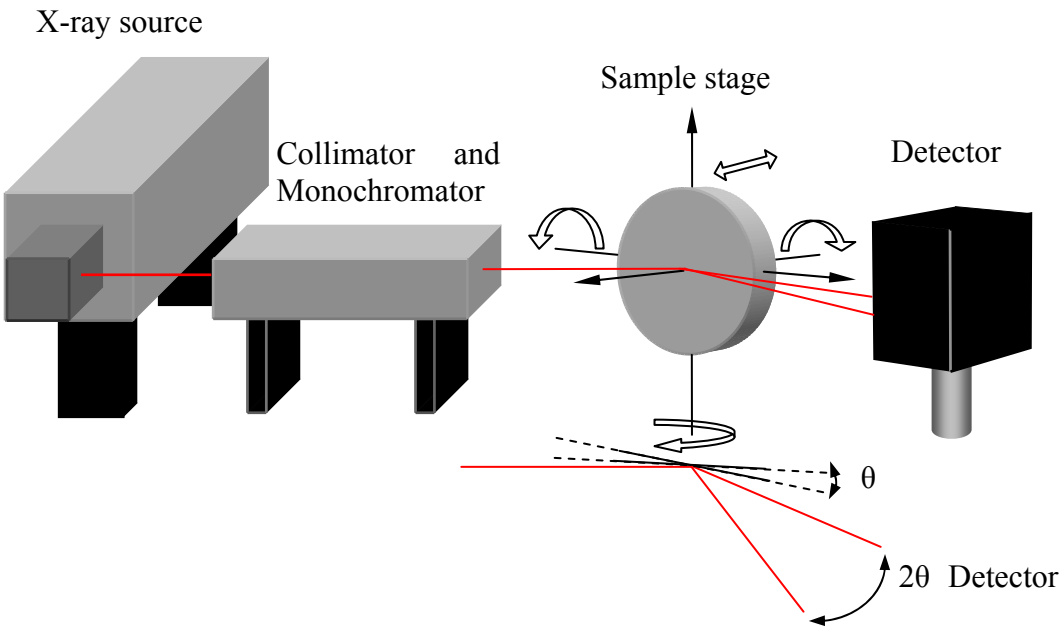

Figure 2. 3 *Experimental setup of the BEDE 200 system currently at Heriot-Watt.*

After a collimated beam has been produced it irradiates onto the sample attached to the 4 axis stage. The stage is set up so that chosen reflecting plane is at the Bragg angle to the incident beam. As mentioned previously, there are specific lattice planes that will provide strong diffraction. For the most part the 400 plane is used as it satisfies the conditions for strong diffraction. Both GaP (chapter 3) and GaAs (chapter 4 and 5) substrates are utilized in this thesis so the stage can be adjusted to accommodate the change in Bragg angle for the substrate under investigation.

The detector is a solid state device with its output transferred to a PC where the counts are recorded. Shown in figure 2.3, the detector is setup so that it makes an angle of 2θ with the sample stage. Rocking curve analysis presented in this thesis requires this relationship to remain constant throughout the entire scan range. Consequently as the stage is rotated through a range of many arcseconds the detector is moved in unison to maintain the same $\theta/2\theta$ alignment. As the detector scans through this range the intensity is obtained as a function of angle θ. Once obtained the $I(\theta/2\theta)$ spectrum can be imported into the BEDE simulation software which allows for the determination of layer thickness, composition, lattice parameter, strain, and interlayer grading.

One of the key abilities of the BEDE software is the ability to simulate specified models and compare them to data collected from experimental scans. As a measure of the merit of the simulated model the software does statistical analysis comparing the intensities of the reference and the comparison spectra over a specified angular range to produce a goodness of fit GOF value ranging from 0 to 1. This is a chi-squared statistical analysis and is calculated as follows;

$$\chi^2 = \sum_{i=j}^{k} \left[\log(y_i^{ref}) - \log(y_i^{comp}) \right]^2 \qquad \text{Equation 2.32}$$

Where, y_i^{ref} is the ordinate of the reference data and y_i^{comp} is the ordinate of the comparison, and j and k are the indices of the first and last points defining the overlapping of the two data sets. If the two data sets become more alike the GOF value reduces. GOF measurements were used extensively in chapter 5 to model the composition of ZnMgSSe.

2.2.7 Scattering from 2D layers, an introduction to RHEED.

In a similar fashion to the treatment described for X-ray scattering the scattering from the electron beam is dependent on the periodicity of the scattering centers in the material. Because of this the conditions set for X-ray diffraction discussed in section 2.2.1 can be used for electron scattering.

The two main types of electron scattering used in crystallography are LEED (Low energy electron diffraction) and RHEED. LEED is not used as the geometry required is not suitable for use in an MBE chamber, whereas the RHEED measurement technique is ideally suited to MBE growth. By using much higher energies a glancing angle beam can be used incident on the surface. The trajectory ensures that it is perpendicular to the molecular beams and avoids any obstructions in the chamber. The glancing angle to the substrate surface (~1°, figure 2.4), causes the component of the electron momentum normal to the surface to be small, resulting in complete reflection from the top 1-2 atomic layers. These two factors enable the evolution of the substrate surface to be monitored during growth making it an invaluable analytical tool unique to MBE.

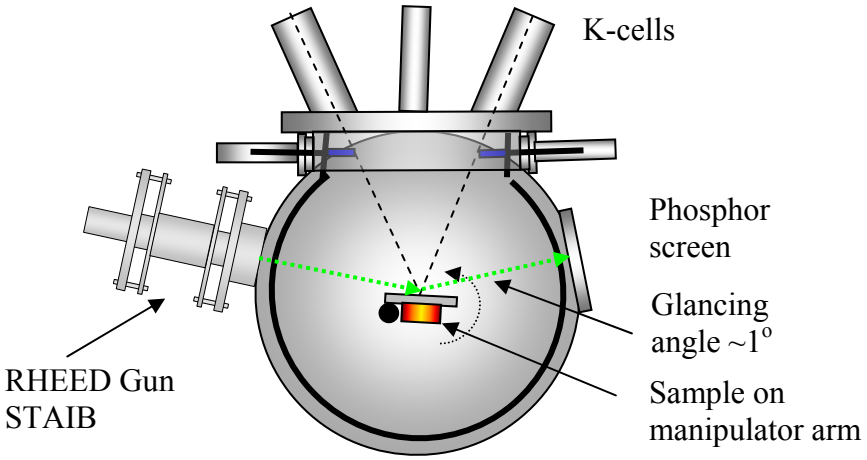

Figure 2. 4 *Schematic of the geometry of the RHEED setup within an MBE chamber.*

In a similar manner to X-ray diffraction an Ewald sphere can be constructed in order to represent the conditions for diffraction. A representation of this can be seen in figure 2.5. As shown the period repeat distance normal to the surface is zero so the reciprocal representation of this is an infinite long thin rod in comparison to the lattice points

described in X-ray diffraction. As with the lattice points described previously these rods, when intersecting the Ewald sphere, describe the conditions for diffraction.

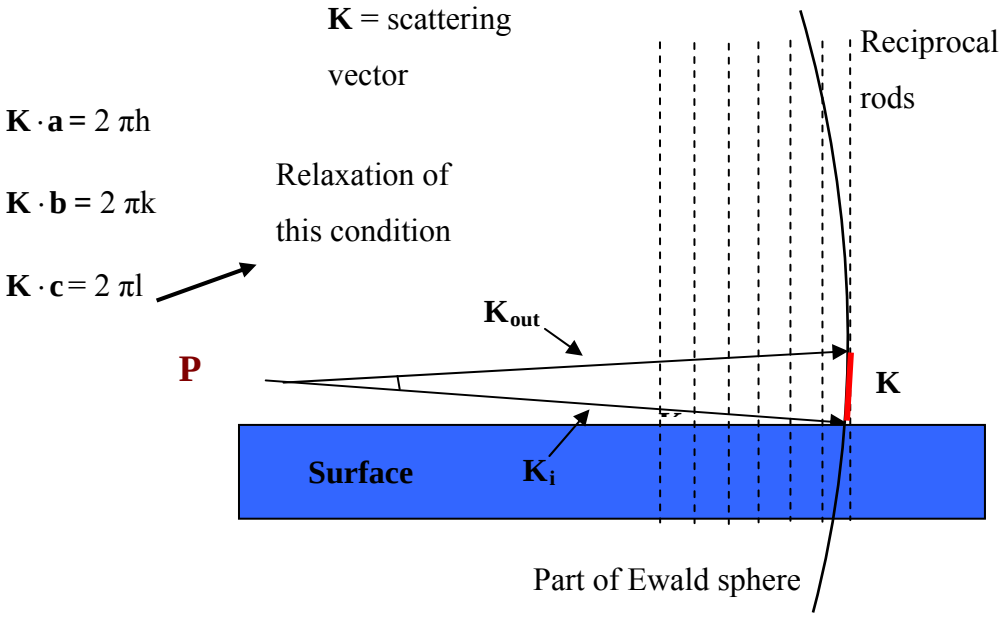

Figure 2. 5 *2D representation of the Ewald sphere intersecting reciprocal lattice rods. P is the centre of the sphere.*

2.2.8 Physical origins of RHEED patterns.

In the model for RHEED a perfectly flat surface is the intersection of 2 Laue 2D rods with the Ewald sphere and is an arc of spots whose positions are determined by the Laue conditions and are said to exist in a Laue zone. It has been widely observed however that during regular growth a streaky pattern is seen. This can be explained by the disorder on the surface which broadens the reciprocal lattice rods. Other factors such as the beam profile and phonon scattering can have an effect on the pattern though their combined effects are negligible in comparison to the effects of surface morphology [24,25,26].

It is assumed that no surface is perfectly ordered but can be considered to consist of domains that cover the surface. These domains can exist as either perfectly formed ordered regions, or disordered and with high non-uniformity. Due to the coherence length of the beam RHEED can only sample a finite length on the sample, typically in the region of a few thousand Å. As a result there is a high probability that the domain

size on the surface is larger than the beam sample size. This maximum resolvable distance (MRD) is dependent on the beam energy so high energies are chosen to reduce the MRD as much as possible. Domains larger than the MRD will appear as infinatly large ordered surfaces and therefore sharp spots situated on an arc defined by the intersection of reciprocal lattice rod array and the Ewald sphere will be observed. For domains smaller than the MRD streaks will be seen.

One other important type of disorder observed is when the crystal has not grown in a uniform manner but consists of crystal domains which have random orientations and are far smaller than the MRD. Like a crystal powder on the surface, this disordered material scatters the beam in all directions and diffuse rings are seen in the RHEED. Known as an amorphous ring, this is observed both during very poor growth conditions generating almost no crystalinity and also during the presence of an oxide layer. The 4 main types of disorder and resultant RHEED patterns are shown in figure 2.6.

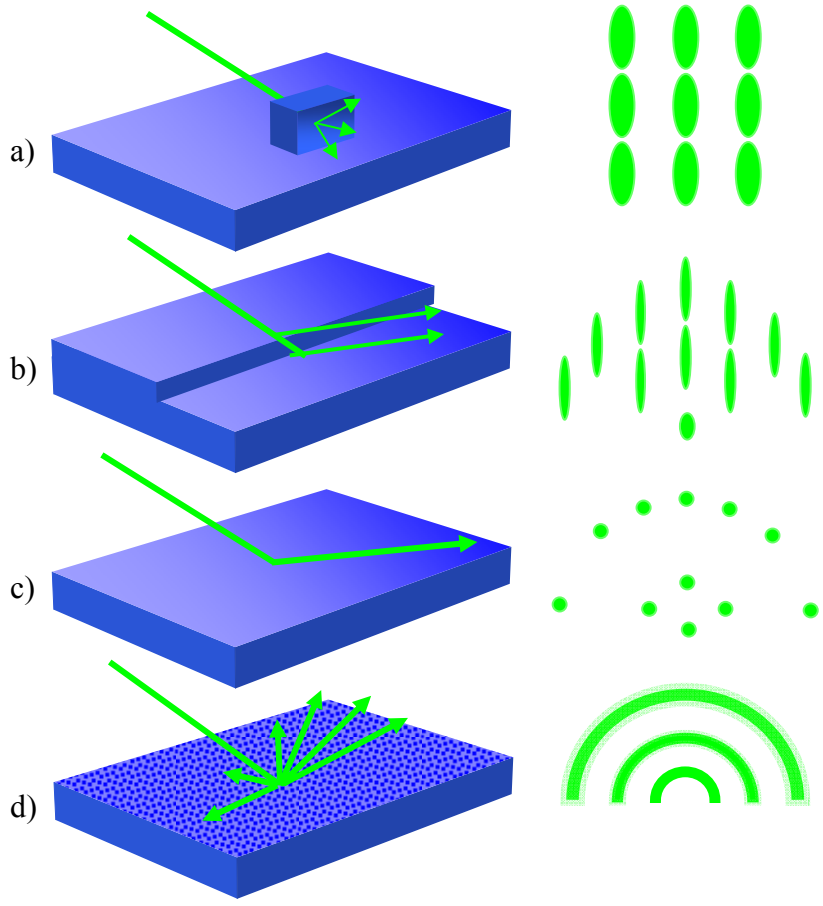

Figure 2. 6 *Schematic of RHEED patterns from various surfaces. a) rough surface with 3D features, b) stepped surface, c) flat surface, d) polycrystalline*

The intensities of the diffraction features generated on the screen have a similar relationship to that of X-ray diffraction and are related to the square of the structure factor. The structure factor for RHEED however is slightly modified to encompass new parameters associated with surface interaction. For example, the normal and parallel to surface components of the wavevector have to be considered.

2.2.9 RHEED pattern nomenclature.

The nomenclature for RHEED patterns is determined from the bulk surface mesh which can undergo reconstruction. This is a deviation in the position of surface atoms from the bulk lattice positions. Reconstruction occurs to minimise the surface energy and maintain average charge neutrality [27]. A surface that has not undergone reconstruction is said to have a (1x1) RHEED pattern, where the two numerical values are descriptions of the periodicity of the species in two orthogonal directions.

When a surface has undergone reconstruction then there is an increase in the periodicity of the surface unit mesh. If **a** and **b** are the translation vectors describing an ideal surface mesh then $\mathbf{a_s}$ and $\mathbf{b_s}$ are the vectors describing the mesh that has undergone reconstruction. They are related by:

$$\mathbf{a_s} = M\mathbf{a}, \mathbf{b_s} = N\mathbf{b} \qquad \text{Equation 3.33}$$

Where M and N are the periodicity of the unit cell along the [110] and $[1\bar{1}0]$ azimuths respectively. For a surface that is exhibiting such a reconstruction the notation (MxN) is used. For surfaces where the shortest unit cell vector is of the form $\mathbf{a_s}$ = M**a,** $\mathbf{b_s} = M\mathbf{a}/2 + N\mathbf{b}/2$ a non primitive centered unit mesh can be used and the notation changes to c(MxN). Similarly for a surface where reconstruction of the mesh is rotated by θ degrees it becomes (MxN)Rθ.

Reconstruction is observed in the RHEED by the presence of faint streaks between the more pronounced substrate derived streaks. On surfaces where no reconstruction is occurring and only the (1x1) pattern is observed the so called integral order streaks are observed while on reconstructing surfaces, the fainter intermediate streaks are known as fractional order streaks. An example of this is the non metal rich (2x1) pattern as observed during growth of ZnSe which is shown in figure 2.7. Although the notation used in the RHEED nomenclature gives the user a clear indication of the periodicity of

the surface along given azimuths, the physical interpretation of this in relation to how the atoms are arranged is still undefined. On GaAs and Si there have been many studies conducted to clarify this problem but in our material system there has been very little work on understanding the RHEED patterns and the arrangement of atomic species on the surface.

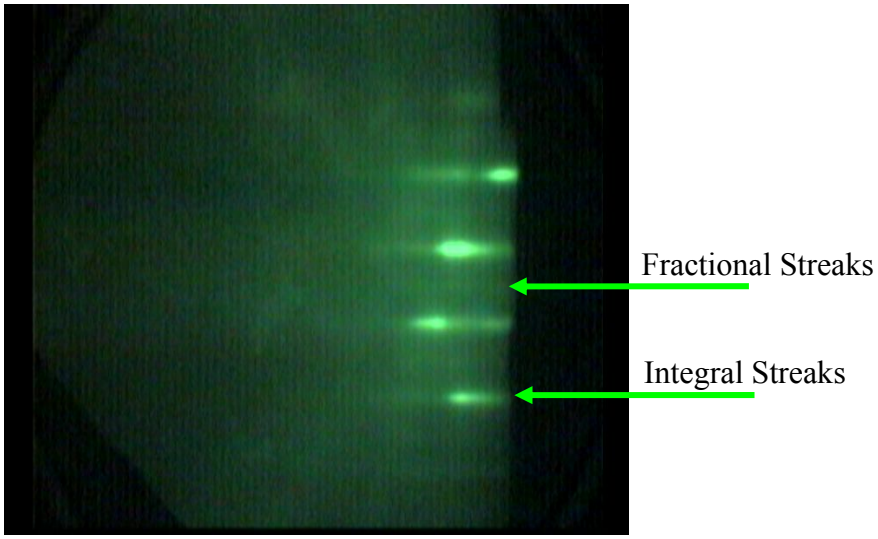

Figure 2. 7 *Video still of (2x1) reconstruction during ZnSe growth. This image shows reconstruction along the [110] direction.*

One further consideration to be noted is the shape of the RHEED spots/streaks. If disorder on the crystal is anisotropic the size and shape of the diffraction spots can change during rotation of the sample. For example if the RHEED beam intersects an azimuth where there is low disorder and domains are large then the diffraction will yield a sharp streaky pattern while in the orthogonal direction domains are small and surface is disordered the diffraction spots will be elliptical in profile. This is discussed in more detail in chapter 4 section 4.3.2.

The use of RHEED in semiconductor growth is predominantly to give the grower access to real time data on the surface morphology during growth rather than post growth techniques such as TEM [6], and AFM [3]. By taking stills or videos of the patterns, an indication of terrace dimensions and distributions can be found by measuring the streak dimensions. This is explained in more detail in chapter 4 with regards to the surface morphology of MgS.

2.3 Atomic Force Microscopy (AFM).

The AFM examines the uppermost topography of the sample. Invented by Binnig *et al* in 1986 [6] this technique is used to study structures smaller then the wavelengths of visible light and was developed as an alternative to scanning tunnelling microscopy (STM). This technique allows for measurement of height fluctuations with nm resolution, while mapping the distribution of surface features [28]. Using this method such features as quantum dots [29], wires [7] and nanostructures can be observed as well as atomic layer smoothness and the transformation from ZB to rocksalt [30]. For the investigations carried out in this thesis only topography of the surface was considered, however a comprehensive description of current and future applications has been published recently [31].

Unlike a conventional microscope AFM dose not directly observe the surface *via* a light source and lenses, but utilises the Van Der Waals force. A very fine sharp silicon etched tip is attached to a piezo mount allowing for a raster scan over the surface. A laser is shone onto the cantilever close to the location of the tip and reflected beam directed onto a split photodetector. As the tip is scanned over the surface, interaction occurs with the top-most atoms attracting or repelling the tip and deflecting laser beam.

There are two normal modes of operation for the AFM, contact and tapping modes; however contact mode can lead to surface damage and consequently is not used in our experiments, and will not be discussed here. Tapping mode helps to overcome the problems associated with contact mode, in particular, friction, adhesion and electrostatic forces between the surface and the tip. It does this by alternately placing the tip in contact with the surface in order to obtain high resolution, then lifting the tip, preventing dragging along the surface.

In tapping mode the cantilever assembly is oscillated at its resonant frequency, by means of a piezoelectric crystal. While scanning, the oscillating tip intermittently contacts the surface at a frequency between 50 and 500 kHz with amplitude ranging typically from 20nm to 200nm. As the tip scans the surface in a raster pattern the oscillation amplitude scales in direct proportion to the average distance of the probe to the sample. Using the split photo detector a feedback loop is generated controlling tip

sample interaction. The signal from the photo detector is then amplified, digitized and converted by the software program. Analysis of the data is undertaken using the software provided with the AFM system. Parameters such as feature dimensions, sectional profiles, distribution densities and surface roughness are obtained by this method. These parameters were used in chapter 4 to characterise undulations in the topography of MgS in order to determine height and distribution of nanowires on the surface. The surface roughness feature was used in chapter 5 to compare the surface of MgS and a newly developed ZnMgSSe. A schematic of the AFM system is shown in figure 2.8.

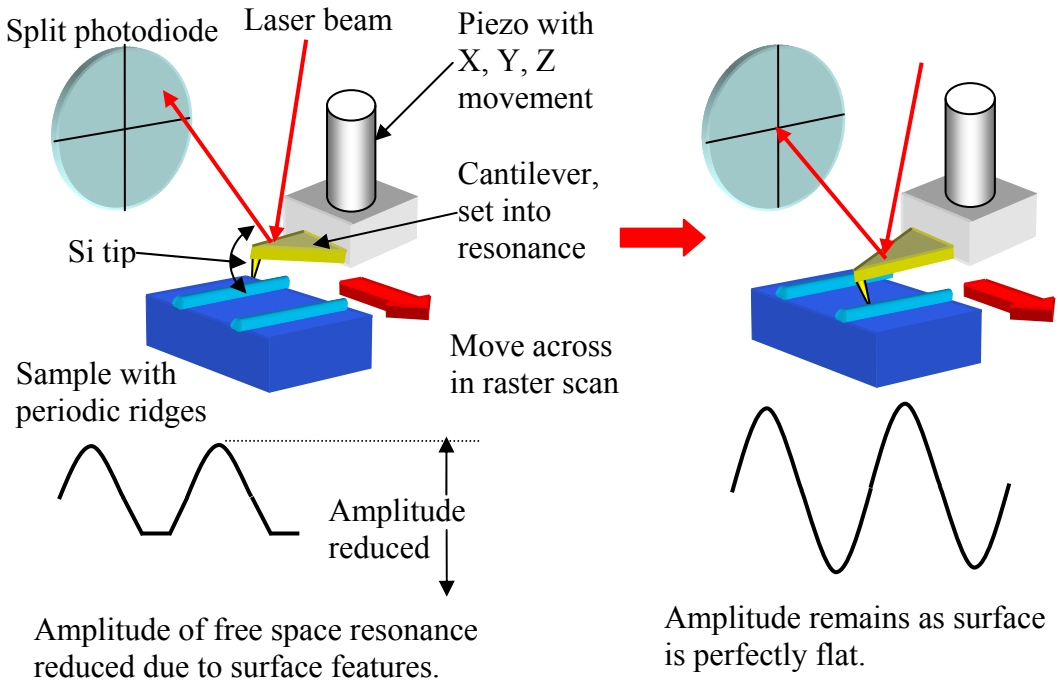

Figure 2. 8 *Schematic of AFM setup showing how deflection of cantilever can translate to feature height.*

One of the considerations to be noted is the profile of the scanning tip. The tip used in this thesis is an etched Si asymmetric tip with a kite profile as shown in figure 2.9. Because of the tip profile any sample that has features with steep sides will return a scan with skewed edges.

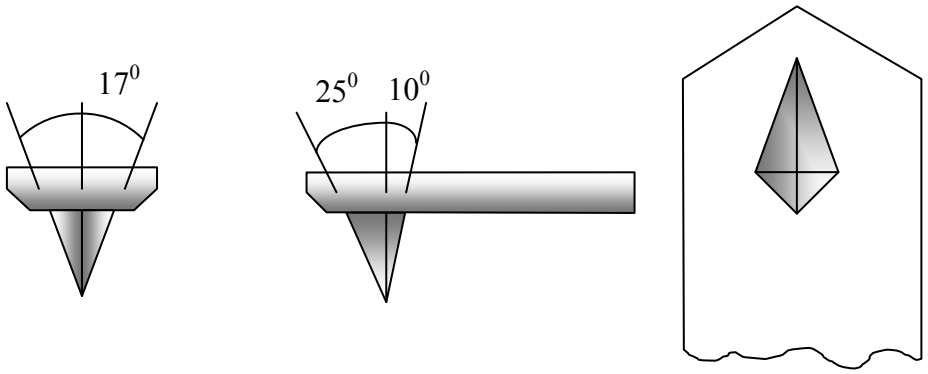

Figure 2. 9 *Tip profile of the Si cantilever tip used in the Dimensions 3100.*

AFM is used extensively in chapter 4 to characterize MgS nano wires and these features are far smaller than the tip dimensions. The effects of the tip profile on the scans were considered to be negligible.

2.4 Photoluminescence Spectroscopy (PL).

All three characterization techniques that have been discussed previously have dealt with the structural properties of the material whereas PL probes the electronic structure of the material. Unlike the previous techniques all PL measurements were undertaken by a member of the Nano-optics group at Heriot-Watt University. This technique is included here to show how the information gathered from PL complements that obtained from other methods.

By irradiating the sample with light of greater energy than the band gap of the material electron hole pairs are generated. Bound by coulomb attraction these excitons have energy equivalent to the band gap of the material minus the exciton binding energy. The binding energy of the exciton for a given state n is found by:

$$E_x^n = -13.6 \frac{\mu}{\varepsilon_r^2} \frac{1}{n^2} \text{ eV} \qquad \text{Equation 3.34}$$

where ε_r is the bulk dielectric constant and μ is the reduced mass.

Values for bulk II-VI materials are ~ 20meV [32] compared to E_{kT} at room temperature of 25meV. To produce stable excitons, the thermal energy in the crystal has to be reduced below the bulk binding energy or, alternativly, the binding energy has to be

increased. By confining the carriers in low dimensional structures the binding energy can be increased to ~ 40meV allowing for stable excitons right up to room temperature.

Carriers that are excited with energies above the band gap undergo thermalisation prior to recombination. In this process the carriers excess energy is removed in a few picoseconds. This is a non-radiative process. Subsequent, recombination of the electron-hole pair can occur as both radiative (photon) and non radiative (phonon) emissions. This process is shown in figure 2.10. Localized defects or dislocations in the material can alter the radiative process resulting in multiple emissions of lower energy photons. The emission energies are however well known and can be identified easily from the spectra and thus provide detailed information on what defects are present [33,34].

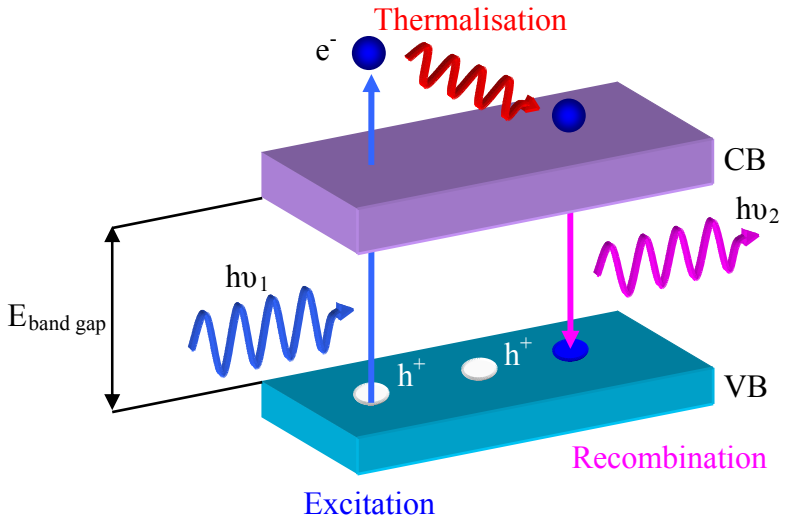

Figure 2. 10 *Schematic of exciton excitation, themalisation and recombination.*

By confining the excitons in low dimensional structure such as quantum wells the efficiency of the emission can be greatly improved by increasing the exciton binding energy. In these structures the excitons are generated in the barrier region and either drift or diffuse into the well region. The high band gap barrier confines the excitons and quantises the density of states within the well. Sinusoidal wavefunctions now exist in the growth direction with small evanescent fields permeating into the barrier region [35] as shown in figure 2.11. This field limits the dimensions of the barrier material especially when multi-quantum wells are considered. If barriers are too thin then the evanecant field will allow transport of carriers into adjacent QW, reducing quantum efficiency and PL emission. Quantum well thicknesses are usually in the order of few

tens of Å's, which is comparable to the de Broglie wavelength. The density of states for QWs is changed from that of the bulk material, due to the quantisation of the momentum in the growth direction. The density of states in the energy interval dE for a quantum well is given by:

$$N_{\lambda D}(E)\,dE = \frac{m^*}{\pi^2 \hbar^2 L_Z}\,dE \qquad \text{Equation 3.35}$$

Where λd is the de Broglie wavelength, m* is the effective mass of the conduction band electron and L_Z is the width of the confining region. The total energy of the electron is calculated by solving the Schrödinger equation [36], and the corresponding total energy for an infinitely deep well is given by:

$$E(l,k_x,k_y) = \frac{\hbar^2}{2m^*}\left[\frac{\pi^2 l^2}{L_Z^2} + k_x^2 + k_y^2\right] \qquad \text{Equation 3.36}$$

Where l=1,2,3,4,… is the band index. This equation shows that as the well width decreases the quantised bound state energies increase. Consequently higher barriers are needed to contain the confined states.

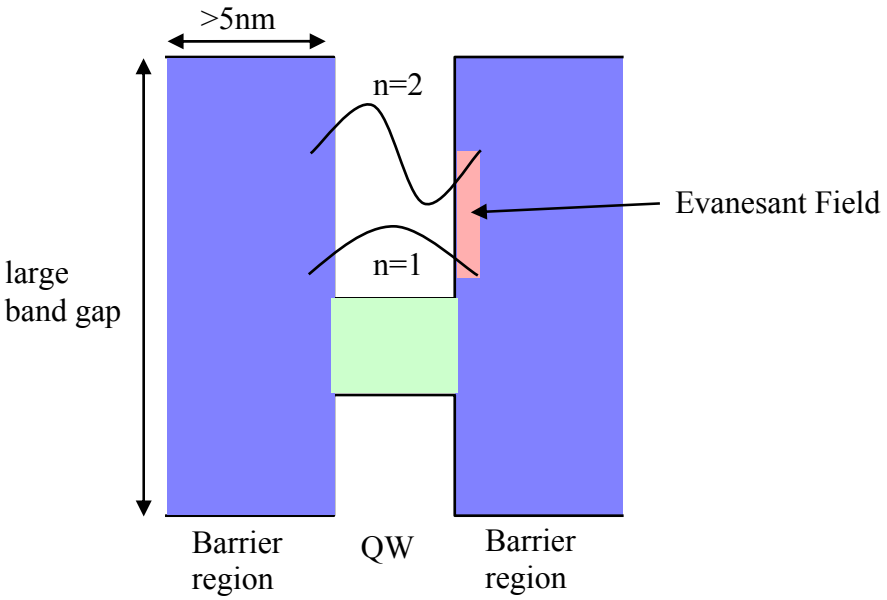

Figure 2. 11 *Band structure of a typical QW showing quantised electron confinement.*

The QW devices presented in this thesis have a bandgap energy difference between the well and barrier of ~ 2eV, since the band-gap energy of ZnSe is 2.823eV and that of MgS is ~4.8eV (77K). These materials form a type I QW structure [37], where wells are formed in the same material in both the conduction and valence bands.

PL measurements were carried out using the 3500Å line of an argon ion laser focused onto a LN2 cooled sample contained within a cryostat. The resulting emission generated in the sample is detected using a GaAs photomultiplier tube. The experimental setup is shown in figure 2.12.

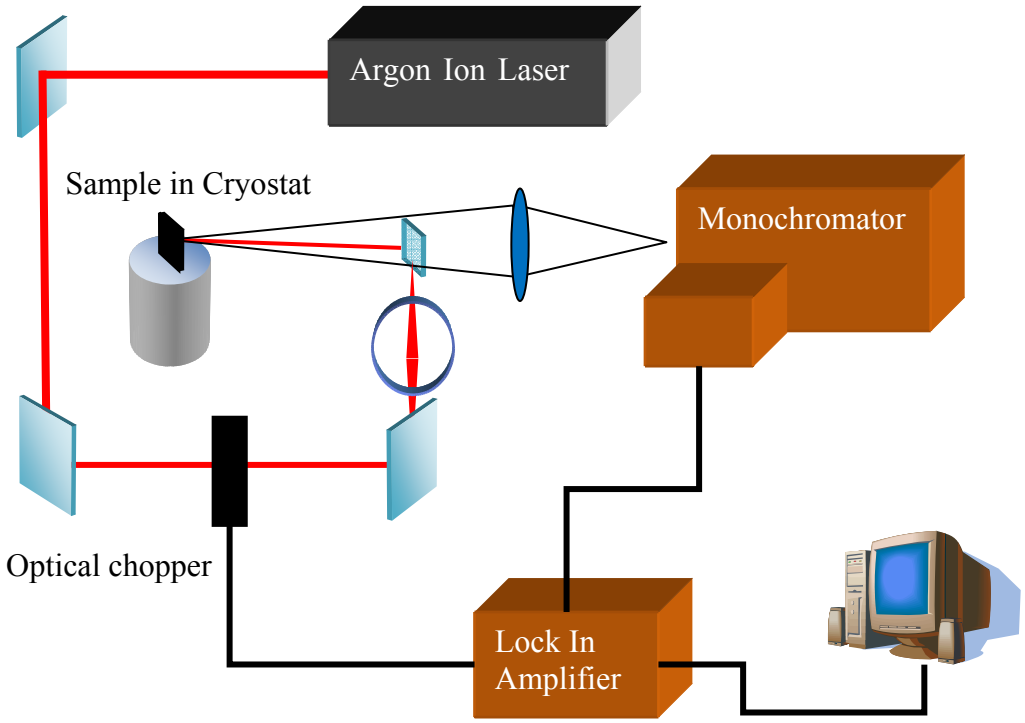

Figure 2. 12 *Experimental setup for PL measurements.*

2.5 Transmission Electron Microscopy (TEM).

One of the final characterization techniques used to examine a few select samples is TEM, specifically High Resolution TEM (HRTEM). In this section a brief explanation of the process is given with reference to more detailed work carried out on some of the previous Heriot-Watt samples.

Currently there are no TEM facilities within our group, however under the Self-Assembled semiconductor Nanostructures for new Devices in photonics and Electronics (SANDiE) collaboration our group supplied samples to the Departamento de Cienciadelos Materialese Ingeniería Metalúrgica y Química Inorgánica, Universidad de Cádiz who specialize in TEM studies. They were particularly interested in investigating our samples as very little investigation has been carried out on zinc blende II-VI metastable sulphides.

In basic principle an electron microscope works in much the same way as a regular optical microscope with the obvious difference in irradiation source. Both optical and electron microscopes have a limiting resolvable distance determined by the wavelength of the source which in the case of an electron microscope is the de Broglie wavelength of the electron. As this wavelength is ~ Å's in length it allows for resolvable images as small as 10's Å and magnifications up to $2x10^6$X. To focus and direct the electron beam an arrangement of electrostatic and electromagnetic lenses are used. In the case of TEM the focused beam is irradiated onto a sample and its transmitted image captured on a CCD below the sample.

Preparation of the samples is crucial to ensure good high quality images while avoiding unnecessary damage to the structure. Thinning of the sample through a range of first, mechanical then ion and chemical etching is required in order to obtain thin enough samples for electron transparency. The properties of the materials that Cadiz was studying (MgS and ZnSe) however required the development of new preparation techniques. As ZB MgS is a metastable material whose preferred structure is rocksalt it is especially susceptible to mechanical stress, degradation through oxidisation and can loose its ZB structure under ion bombardment.

Samples are milled and dimpled down from original thickness to ~20μm, this mechanical grinding is then improved upon by using Ion milling. In order to limit the introduction of point defects in the material the ion milling process is done using decreasing ion voltages from 4 to 2kV. Decreasing angles of incidence for the ion beam are used to further reduce the chance of damage to the material. During the process the sample holder was cooled to 77K. A more detailed explanation of this process can be found in references [12,38].

TEM was used in this thesis to examine in detail the structure of the quaternary alloy ZnMgSSe, exploring the interfaces and crystal purity in order to further confirm some of the data that other characterization techniques had generated. The details of this can be found in chapter 5.

2.6 Summary.

This chapter has presented an overview of the most important characterization process used throughout this thesis, with emphasis on the X-ray and RHEED methods as they are the prominent techniques used and provide the most comprehensive data for initial material development. It can be seen that individually each technique has its merits but together they provide a more detailed description of the materials. X-ray, RHEED and AFM studies were carried out in house with PL being performed at Heriot Watt by the nano optics group and TEM by the University de Cadiz, for which I am grateful. In chapter 3 X-ray interference measurements are used to characterise CrS with the view to develop novel ferromagnetic semiconductors. Chapter 4 will discuss the surface morphology of MgS by using a combination of RHEED analysis and AFM measurements. The final experimental chapter utilises all of the aforementioned characterisation techniques to fully characterise a new material with the aim of incorporating the material into novel epitaxial lift-off structures.

2.7 References.

[1] L. Tapfer, K. Ploog, Phys. Rev. 40 (1989) 9802

[2] B. K. Tanner, J. Phys. D: Appl. Phys. 26 (1993) A151

[3] C. Bradford, C.B. O'Donnell, B. Urbaszek, A. Balocchi, C. Morhain, K.A. Prior and B.C. Cavenett, Appl. Phys. Lett. 76 (2000) 3929

[4] M. Funato, A. Balocchi, C. Bradford, K. A. Prior, and B. C. Cavenett, Appl, phys letter 80, 3, (2002) 443-445

[5] M. Funato, K. Omae, Y. Kawakami, Sg. Fujita, Phys Rev B, 73, (2006) 245-308

[6] G. Binning, C. F. Quate, Ch. Gerber, Phys Rev Lett, 56, 9, (1986)

[7] R.T. Moug, C. Bradford, K.A. Prior, J. Cryst Growth, 301–302 (2007) 289–292

[8] K. Menda, I, Takayasu, T. Minato, M. Kawashima,Jap. J. of Appl. Phys, 26, 8, (1987) 1326-1329

[9] J.M. van Hove, P.R. Pukite, P.I. Cohen, J. Vac. Sci, Technol, 3, 2, (1985) 563-567

[10] R.T. Moug, C. Bradford, K.A. Prior, J of the Korean Phys Soc, 53, 5, (2008), 2996-2999

[11] J.B.Clegg, Surface and Interface Analysis, 2, 3, (1980) 91-95

[12] A.M. Sanchez, J. Olvera, T. Ben, J.K. Morrod, K.A. Prior, S.I. Molina, Appl. Phys. Lett. 89 (2006) 121907

[13] J.K. Morrod, T.C.M. Graham, K.A. Prior, B.C. Cavenett, J. Cryst Growth 278 (2005) 278–281

[14] B. W. Batterman and H. Cole, Rev. Mod. Phys., 36 (1964) 681-716

[15] D. K. Bowen, B. K. Tanner, High Resolution X-ray diffraction and topography. Taylor and Francis 1998

[16] W. L. Bragg, Proc. Roy. Soc. A, 89 (1913) 248-291

[17] C. Bradford, C. B. O'Donnell, B. Urbaszek, C. Morhain, A. Balocchi, K. A. Prior, B. C. Cavenett Phys Rev B, 64 (2001) 195309

[18] H. Holloway, J. Appl. Phys. 67, (1990), 6229

[19] R.W. James, The Optical Principles of the Diffraction of X-rays, OX Bow Press, Connecticut, 1982

[20] Z.G. Pinsker, Dynamical Scattering of X-rays in Crystals, Springer-Verlag, New York, 1978

[21] S. Takagi, Acta. Cryst., 15 (1962) 1311-1312

[22] D. Taupin, Bull. Soc. Fr. Mineral. Cristallogr., 87 (1964) 469-511

[23] N. Loxley, D.K. Bowen and B.K. Tanner, presented at 1990 Fall MRS meeting, Channel Cut Collimator Reference and Instruction Manual

[24] P. J. Dobson, An Introduction to Reflection High-Energy Electron Diffraction, in Surface and Interface Characterisation by Electron Optical Methods, edited by A. Howie and U. Valdre, Plenum Press, 1988

[25] M. G. Lagally, D. E. Savage and M.C. Tringides, Diffraction from disordered surfaces: an overview in Reflection High – Energy electron

diffraction and reflection electron imaging of surfaces, edited by P.K. Larson and P.J. Dobson, Plenum Press, 1988

[26] B.A Joyce, J.H. Neave, P.J. Dobson, P.K. Larson, Phys. Rev B 29, 814, 1984.

[27] E. A. Wood, J. Appl. Phys. 35 (1964) 1306

[28] Dimension 3100 Manual, Digital Instruments (2000)

[29] S. H. Xin, P. D. Wang, Aie Yin, C. Kim, M. Dobrowolska, J. L. Merz, J. K. Furdyna, Appl Phys lett, 69, (1996), 3884

[30] K.A. Prior, C. Bradford, L. David, X. Tang and B.C. Cavenett, J Cryst growth, 275, (2005), 141-149

[31] Franz J. Giessibl, Rev Modrn Phys, 75 (2003), 949-978

[32] B. Urbaszek, A. Balocchi, C. Bradford, C. Morhain, C. B. O'Donnell, K. A. Prior, B. C. Cavenett, 77, 23, (2000), 3755-3757

[33] T. Yao, M. Ogura, S. Matsuoka and T. Morishita, Jpn. J. Appl. Phys., 22(1983), L144

[34] T. Yao, J. Cryst. Growth 72 (1985), 518

[35] S. Desmond Smith, Optoelectronic Devices, Prentice Hall,1995

[36] Physics of Semiconductors, ed. B. Sapoval and C. Hermann, Springer-Verlag, 1995.

[37] Semiconductor Optics, ed. C. F. Klingshirm, Springer-Verlag, 1997

[38] N. Wang and K. K. Fung, Ultramicroscopy 60, 427,1995

Chapter 3

Growth of (Zn,Mg)S/CrS multilayers on GaP substrates.

3.1 Introduction.

Work developing sulphur containing compounds has been at the core of II-VI research at Heriot-Watt University for some time. Studies have included the growth of ZnS [1], continuing with development of MgS [2], MnS [3] and recently MnCrS [4]. The ability to grow these novel sulphur containing compounds in their metastable zinc blende (ZB) crystal structure is largely due to the growth technique, whereby a compound ZnS source is used as the only source of sulphur. Previously, successful growth of MnS and MgS has been achieved using other sulphur sources [5,6], however investigations into compound ZnS as the sulphur source have shown improved results [7].This compound source ensures the lowest possible sulphur overpressure and a metal rich growth regime.

To be successful this growth method requires that the metal to be incorporated has a much lower vapour pressure than Zn and the growing material is a close lattice match to the substrate. Under optimum growth conditions it is believed that a thermodynamically preferable reaction takes place at the surface, replacing Zn and allowing growth of ZB MgS, MnS and CrS. A more detailed explanation of this method in relation to MgS is covered in chapter 4.

The motivation into researching sulphur containing compounds is due, in part, to their large band gap, making them suitable as barrier material in both quantum well and quantum dot structures but also, more recently, due to their predicted suitability for the fabrication of ferromagnetic semiconductor structures. The range of useful properties include: wide band gap etch-soluble MgS [8,9], antiferromagnetic MnS [10], and the recently predicted ferromagnetic CrS [11]. The majority of research into these compounds has been on GaAs substrates as both MgS and MnS have lattice parameters

close to that of GaAs. However both ZnS and CrS [4] have lattice parameters better matched to GaP, generating difficulties in both their growth and characterisation; these issues will be discussed in this chapter.

Motivation for the studies discussed here, derives from the field of spintronics; Dietl predicted that that unlike the antiferromagnetic MnS, CrS, would be ferromagnetic with a high Curie temperature [11], based on previous work by Blinowski [12]. Interest in this material led to the award of an EPSRC research grant at Heriot-Watt in 2003. The main goal of this study was to try and deposit a CrS layer ~100Å thick to measure any magnetic properties. These measurements were to be done in conjunction with Dietl *et al* at the Polish Academy of Sciences (PAS), Warsaw, Poland.

In developing a new material system the ability to characterise the material at each step is critical. For the optimisation of new materials XRI measurements were used on thin samples to achieve a measure of thickness and composition (details discussed in chapter 2). This allows informed alterations of growth parameters including flux and substrate temperature. Due to the interference properties of X-rays and the sample design very thin layers ~ few nm can be characterised [13,14,15]. However, in some cases, the XRI system cannot be easily employed, making characterisation difficult. CrS is such a material as will be demonstrated in this chapter.

3.2 Previous research into transition metal sulphides.

Preliminary work on this material was carried out by Dr Lorraine David as part of her 2006 PhD thesis. Some of the key research aspects that were undertaken are:

- Firstly, cleaning of the Cr source material. It was found that during outgasing of the source material the pressure would increase beyond safe operating levels, and as such, the outgasing was undertaken in cycles. A digital heat cycle was employed to clean the 5N pure source used.

- Selection of a substrate: As the lattice parameter at this stage was unknown, Dr K Prior estimated from tabulated atomic radii that a_{CrS} = 5.806 Å. This lattice parameter is closest matched to InP. Initial growths on InP did not reveal any layer in X-ray diffraction so the lattice parameter was determined experimentally.

- Determination of a_{CrS} from the growth of MnCrS: This alloy of MnCrS was grown with varying Cr concentrations to obtain a_{CrS} = 5.387 ± 0.025Å [4]. This lattice parameter is closest matched to GaP and therefore a new set of studies were undertaken on this substrate.

Thin layers of CrS with ZnS cladding grown on GaP substrates were examined using XRI. However using the initial value of a_{CrS} previously predicted, the conditions for Pendellösung fringes, and using equation 2.32 from chapter 2 with the lattice constants of CrS (5.378Å) and ZnS (5.4102Å), it was seen that the thickness of the layers being grown would be less than the minimum resolvable thickness for fringes ~10Å. At this stage this thickness was believed to be greater than the layer thicknesses grown. For this reason work on the ZnS cladding layers was halted and the use of ternary ZnMgS as the cladding was investigated. This allowed an increase in the cladding lattice parameter, and therefore a decrease in the minimum thickness for fringe observation. Using this ternary as the cladding, CrS thicknesses of ~30Å were observed in the XRI data initially obtained. By using these structures and optimizing the simulation parameters of the BEDE system a more accurate value of 5.353 ± 0.0025Å for the CrS lattice constant could be realised.

At the start of this investigation the initial work was reproduced in samples HWA1988-HWA2001. Although the XRI results were reproducible with similar traces, on closer inspection of the simulations which had been produced there appeared to be a potential ambiguity in the results. As the BEDE software is a modelling tool, all input variables have to be accurately defined by the user. As both the lattice parameter and the Poisson's ratio of CrS were estimated there was already an inherent uncertainty in the simulations. More worryingly, by varying the thicknesses and composition it was observed that there was more than one acceptable fit to the experimental data. This is shown in Figure 3.1. and 3.2. Figure 3.3 demonstrates that when the [115] direction was scanned the simulation generated does not fit with the data.

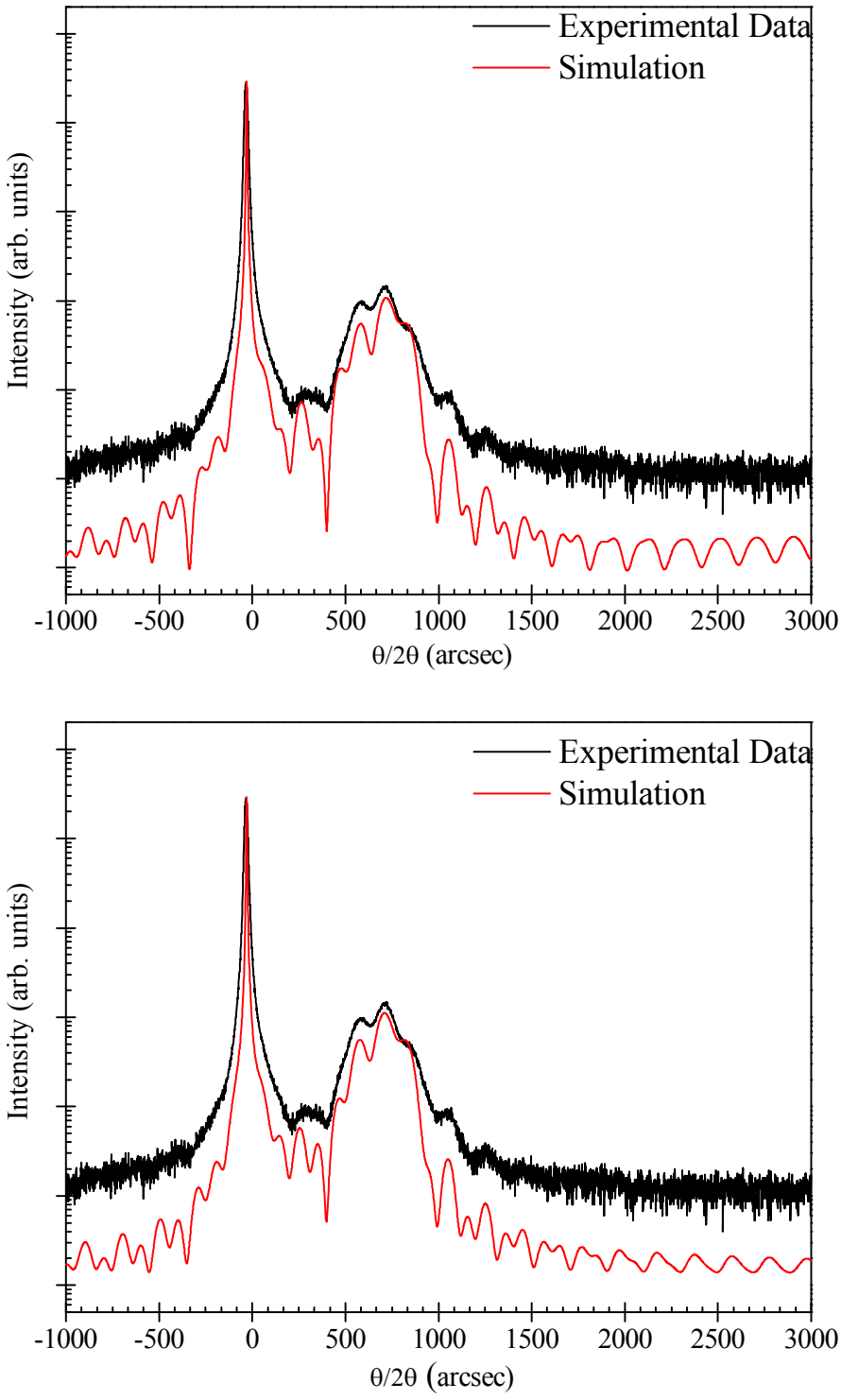

Figure 3. 1 *(Top) Initial simulation of sample no HWA1922 showing ~30Å of* $Zn_{0.03}Cr_{0.97}S$*, (bottom)showing a similar fit can be achieved with varying CrS composition as shown in figure 3.2.*

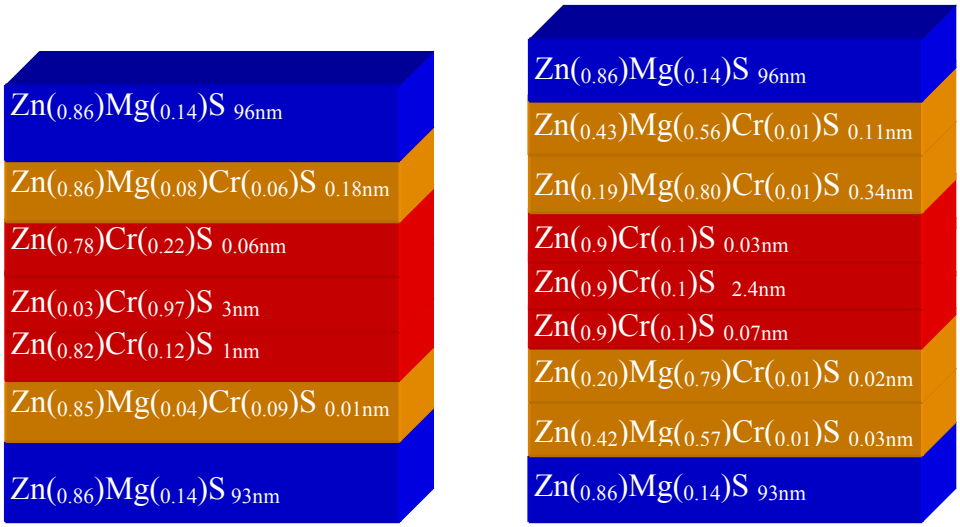

Figure 3. 2 *Structures generated from XRI simulations. Left corresponds to structure proposed previously. Right is the structure from alternative simulation with less Cr which features the same trace.*

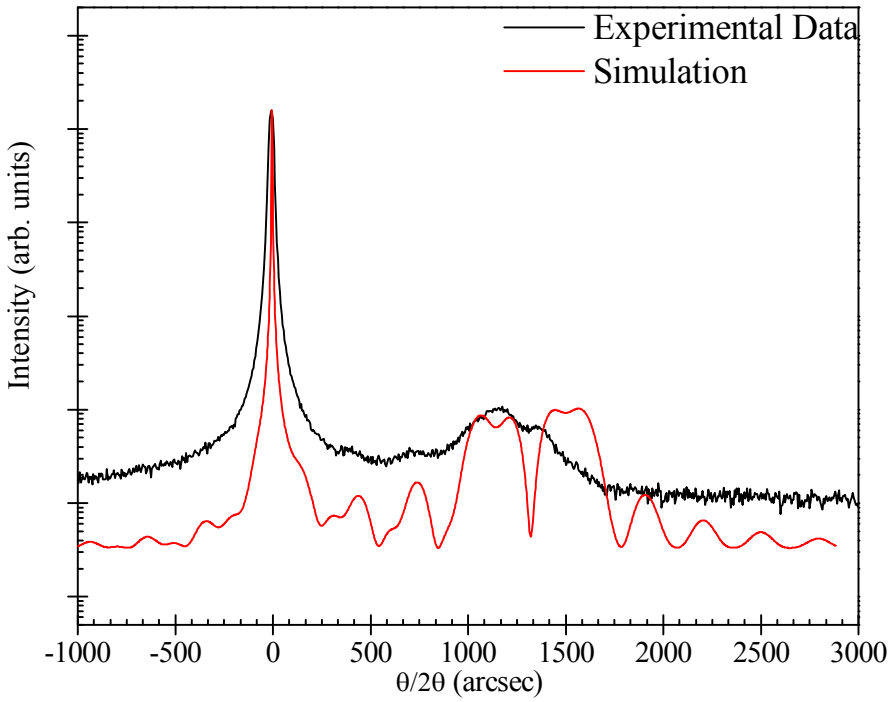

Figure 3. 3 *[115] XRI scan of sample no HWA1922 with simulation generated from the structure proposed previously.*

Reasons as to why an accurate simulation of the data was not attainable and the attempts made to correct this and the structure for PAS are the main motivations in this chapter.

3.3 Growth of ZnMgS/CrS multilayers.

As mentioned previously the driving force behind the research into CrS was to make magnetic measurements in order to verify the prediction that CrS was ferromagnetic. To achieve this, a CrS thickness in the region of 100Å was required. Due to the problem of the ambiguity in the deposited layer thickness, a decision was made to try and simulate a superlattice structure of ZnMgS/CrS. By adding many repetitions of ZnMgS/CrS more interference fringes would be apparent in the rocking curve data and would increase the chances of obtaining an accurate description of the structure, including the CrS layer thickness.

One of the considerations to be addressed before growth of the superlattice could commence was the strain thickness product of the structure. P. Kidd *et al* [16] observed that as the thickness of the layers increases beyond a critical value the strain decreases according to $\varepsilon h = K$ as shown in Figure 3.4, then, will become predominantly relaxed.

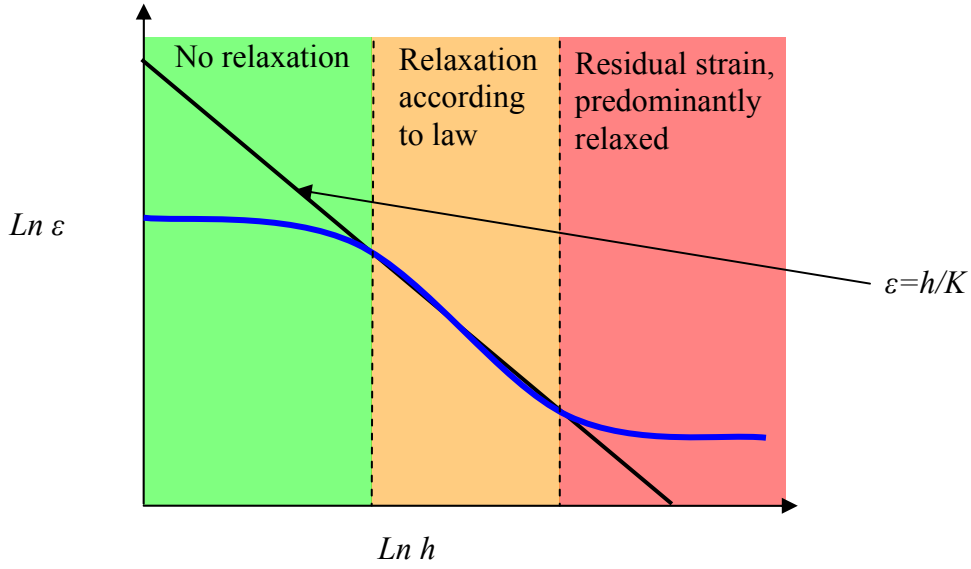

Figure 3. 4 *Schematic diagram illustrating the relationship: ε = h/K (line) [16]*

For multilayer structure with n individual layers of thickness h_i and strain ε_i the average strain is defined by:

$$\bar{\varepsilon} = \sum^{n} h_i \varepsilon_i \Big/ \sum^{n} h_i \qquad \text{Equation 3.1}$$

and $$h = \sum^{n} h_i$$ Equation 3.2

Form this, the critical thickness conditions become

$$h\bar{\varepsilon} \leq K$$ Equation 3.3

This allows the maximum thickness of the superlattice to be estimated if the growth rate and composition of the ZnMgS alloy and the maximum obtainable thickness of CrS are known.

3.3.1 Growth of CrS.

All samples in this section were grown on (100) GaP wafers purchased from University Wafer. As only a small batch of these wafers was available they were cleaved into eighths. To remove the surface oxide layer, samples were etched in a 15:5:5 solution of $HCl:HNO_3:H_2O$ for 120 seconds at room temperature [5], subsequently rinsed in 18MΩ deionised water and dried quickly with nitrogen gas. Using a thin layer of indium the samples were secured to a molybdenum substrate holder *via* surface tension. Before transport to the growth chamber any absorbed water was desorbed by rapid heating to 200^0C.

The sources used for this study were 6N purity Mg, Zn and ZnS, with the 5N purity Cr source mentioned previously. For the Cr and ZnS sources LN_2 cooled shutters were used to reduce the outgassing generated from the high temperature cells. These sources were raised to the appropriate temperatures prior to the sample being transported to the growth chamber. This was done so that flux measurements could be taken before the sample oxide layer was removed and to minimise surface contamination.

After degassing the samples were transferred into the growth chamber where the thin oxide layer, which forms on the surface during indium mounting, was removed by heating the sample to around 580-620^0C. As a III-V substrate is used in a II-VI chamber, a Zn flux was applied to the surface during heating. In the absence of Zn flux, sulphur can attack the GaP surface forming Ga_2S_3, and create areas of high dislocation density due to large lattice mismatch [17].

Once the sample reaches the desorption temperature a 4x RHEED pattern is observed along the [011] azimuth. At this point the substrate temperature is reduced to the growth temperature of 180^0C. During the cool down the substrate is left exposed to a Zn flux to prevent further Ga_2S_3 formation whilst retaining the flat ordered surface indicated by a 4x RHEED pattern. However, as Zn condenses at ~ 200^0C there is a temperature window where no Zn flux can be used and an increased chance of attack from sulphur is incurred.

In order to achieve successful growth of CrS on GaP this was one of the main issues to tackle. One of the methods used was to slowly reduce the Zn flux towards the end of the cool down period. This was timed so that the flux would be reduced when the sample temperature reached 190^0C and be negligible by the growth temperature of 170^0C. This was successful in maintaining the 4x RHEED pattern down to the growth temperature, however produced little improvement in the quality of growths undertaken afterwords.

From the previous work it was found that raising the temperature after the growth of the ZnMgS layer for the CrS layer improved the growth. As Cr has such a high evaporation temperature (~ 1000^0C) during low temperature growth (180^0C for ZnMgS) it was thought that there would not be adequate surface migration to sustain 2D growth.

Due to this the growth of the ZnMgS/CrS layers needed to be halted for ~ 15-20 minutes before the growth of the CrS layer, during which the growth temperature was increased from 180^0C to 320^0C. Once the growth of CrS was finished the growth temperature was reduced back to 180^0C for the next layer of ZnMgS.

Initially a sample of GaP/ZnMgS was generated in order to determine the growth rate and composition of the cladding layers. The resultant XRD scan is shown in figure 3.9.

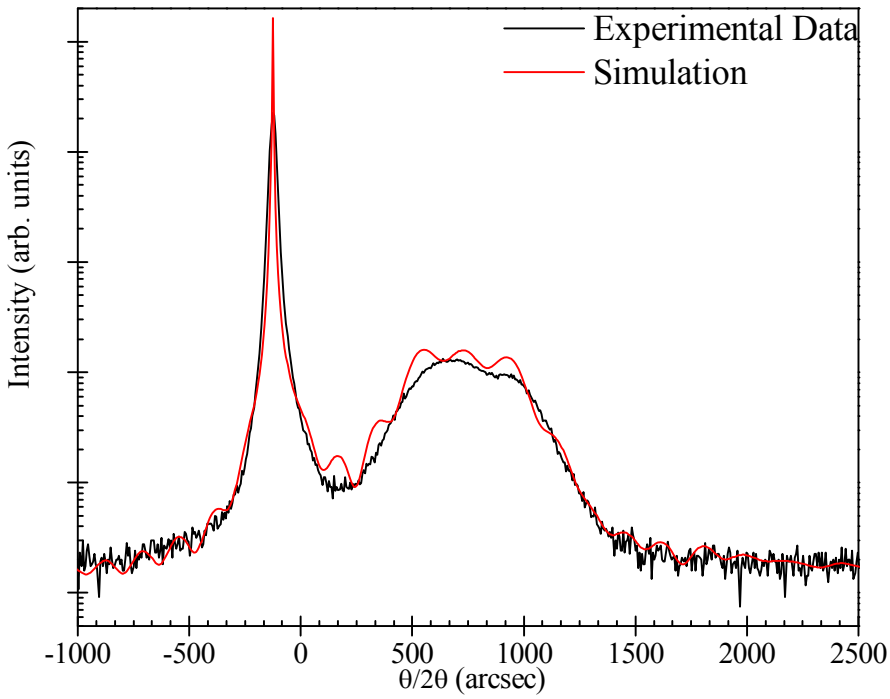

Figure 3. 5 *XRD spectrum of HWA1999 with simulation in shown in red.*

When simulated a growth rate of 0.67 Å/s and a composition of $Zn_{0.86}Mg_{0.14}S$ was obtained from the secondary peak height and position. It can be seen from the simulation in red that this is not a perfect fit; however for the purpose of gathering the growth rate this was a good enough estimate.

Using equation 3.4 a critical thickness in the region of 2000Å is derived from the critical thickness of ZnSe and using the value 0.4 for *k*, which appears to be an acceptable choice for a variety of II-VI alloys [18]. So for these structures a cladding thickness of ~300Å with 5 repetitions was chosen as it simulated the best fringes, allowed for ~100Å of CrS growth, and maintained a total thickness less that 2000Å. A schematic diagram of the structure and the simulation generated are shown in Figure 3.6

Previous CrS calibration growths showed a sharp and streaky RHEED pattern for approximately 30s before the pattern changed to spotty and diffuse. This is an indication that the growing layer is initially flat but had converted to a 3D growth mode. Therefore in these structures in order to maintain a flat surface throughout the growth the time for the CrS layer was reduced to 20s.

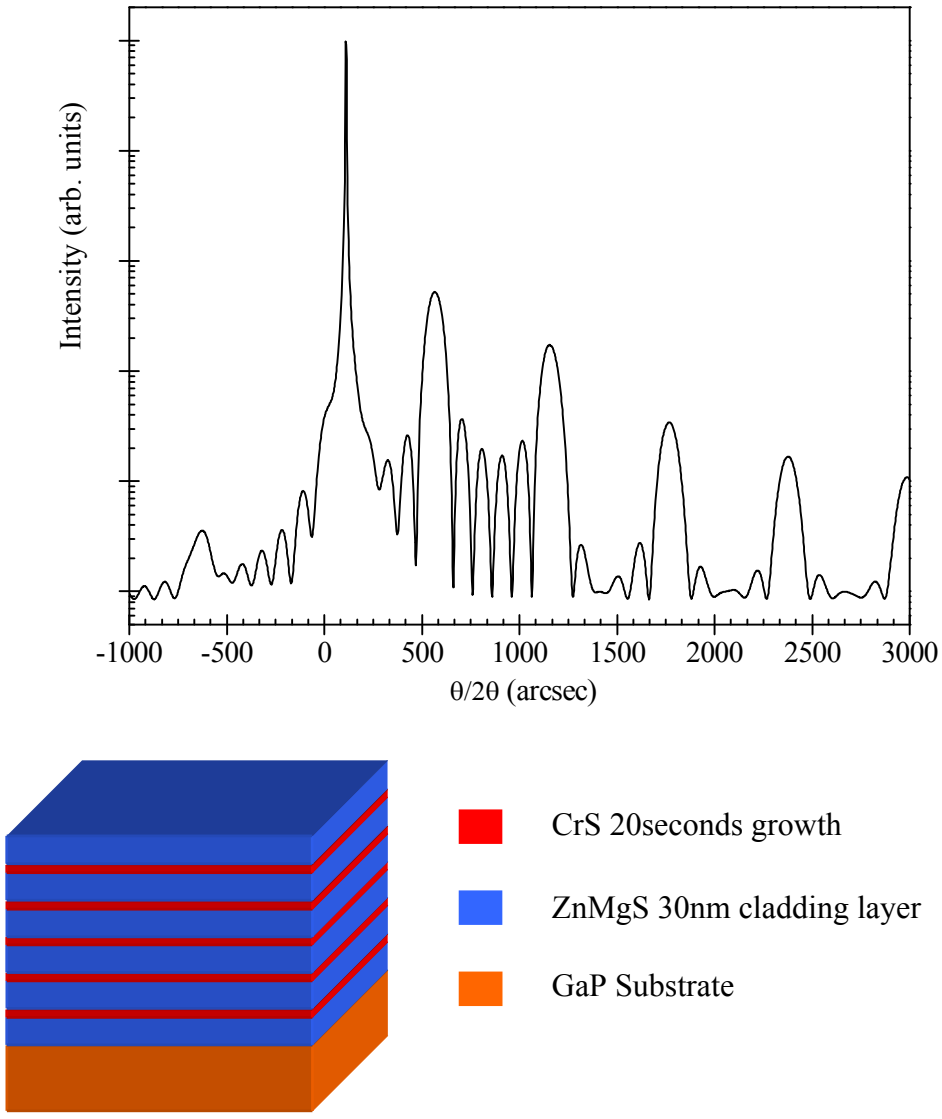

Figure 3. 6 *Simulation of the GaP/(ZnMgS(300Å)/CrS)x5 superlattice with the structure presented below.*

3.3.2 Analysis of ZnMgS/CrS Superlattice.

As with all the samples in this study characterisation using DXRC was employed. After the sample had been grown, a section of the structure was cleaved and an X-ray rocking curve spectrum obtained using the BEDE DXRC system. X-ray scans were done with a step size of 2 arcseconds and a sample rate of 25 seconds per step. This was done to improve the resolution of the fringes. The resulting spectrum and simulation is shown in Figure 3.7.

It is apparent that the graph shows no fringes at all. This was puzzling as the main goal of this sample was to generate better resolved fringes, providing enough information to make an accurate model of the structure.

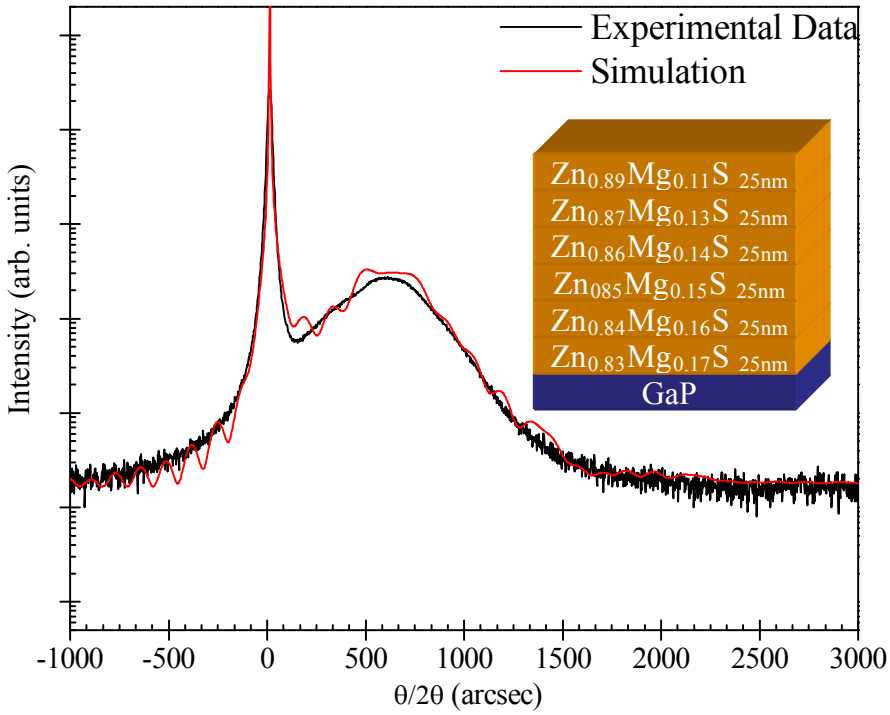

Figure 3. 7 *XRI spectrum and resultant simulation of HWA2002 ZnMgS/CrS superlattice. Insert shows simulated structure.*

Models of the structure were investigated with different causes; from abnormal strain gradients across the layers, fluctuating thickness, to composition variations. It was found that the best match to the spectrum was changes in the Mg mole fraction in the ZnMgS of ±3% and was presumably caused by small fluctuations in the growth temp of only a few degrees. This was unfortunate but not unexpected due to the temperature changes required during growth.

One significant observation was the ~100 arcsec shift to the left in peak position from bulk ZnMgS to the CrS modulated ZnMgS superlattice, indicating partial relaxation. This highlights that there must be another material in addition to ZnMgS inducing dislocations and defects as this structure was designed to remain below the critical thickness.

3.4 Growth of ZnS/CrS superlattice.

Due to the observation that a small change in the composition of the cladding layer could smear out the fringes a decision was made to revert back to ZnS cladding layers. This would avoid the problems associated with a ternary material. As mentioned previously ZnS was initially rejected as a cladding material as its strain was similar to CrS and very thin spacer layers would not produce discernable XRI fringes. However when a newly predicted value of a_{CrS}=5.353Å was obtained [19] a new minimum thickness for fringe observation was determined. This in turn generated a lower minimum detectable layer thickness below 10Å and thus allows for the possibility of thinner CrS layers to be investigated. As with ZnMgS, a calibration sample of a thick ZnS layer was required in order to measure the growth rate. The resulting XRD spectrum is shown in figure 3.8

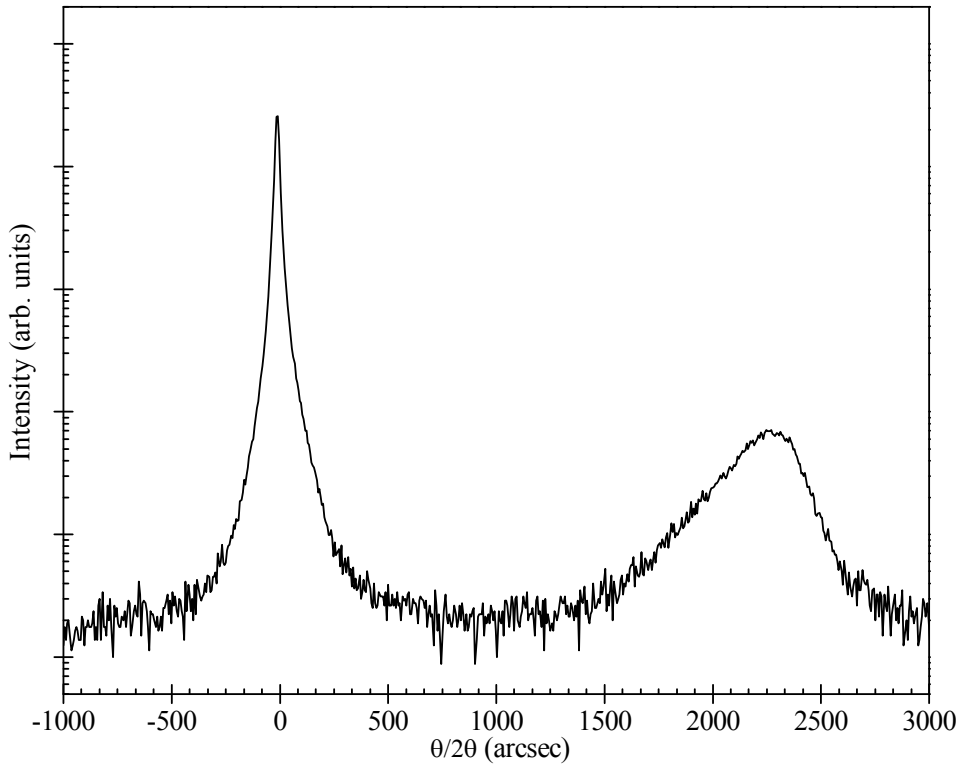

Figure 3. 8 *XRD scan of ZnS calibration layer (HWA2018)*

This data gave us a rough estimate for the growth rate from the peak intensity and position. However the asymmetric ZnS peak in the graph was not expected. This feature

was interesting but thought at this time to be a negligible effect in the development of the superlattice and work continued using ZnS. A possible explanation for this asymmetry and its consequences are discussed in section 3.5 of this chapter.

In a similar fashion to that of ZnMgS the strain thickness product of ZnS/CrS was re-calculated using the new value of a_{CrS}. From this a max thickness of 580Å was found, less than was needed to show well resolved fringes and therefore there was a possibility that the ZnS cladding layers would be partially relaxed. This relaxation would be further increased as the lattice constant of CrS is larger than ZnS. These inherent factors could not be ignored but as a last effort to provide the 100Å of CrS required by PAS, the ZnS/CrS superlattice was investigated.

Using the growth rate of 0.43Å/s found from HWA2018 and the critical thickness of ~600Å, a growth time of 5 min per layer of ZnS with 6 repetitions was chosen. This was decided to be the best possible chance of demonstrating fringes using ZnS whilst remaining below the critical thickness. As with the previous structure the CrS layer was grown for 20 seconds at 350^0C. A schematic diagram of the structure is shown in figure 3.9

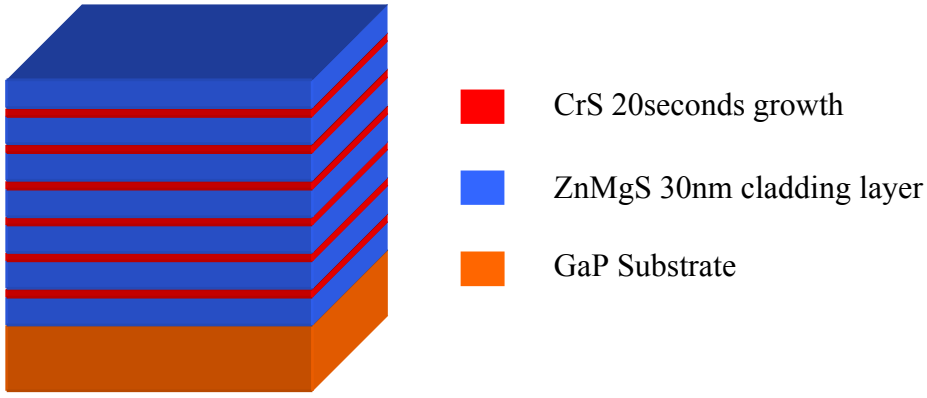

Figure 3. 9 *Schematic of the ZnS/CrS superlattice used for the growth of sample HWA2029*

The resultant XRI spectrum is shown in Figure 3.10. Yet again there were no fringes. There was however a shift in the peak position and an increase in the FWHM of the substrate peak which has developed a shoulder as indicated in figure 3.10. The shift in peak position was a good indication that there was a second material present with the

ZnS while the broadening of the GaP substrate peak is known to be caused by an increase in misfit dislocation density [20].

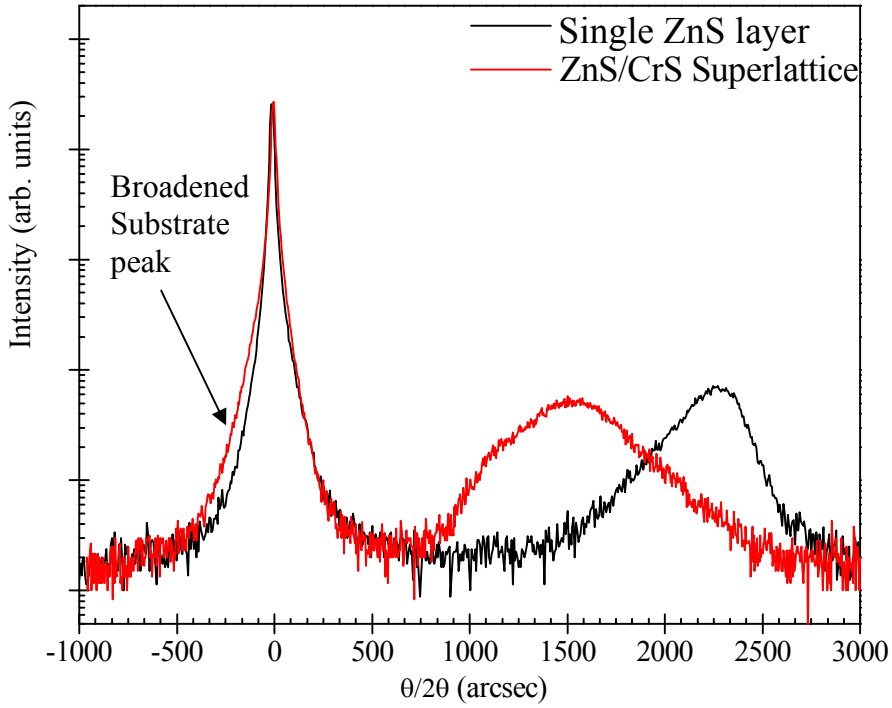

Figure 3. 10 *XRI spectrum of HWA2029 (red) and XRD spectrum of HWA2018 (black) showing the shift in the epilayer peak position and the broadening of the substrate peak.*

This sample was sent to Professor Dietl's group at Warsaw, however the results of their measurements are still pending. At this point the growth of sulphur containing compounds on GaP stopped. However, investigations into why these materials proved so difficult to characterise were undertaken.

3.5 XRD simulations of CrS containing layers grown on GaP.

The key to improving the growth of the sulphur containing compounds was to fully characterise the previous XRD data that samples had produced. In order to do this first an understanding of the simulation software and its limits needed to be acquired. Initial ideas as to why the epilayer peaks were lacking in structure included: 1) the strain relationship between cladding and spacer layer being such that relaxation occurs below

expected thickness, 2) the lattice parameter of CrS generated *via* the BEDE GOF procedure may be incorrect, 3) the relationship between strain in the x-y and z directions and any tilt generated by substrate miss-cut.

In the BEDE software system it is possible to input strain variables into the simulation. By introducing strain into the simulation changes in the simulated composition and thickness are observed. This is a very useful tool if the strains and Poisson's ratio are known for the material. However, with ZB CrS the material parameters were generally unknown; therefore finding suitable strain profiles was difficult.

The software can model a layer graded in composition or strain by dividing the layer into laminae of equal thickness, but having one compositional variable varying as a function of Z, the height within the layer. The function can contain any trigonometric or hypertrigonometric function, it also has the capability to use power laws and natural logs. For this analysis the linear, exponential and parabolic functions were applied to the layers in an attempt to better simulate the XRD data.

Both the ZnMgS and ZnS single layer XRD scans showed asymmetric peaks and therefore it was decided that these would be the best structures to initially simulate. If these were modelled successfully then a large number of variables could be removed from the CrS XRI scans reducing the amount of ambiguity in the simulation.

The samples were grown for calibration of their composition and total thickness; therefore they are well above the critical thickness for pseudomorphic growth on the substrate. Beyond this thickness the layer slowly relaxes, resulting in separate regions of differing strain. This was one of the initial suggestions as to why the XRD was not symmetrical. However, when different strain profiles were tried, even functions such as logs and exponentials, a good fit of the data was still unattainable.

One of the main problems with the growth of II-VI structures on III-V substrates as previously mentioned in section 3.3.1, is the initial nucleation of the II-VI compounds on the substrate. In the GaP/ZnS system this is made difficult by the background S_2 residual pressure and the heat clean procedure for GaP occurring without excess phosphor. This leaves the sample at risk of forming disordered submonolayer domains of Ga_2S_3 resulting in domains of ZnS with differing strains and dislocation densities. As

Ga_2S_3 is a cubic structure closely related to ZB, formation of Ga_2S_3 is not noticeable by RHEED.

These regions with different strains will smear out the diffracted pattern. A schematic is shown in figure 3.11 to try and show this effect.

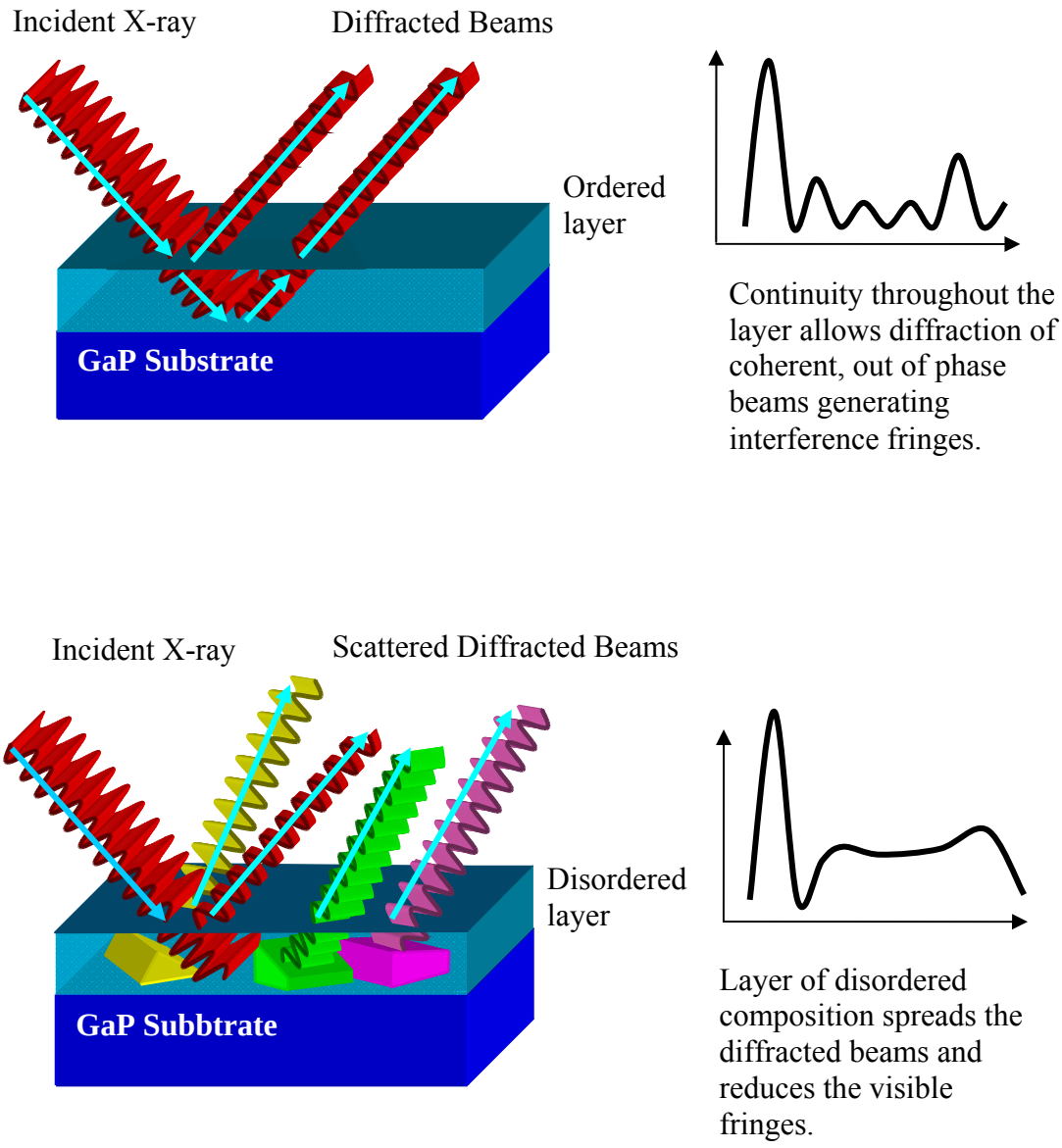

Figure 3. 11 *Schematic diagram of (top) scattering from a surface with one strain state, generating an XRD spectrum with well resolved fringes and (bottom) a surface with regions which have different strain states (shown as yellow, green and purple) which produce a smeared out XRD spectrum lacking in resolvable fringes.*

Unfortunately the profiling of these strain variations is not possible in the BEDE system. Strain is input as a function of *z* and the software assumes the layer is of continuous composition across the *x*-*y* plane.

To try and simulate this structure a weighted average function needs to be applied in order to incorporate the variations in strain throughout the layer. This technique first requires the XRD spectrum to be matched as closely as possible with the simulation available in software. This simulation is then repeated with a different strain. As the strain affects the position of the epilayer peaks in the simulation, only strains were used that would generate a peak shift within the confines of the experimental peak. This range, when averaged, would combine the weighted intensities while maintaining the superposition of the peaks. To combine the simulations in a way that reflects the structure each strain simulation is weighed according to the physical probability of finding such values in the structure. For example, the structure is unlikely to be completely relaxed and therefore large relaxation values are weighted less than smaller ones. By multiplying the adjusted strain values by the weighting factor then adding the results together a weighted average over the range of strain values can be obtained.

The task of finding suitable strain values and the corresponding weighting that each set had was set as a project for an MPhys student to undertake. This work was successful in proving the concept that the smearing of the XRD data was indeed due to the heterogeneity of the analysed layer. This can be seen in the simulation of the ZnS XRD scan shown previously in Figure 3.8. It can be clearly seen in Figure 3.12 that the superposition of two positive strains, 7.5% and 30%, when weighted in the ration 77.5:22.5 can fit the asymmetric shape of the peak. It was also promising that this fit was obtainable using realistic strains. It is also feasible that the introduction of a 3rd strain state would improve the fit even further.

With this method showing that a fit could be obtained for this previously un-simulatable structure the other X-ray spectra of similar shape and structure were tested. It was found that in most structures that the weighted average method would generate a fit far better than the BEDE software.

This analysis of these XRD spectra allowed a more detailed picture of why the post growth investigations into CrS structures were so difficult. From this model we can

surmise that the analysis of the growths of CrS was going to be hindered from the onset of heat clean. The formation of Ga_2S_3 on the surface will not only affect the cladding layer but will be even more prominent on the subsequent CrS layer due to the extra partial, but varying, relaxation present.

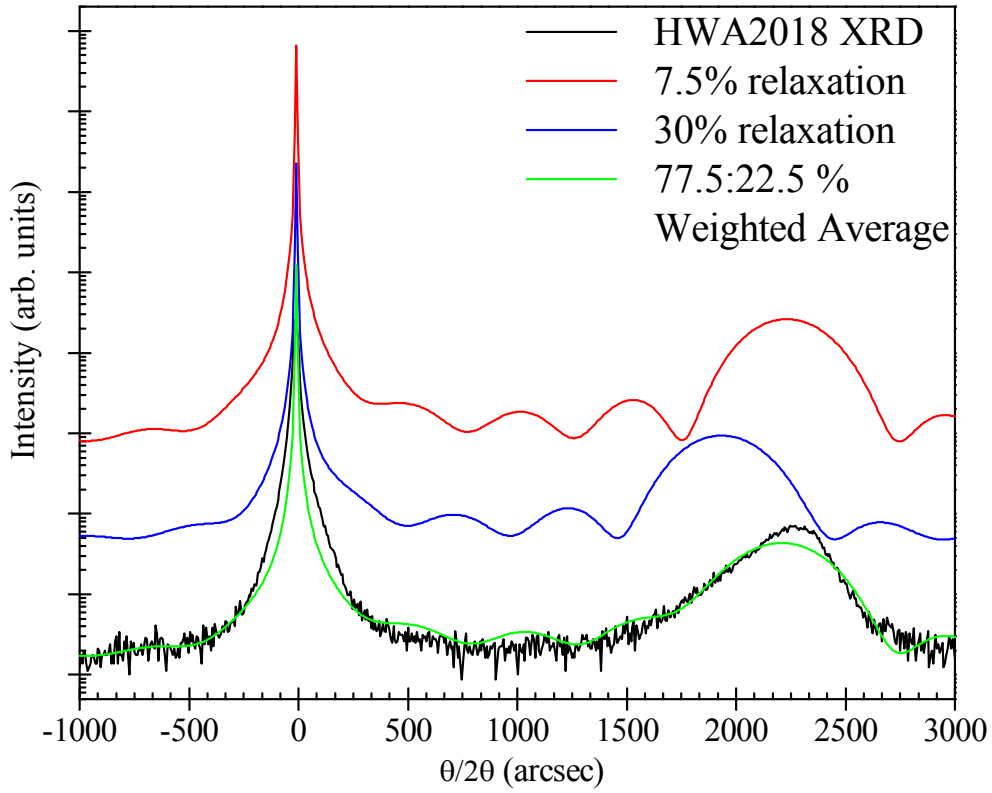

Figure 3. 12 *Initial XRD scan shown in black with the graph in green representing a weighed average combination of differing relaxation values.*

3.6 Conclusions and further work.

3.6.1 Conclusions.

Through this investigation a large amount of useful information has been generated about the growth of ZnS, ZnMgS and CrS deposited on GaP. From the absence of simulatable XRI scans and thickness calibrations, it has been seen that the main key to improving the growth of these materials is to make the initial GaP surface as free from sulphur as possible to make sure the substrate is atomically flat. Unfortunately the system as set up at the moment is unable to achieve this. As it can be seen there are domains with differing strain throughout the samples, and it can be surmised that the preparation of the sample during heat clean is the predominant factor in reducing the quality of the samples.

However the other issues highlighted in this study also play a part in the difficulties related to growing this material. For the ternary cladding layers it was seen that a very slight change in the growth temperature can change the Mg mole fraction enough to remove or obscure any XRI fringes that may have been generated. With the ZnS cladding layers the strain associated with the lattice mismatch is so high that relaxation is possible during the top cladding layer deposition. All of these factors contribute to the difficulties associated with the development of CrS containing structures in varying degrees and would need to be addressed independently in order to develop this material system further.

3.6.2 Further work.

Due to the completion of the EPSRC grant to investigate this material, work on its development has stopped; this however has not prevented various solutions to the problems from being suggested. This is especially important now that interest in the material has been revived, as now requests are arriving from international collaborators to use CrS in further structures for magnetic measurements with papers from the group of Prof Heimbrodt (Philips university Marburg) already in press [21].

As the protection of the substrate from interacting with sulphur seems to be the dominant issue with this system, capping the substrates with a group V element may be

the solution to this issue. However even this is fraught with problems as finding a suitable material to use is difficult. Predominantly this is because III-V substrates are being used in a II-VI chamber so care has to be made to avoid choosing a capping material that will affect subsequent depositions. Ideally the layer would be capped with As allowing for a low temperature heat clean and reduction in the S attack. However there are no studies where this has been done on GaP so capping of the substrate, although possible, is not the route that is best suited to this system.

Previous studies showed that by immersing a freshly etched sample of GaAs into ammoniumsulphide solution the layer can be capped with a monolayer of S atoms at room temperature. Passivation of the GaP substrate [22] using a monolayer of sulphur prevents any further reaction with the surface. This allows for a very low temperature heat clean as the gallium and phosphorus oxides are not present and eliminate the high temperature desorption where the surface is most at risk. However, this technique, when used for GaAs had poor reproducibility due possibly to the ammonium solution degrading with time [23]. As it is untested with GaP the level of improvement gained by using this technique is unknown but if it can improve the preparation of the sample by even a small percentage it may provide enough improvement so that a better understanding of the subsequent layers could be achieved.

A very high operating temperature was needed to obtain the relevant flux required for growth; unfortunately this resulted in a very high background pressure of N_2 from the boron nitride Knudsen cells during the CrS growth. This issue could be resolved with the installation of a tungsten crucible Knudsen Cell.

3.7 References.

[1] S.A. Telfer, C. Morhain, B. Urbaszek, C. O'Donnell, P. Tomasini, A. Balocchi, K.A. Prior, B.C. Cavenett, J Cryst Growth, 214-215, (2000), 197-201

[2] C. Bradford, C.B. O'Donnell, B. Urbaszek, A. Balocchi, C. Morhain, K.A. Prior, B.C. Cavenett, J Cryst Growth, 227–228, (2001), 634–638

[3] L. David, C. Bradford, X. Tang, T.C.M. Graham, K.A. Prior, B.C. Cavenett, J Cryst Growth, 251, (2003), 591–595

[4] L. David, K.A. Prior, Phys Stat Sol, 243, 4, (2006), 778–781

[5] N. Teraguchi *et al*, Appl Phys Lett, 67, (1995), 2945

[6] K. Uesugi *et al*, Appl Phys Lett, 68, (1996), 844

[7] K.A. Prior, S.A. Telfer, X. Tang, C. Morhain, B. Urbaszek, C. O'Donnell, P. Tomasini, A. Balocchi, B.C. Cavenett, J Cryst Growth, 227–228, (2001), 655–659

[8] C. Bradford, A. Currran, A. Balocchi, B.C. Cavenett, K.A. Prior,

R.J. Warburton, J Cryst Growth, 278, (2005), 325–328

[9] A Curran, J K Morrod, K A Prior, A K Kar, R J Warburton, Semicond Sci Technol. 22, (2007), 1189–1192

[10] T. Dietl, H. Ohno, Physica, E 9 (2001), 185-193

[11] T. Dietl, F. Matsukura, H. Ohno, Phys Rev B, 63, (2001), 195-205

[12] J Blinowski, P. Kacman and J.A. Majewski, Phys. Rev. B 53, (1996), 9524

[13] L. Tapfer, K. Ploog, Phys Rev B, 40, (1989), 14

[14] B K Tanner, J Phys D Appl Phys, 26, (1993), 151-155

[15] K.A. Prior, X. Tang, C. O'Donnell, C. Bradford, L. David, B.C. Cavenett, J Cryst Growth, 251, (2003), 565–570

[16] P. Kidd, D.J. Dunstan, H.G. Colson, M.A. Louren, A. Saceddn, F. Gonzhlez-Sanz, L. Gonzfilez , Y. Gonzfilez , R. Garch , D. Gonzfilez, F.J. Pacheco, P.J. Goodhew, J Cryst Growth, 169, (1996), 649-659

[17] Y. Chen, J. Washburn, Phys Rev Lett, 77 (1997) 4046-4049

[18] K. Prior, personal communication

[19] L. David, MBE Growth and Characterisation of Metastable Transition Metal Sulphides. 2006

[20] V. M. Kaganer, R. Köhler, M. Schmidbauer, R. Opitz, Phys Rev B, 55 (1997) 1793-1810

[21] W. Heimbrodt, L. Chen, H.A. Krug Von Nidda, A. Loidl, P.J. Klar, L. David, K.A. Prior, J Korean phys sol 53, 5, (2008), 2852-2856

[22] V. N. Bessolov, M. V. Lebedev, Semiconductors, 32, (1998), 1141-1156

[23] K. Prior, personal communication.

Chapter 4

A study of the MgS (100) surface.

4.1 Introduction.

MgS is an excellent barrier material for wide-gap II-VI quantum structures due to its large bandgap of ~5eV. Although MgS can be grown in the metastable zinc blende structure in layers up to 1400Å thick the maximum thickness which can be obtained is a sensitive function of growth rate, II-VI flux ratio and, most critically, substrate temperature. The optimum growth temperature occurs in a narrow range between 240-270°C and the maximum thickness decreases rapidly as the growth temperature is raised to 300°C [1,2]. Previously, the HW MBE group have shown that the development of large scale changes in the MgS morphology can be observed by RHEED, in particular, the observation of 1D nanostructures [3,4], and the conversion of MgS layers from zincblende to rocksalt [5]. The development of the MgS 1D structures is discussed in section 4.4 of this chapter.

Well before the onset of the phase change, the surface of the MgS layer develops 1D wires or nanowires [3], which it has been suggested arise from the tensile strain of MgS to the GaAs substrate [6]. We can monitor the phase stability and stoichiometry of the growing structure by RHEED which has proved invaluable in determining the onset of the phase change between ZB and rocksalt but gives limited information on the evolution of the surface morphology and development of the nanowires. However AFM provides the ability to measure the dimensions, distribution, and frequency of the wires allowing for detailed analysis. Alongside the use of AFM, RHEED was used in this study to investigate the Mg atoms when deposited, to provide a comprehensive model of the growth of ZB MgS.

Although MgS is a well studied material little is known as to the actual orientations of atoms on the surface when grown using either our growth technique or conventional MBE. Therefore two areas of interest will be the main topics in this chapter. First section 4.3 will show a surface study of the interaction of Mg atoms arriving at the MgS surface, investigated using RHEED to generate information on such surface parameters as step size, terrace width and periodicity. Captured video clips of the RHEED changes allow an understanding of the surface reconstruction (as discussed in chapter 2). Section 4.4 will demonstrate post growth analysis of the MgS surface using AFM to investigate how the formation of 1D wires changes under differing conditions. As MgS is predominantly used as a barrier material for carrier confinement a sharp interface between layers is advantageous. It is known that there is little or no intermixing between adjacent layers of ZnSe-MgS [7] due to the immiscibility of the materials. However the presence of 1D wires in the MgS layer can lead to fluctuations in width which in turn broadens the PL peak from a ZnSe QW when the well width becomes very thin.

4.2 Sample preparation.

For this study, all samples were grown in either the HWA or HWC chambers using 6N sources of Zn, Se and Mg and ZnS. GaAs (001) substrates were etched in a 2:2:15 H_2O_2:H_2O:H_2SO_4 solution prior to entry into the growth chamber. Any H_2O left on the sample was removed in the preparation chamber by heating to 200^0C. The oxide layer was removed by rapid heating to ~ 580°C before cooling back down to the growth temperature of 260°C under a Zn flux [8]. After oxide removal a sharp (4x2) pattern was observed on the [110] GaAs surface, indicative of a surface with minimal sulphur contamination. This surface is routinely obtained, before any use of ZnS in our system only when the liquid nitrogen cooled shutter is used to help reduce the low partial pressure of sulphur [2]. Contamination of the substrate by sulphur during oxide removal was further avoided by reducing the ZnS source temperature by 80K during the cleanup. For all samples, prior to the growth of the MgS layer, a 300Å buffer layer of ZnSe was deposited to protect the substrate from sulphur contamination. This preparation process was constant throughout all samples.

4.3 RHEED observations during MgS deposition.

RHEED patterns were obtained using a Staib 15S electron gun operated at 15keV. Patterns were recorded with a CCD camera, digitized and analyzed using Image Pro Plus (IPP) software to obtain profiles of the RHEED diffraction features, which were then used to estimate the scale of surface roughness. A schematic of this setup can be seen in figure 4.1.

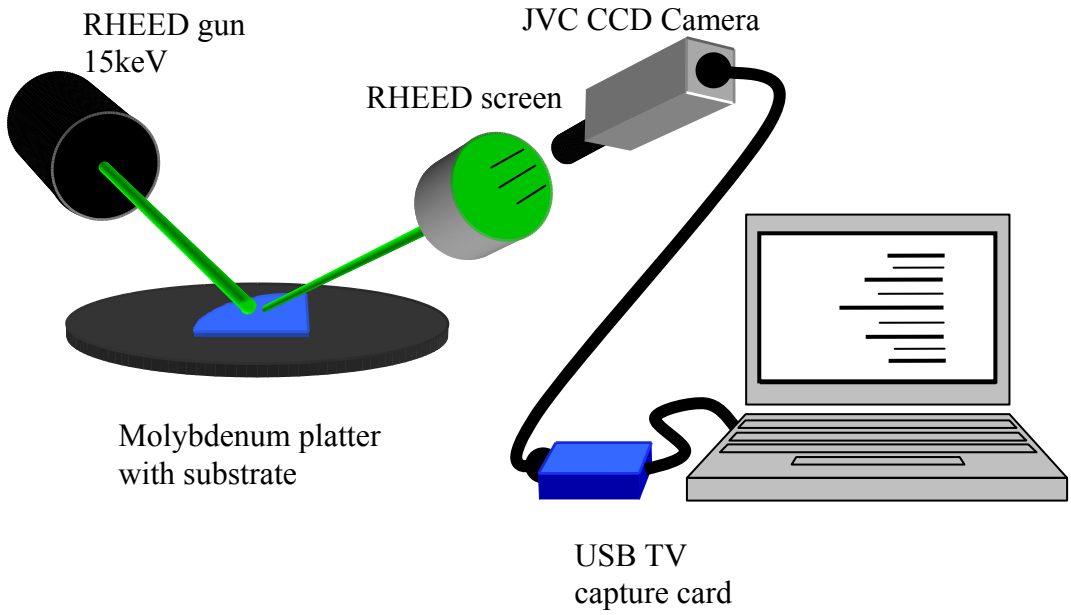

Figure 4. 1 *Schematic showing how the RHEED patterns were captured using a USB video capture card and recorded onto a PC.*

An analogue to digital video converter was needed to allow the PC to receive the signal from the CCD camera. A basic USB TV card was used as it provided the necessary ports and interface allowing the recording of the RHEED pattern. When a growth was complete the recording was stopped, saved and filed for analysis. The analysis of these samples is discussed in section 4.3.2 of this chapter.

In order to study the effect of different Mg fluxes and annealing conditions on the MgS surface, a series of identical MgS layers wasgrown. Growth always commenced with a thin (300Å) buffer layer of ZnSe, followed by the deposition of a MgS layer 70Å thick. The ZnSe buffer layer showed a sharp 2x1 pattern RHEED indicative of a flat surface at

the end of the growth of this layer. During the growth of the MgS layer a c(2x2) pattern was observed, shown in figure 4.2. In these experiments, the growth of the MgS layer was halted after the growth of 70Å, as previous AFM results have shown that this surface is flat while thicker layers can develop pronounced 1D wires [3,4], which introduce extra features in the RHEED (described in chapter 2).

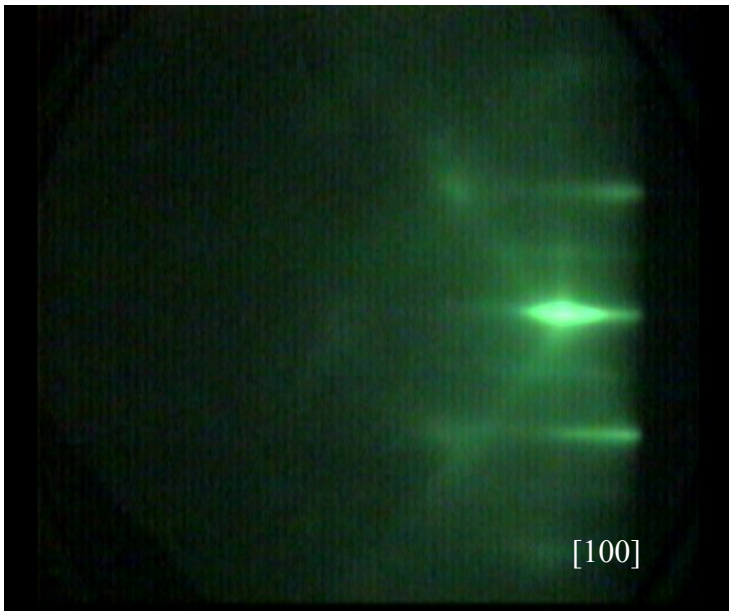

Figure 4. 2 *Still frame from recorded data. Frame shows a c(2x2) pattern commonly observed along the [100] direction during MgS growth. Also visible are faint Kikuchi lines.*

This growth procedure was used to generate all the layers which were used in subsequent experiments. In order to determine the stability of the MgS layers before exposure to a Mg flux, samples were annealed *in vacuo* at different temperatures. Up to 310 °C, no change was observed in the RHEED pattern, which remained c(2x2) over periods of many minutes.

MgS surfaces were then prepared as described above and the sample temperature was allowed to stabilize for 5-10 minutes at a temperature between 160 and 340°C. The Mg shutter was then opened and the changes in the RHEED pattern recorded (figure 4.3). Subsequently, the Mg shutter was closed and the recovery of the surface was monitored. During the exposure, the Mg cell flux was the same as that used during MgS growth. Based on the MgS growth rate of, 0.5Å/s, and the work covered in chapter 5 section 5.6.2, we estimate a Mg flux of approximately 2.7×10^{14} atoms s^{-1}.

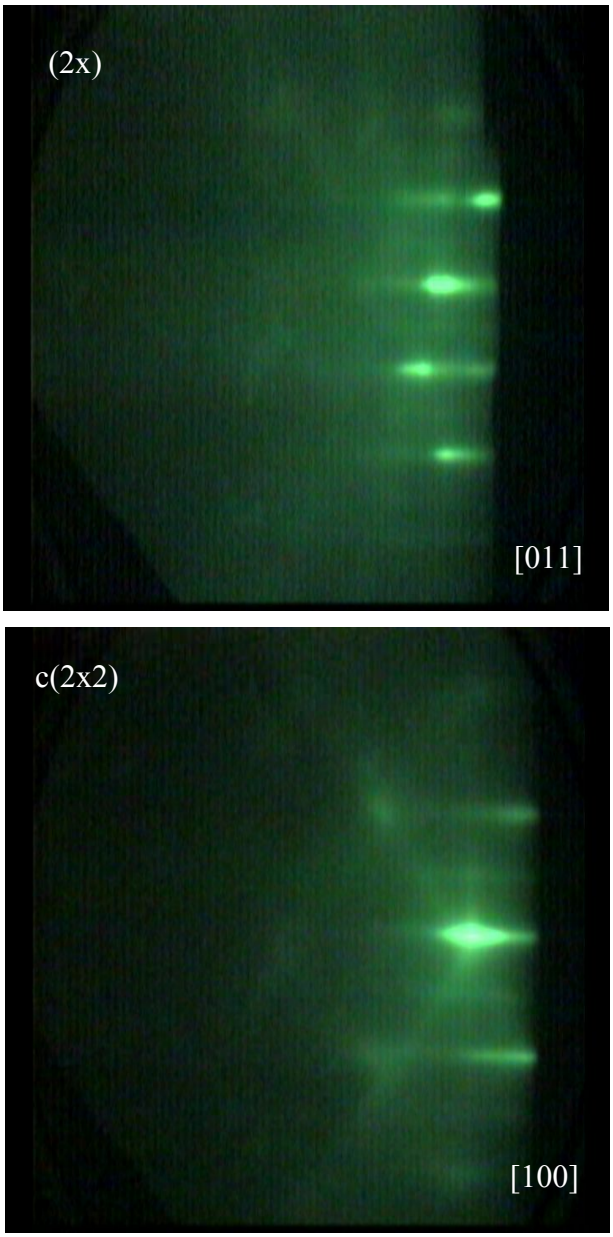

Figure 4. 3 *RHEED patterns observed during (top) ZnSe buffer showing 2x along [011] direction and (bottom) MgS layer showing c(2x2) which remained after annealing.*

In all cases, the c(2x2) pattern was lost during Mg exposure and never reappeared, even after long annealing times following termination of the Mg flux. At temperatures below 310°C, the RHEED pattern changed to a 4x (figure 4.4). The 4x reconstruction which was clearly observed with the RHEED beam oriented in the [110] direction was initially weak, but increased in intensity over several seconds. After reaching their maximum

intensity, the 4x RHEED streaks became very diffuse, then disappeared, and the pattern became a very spotty 1x (figure 4.4).

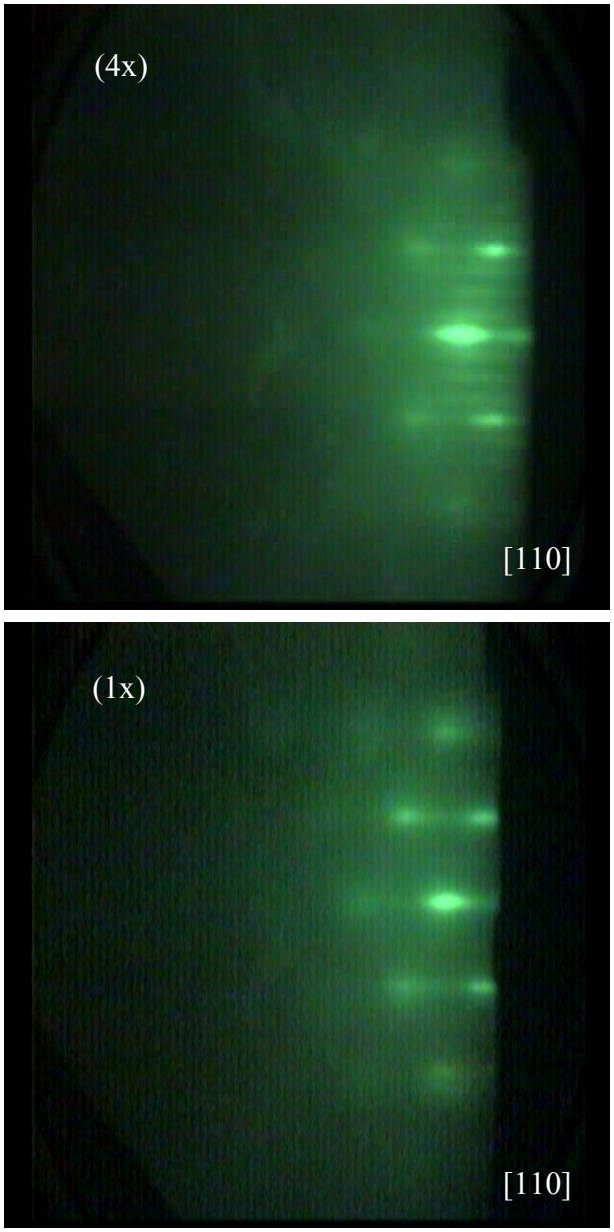

Figure 4. 4 *RHEED patters for (top) 4x1 reconstruction on MgS surface under Mg exposure with substrate temperature at T < 310^{0}C, (bottom) MgS surface under Mg exposure for extended time.*

With higher substrate temperatures, the time required to form the 4x reconstruction also increased, from 3s at 240°C to 10s at 300°C. Over the same temperature range, the time required for the c(2x2) pattern to disappear also increased with increasing substrate temperature. As these two RHEED patterns are observed along different azimuths, they

could not be monitored in the same experiment, but it appeared that the c(2x2) disappears at roughly the same time as the 4x reconstruction appears. At temperatures above 310°C, the 4x reconstruction was never observed, and the pattern evolved smoothly from a c(2x2) to a spotty 1x.

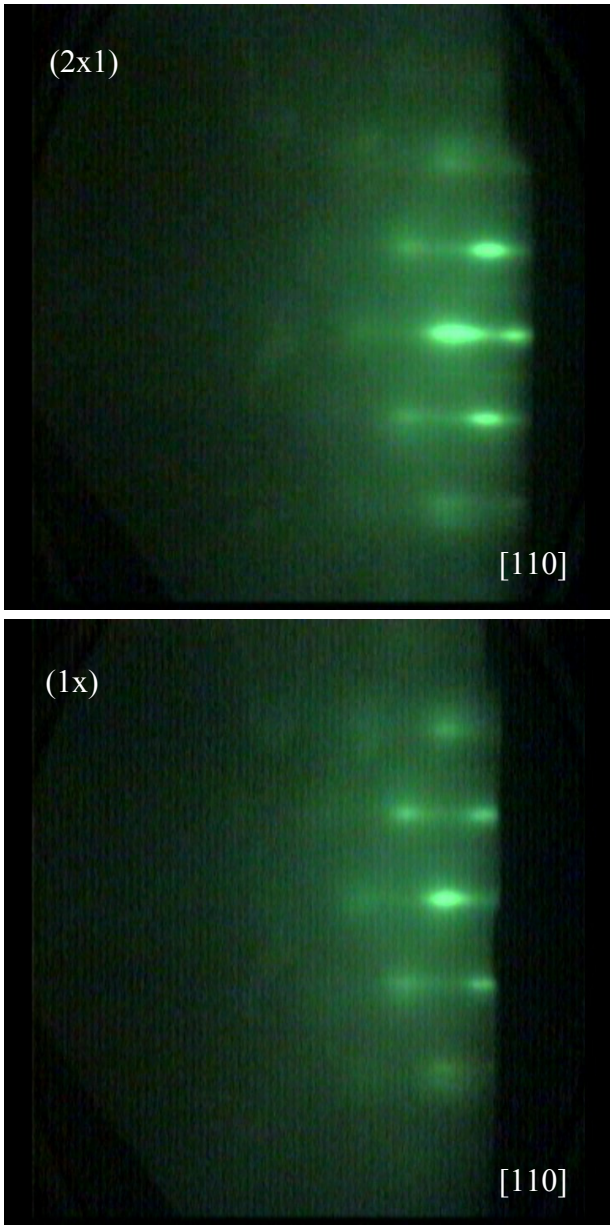

Figure 4. 5 *MgS RHEED patterns after sample has been annealed. The (2x1) pattern (top) is observed on surfaces that have previously had (4x) reconstruction. Surfaces that only demonstrated (1x) reconstruction were unaffected by annealing (bottom).*

These two surfaces showed different behaviour after the Mg flux was removed. Surfaces which showed the 1x1 pattern did not change, even after annealing for many minutes, while surfaces with the 4x1 reconstruction lost the ¼ and ¾ order streaks and changed to a 2x reconstruction (figure 4.5).

4.3.1 Analysis of observed RHEED patterns

As mentioned in 4.3 the RHEED patterns were recorded by a CCD and stored as MPEG data on the computer. An attempt was made to import this MPEG file into the Image Pro Plus (IPP) software but this was designed for use with a dedicated capture card that was not compatible with our updated computers. Due to this the codec used was specific to the software. Attempts to convert the MPEG to AVI were unsuccessful and prevented using the real time analysis function of that program. However this did not prevent analysis of stills from key points in the growth. By using some video editing software specific frames from the MPEG could be captured and exported as bitmaps to be used in the IPP. The ability to import real time video data for analysis is discussed in section 4.6.1 of this chapter.

4.3.2 Analysis of surface morphology from RHEED patterns.

A full treatment of the theory behind RHEED can be found in chapter 2 section 2.2.7. This section will provide a brief overview of the method used to analyze the recorded RHEED patterns.

As mentioned in chapter 2 the RHEED pattern displayed on the screen is a 2D reciprocal lattice of the real space lattice with the shape of the streaks depending on the type of disorder occurring on the surface. If the disorder on the surface is more pronounced along one specific direction the rods intersecting with the Ewald sphere are formed by solid ellipsoidal cylinders. This is shown in figure 4.6. In this instance one direction has a highly ordered surface with the perpendicular direction having little order.

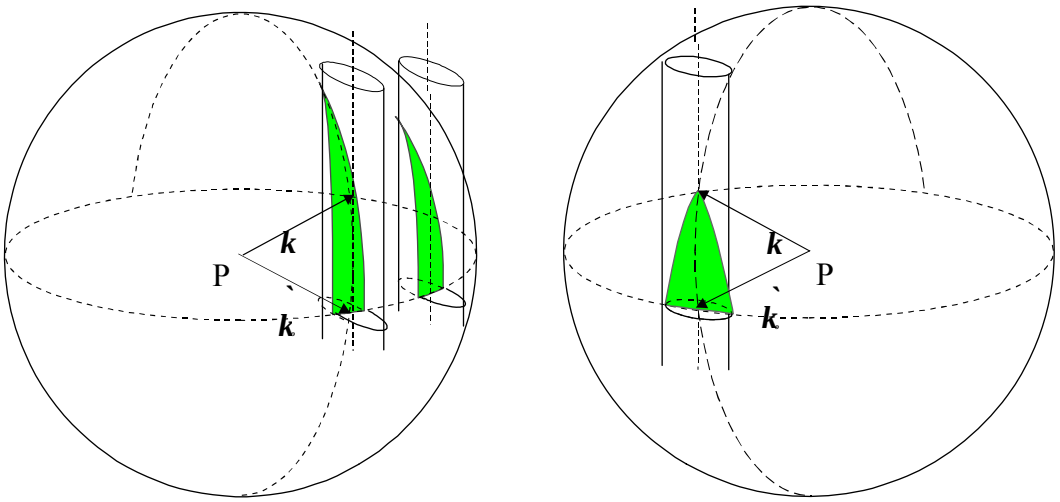

Figure 4. 6 *Schematic of disorder in one dimension.*

A surface which has disorder in one direction will produce long narrow streaks when the order direction is parallel to the intersection orientation with the Ewald Sphere. In contrast, if the ordered direction is perpendicular to the intersection direction, short, broad streaks are observed [9,10,11].

If it is assumed that the surface of the sample is stepped with constant terrace and step sizes, the reciprocal lattice of the stepped surface can be defined as the product of three structure factors: the Surface Mesh (bulk termination at surface), the structure factor of terraces, and the interference between terraces.

From these conditions the dimensions of the RHEED patterns can be directly related back to the dimensions of features on the surface. This is shown in figure 4.7.

The dimensions of the features in the RHEED patterns were measured using the IPP software. The software outputs any sizes in pixels, so a scaling factor was needed. Using a conversion from distance in pixels to reciprocal lattice length the dimensions noted in figure 4.7 could be found.

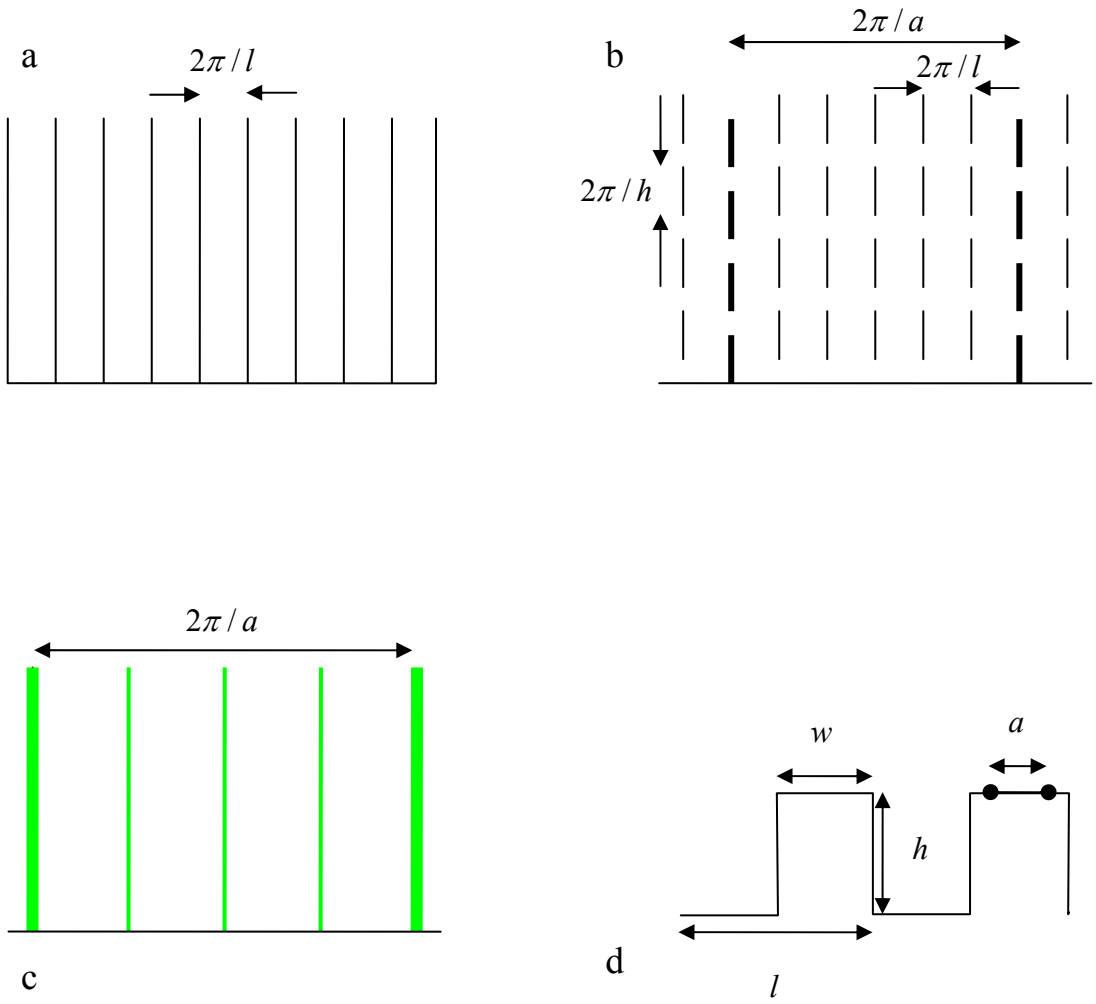

Figure 4. 7 *Schematic of RHEED patterns. (a) Reciprocal lattice of the surface unit cell, with periodicity l. (b) Reciprocal lattice of terraces of steps with unit vector, a. (c) Reciprocal representation of the product of the three structure factors, the thicker lines have higher intensity than other streaks observed. (d) Real space representation of b), a regular stepped surface with periodicity l, step height, h, and unit vector a.*

It can be seen in figure 4.8 how the measurements were noted on the captured RHEED image.

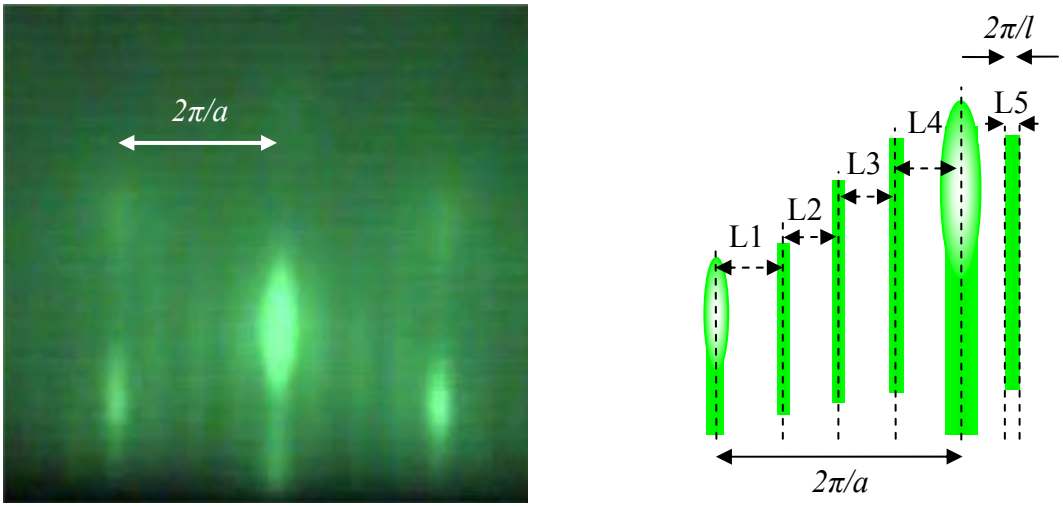

Figure 4.8 *RHEED pattern of 4x reconstruction with schematic of how the measurements were taken using the IPP software. Dimension 2π/a is = 0.25Å^{-1}.*

From the dimensions of the RHEED streaks, the surface roughness and domain sizes were estimated. For all the different surfaces, the RHEED patterns are compatible with domains which are on two levels, separated in height by 2-3Å, which is one atomic bilayer within the resolution of the experiment. The domain widths are less easy to determine as for the c(2x2), 4x1 and 2x1 patterns the CCD resolution means that the streaks are only a few pixels wide. As a result the terrace sizes must be in excess of 50Å. The 1x1 pattern is demonstrably different, and the broad spots are compatible with a much rougher surface where the domains are approximately 16Å wide.

4.3.3 Origins of RHEED features.

Currently there have been few studies as to the origins of RHEED features during MgS growth. However by looking at work on MgSe some comparisons can be made between the two material systems.

Wang *et al* [12] noted that the c(2x2) pattern is never observed during MgSe growth, but both (4x1) and (2x1) patterns routinely observed at low and high II-VI ratios respectively. They suggest that the c(2x2) pattern is confined to Zn containing compounds. In the growth of MgS only the c(2x2) pattern is observed during growth. However, in this work a ZnS compound source is used to supply sulfur and this does incorporate a small residual Zn mole fraction of the order of 1-2% [1, 2]. Previously it has been suggested that the growth of the zinc blende phase of MgS may occur through the presence of a Zn-rich alloy on the surface, with the Zn atoms continuously being replaced by Mg as the layer grows. This explanation is compatible with the suggestion of Wang *et al*. [7], Also the model initially predicted has been confirmed by the RHEED patterns observed from other groups that study MgS [13]. The patterns that are observed in our growth system are not seen when compound ZnS is not used as the source of sulphur.

This indicates to us that the presence of the intermediate Zn layer was responsible for the c(2x2) pattern routinely observed during our MgS growth. This also provides us with an indication as to why the use of ZnS is so successful. When using elemental sulphur the fluxes required are such that a sulphur rich growth regime is unavoidable. However in our system the c(2x2) patterns observed show a metal rich growth regime.

The following model is consistent with the RHEED patterns observed during growth, annealing and the MgS irradiation experiments.

1. *MBE growth of MgS*. During growth, the MgS surface has a c(2x2) RHEED pattern due to the fact that the top monolayer is ZnMgS with a significant Zn mole fraction. MgS growth occurs as the Mg atoms supplied react with the surface Zn atoms and displace them according to the reaction: Mg(ads) + ZnS(c) => MgS(c) + Zn (g).

2. *MgS annealing (no applied flux)*. The ZnMgS surface monolayer is stable *in vacuo* to evaporation over the entire temperature range considered, which is considerably lower than the temperature required to evaporate ZnS from a thermal evaporation source (>750°C).

3. *Irradiation with Mg flux.* The applied Mg flux eventually replaces many of the Zn atoms, producing a (4x1) MgS surface. This surface is the most Mg-rich and

is similar to that seen during MgSe growth. Removing the Mg flux causes some of the surface Mg to evaporate, leading to a more S-rich 2x1 pattern, again similar to that observed in MgSe growth [7].

4. *MgS surface roughness and the 1x1 pattern*. Large surface mesh patterns can only be observed on surfaces which are flat enough to permit the formation of domains larger than several unit cells. On the roughest surface, it is noted that the terrace size is comparable with one unit cell of the 4x1 pattern, and it is impossible for these structures to be observed. A 1x1 pattern is the only one which can be seen on a surface this rough.

This model does not explain the origin of the roughness, which probably arises from the low vapor pressure of Mg compared to other group II metals. At the lower end of the temperature range used (~240°C), the vapour pressure of Mg is low enough that a sizeable population of Mg atoms forms on the surface. The ZnMgS surface layer reacts with this adsorbed Mg phase. This reaction is at first a simple exchange reaction, replacing Zn atoms by Mg and leaving the surface morphology unchanged. With the majority of the Zn atoms removed, the continued Mg flux may aid the transport of material over the surface and the formation of a lower energy rougher surface.

As the temperature is raised, the Mg surface population decreases, and the rate of formation of the 4x pattern also decreases. If the replacement of Zn by Mg were a thermally activated reaction between species at constant concentration, then the rate of formation of the 4x pattern would increase with temperature. However the surface population of Mg atoms decreases with increasing temperature, and at approximately 310°C, the surface lifetime of Mg atoms becomes small enough that the difference between adsorbate sites becomes significant. Mg atoms are presumably most effective at replacing Zn atoms around those sites where they have the longest residence times. This will be at surface step edges, and means that existing surface non-uniformities will be enhanced, leading to roughening.

4.4 Surface Topography study of MgS nanowires characterised using AFM.

The samples described in this section are prepared in the same manner to those in section 4.3. Zn, Mg and Se cell temperatures remained constant with only the ZnS changing for the second surface topography investigation. The structures differ slightly between the RHEED study and the AFM investigation. For the AFM measurements the thickness of the MgS layer was designed specifically to allow for nanowire formation. The 1D wires had already been observed in samples with thicknesses over ~250Å so the MgS layers were grown over the range 150-350Å in order to observe the onset of the wire formation.

4.4.1 Methodology.

Unlike the RHEED study the samples in this investigation required removal from the growth chamber for study under the AFM. However it is well documented that Mg compounds react with air forming MgO and this reaction can completely destroy the surface of the MgS. As this study is revolving around the surface topography of MgS, maintaining the surface integrity is imperative and was achieved by capping the MgS with a few monolayers of ZnSe which prevented oxidation while preserving any nano sized structures.

Surface topography was measured using a Digital Instruments Dimension 3100 AFM. 5μm and 20μm scans were taken within minutes after the samples were removed from the chamber to prevent surface oxidation. All scans were obtained with the scan direction perpendicular to the wires, allowing measurements of the width, height, and length of the features.

In this study two sets of samples were investigated. In the first set, the II:VI ratio was kept constant by maintaining the ZnS and Mg temperatures at 863 and 375°C respectively while the sample thickness was varied from 100 to 400Å. The second set measured the effect of changing the impinging ZnS flux on the dimensions and spacing of the wires. In this set, samples were grown with a MgS thickness of 200Å where

nanowire formation was known to occur. The ZnS cell temperature was varied while the Mg cell temperature remained at 375°C.

The Mg flux is not routinely measured during every growth as it causes degradation of the ion gauge, however a value was obtained during the second series and has been used to calculate the ZnS:Mg flux ratio, which in this series varies from 1 to 1.5.

4.4.2 AFM Results.

A schematic of the wire development under differing conditions is shown in figure 4.8. In Figure 4.9 the 5µm square scans for a subset of the range of conditions studied are displayed in a phase diagram plotting thickness against II-VI flux ratio. These particular samples are shown as they show the greatest variation of topographic features, but the trends described below are observed consistently in many other samples that for reasons of clarity are not displayed.

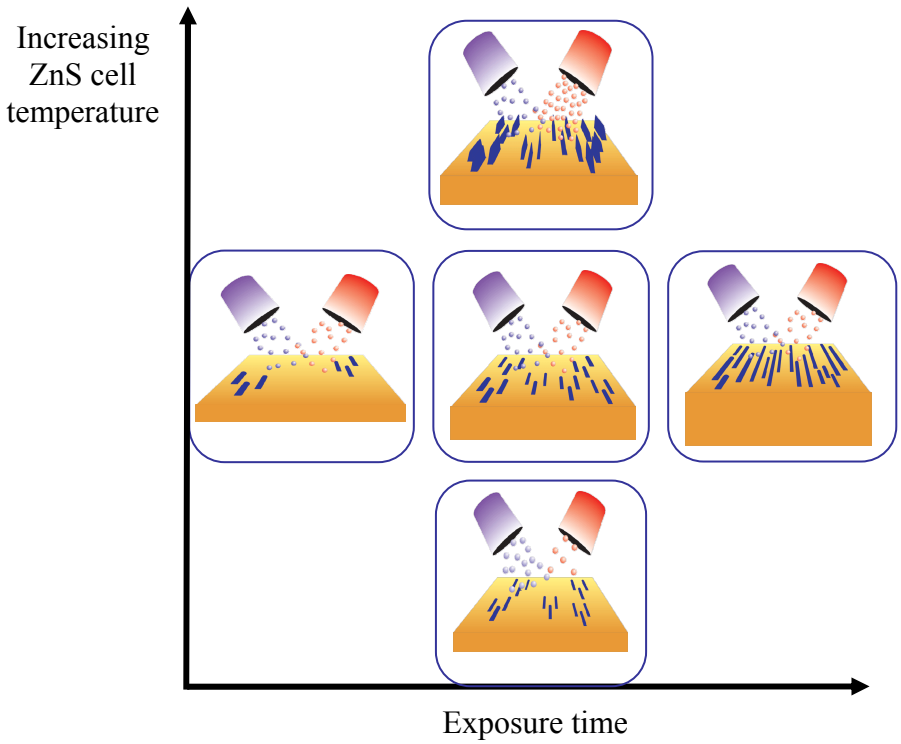

Figure 4. 8 *Schematic of phase diagram showing how the wires develop under differing exposure times ZnS cell temperature.*

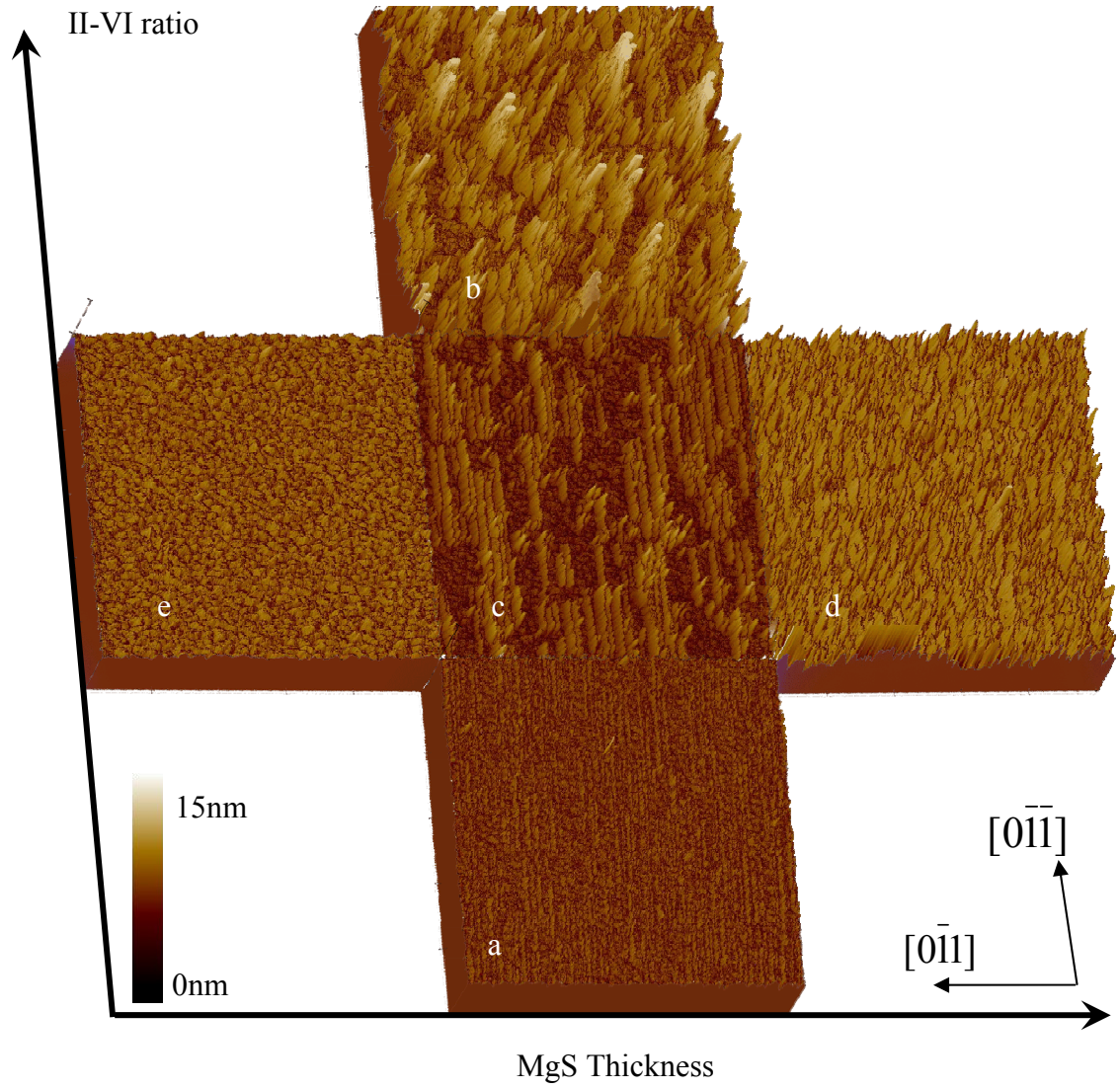

Figure 4. 9 *Phase diagram of MgS nanowires showing a) Thin layers show very few wires, b) At high flux wires have increased in height but the distribution remains constant, c) At 200Å thickness nanowires are 1µm long, 25Å high, with 1000Å spacing and are distributed in bunches along the <100> directions, d) Thicker samples show a dense coverage of surface with nanowires, e) At low flux the wires are smaller. Their distribution remains the same with increasing ZnS flux.*

The first set of results (horizontal axis) shows that at lower thicknesses ~ 100Å there are very few wires and the majority of the surface is atomically flat. Typical wire dimensions for a 100Å thick MgS layer are: length 3600Å, width 800Å and height 18Å.

As the layer thickness increases to 200Å the typical wire dimensions increase to 10000Å (length), 1000Å (width), and 25Å (height). Here the wires are clustered together in groups, but there are regions of the surface between the groups which remain totally wire-free. These flatter areas all have roughly the same width of approximately 0.6 µm.

As the thickness of the MgS layers increases to 400Å the distribution of the wires increases to cover the entire surface. In the sample shown the dimensions are 8150Å (length), 1270Å (width) and 720Å (height). Figure 4.10 shows a 1.5x1.5µm scan with fully developed 1D wires and how the dimensions were notated.

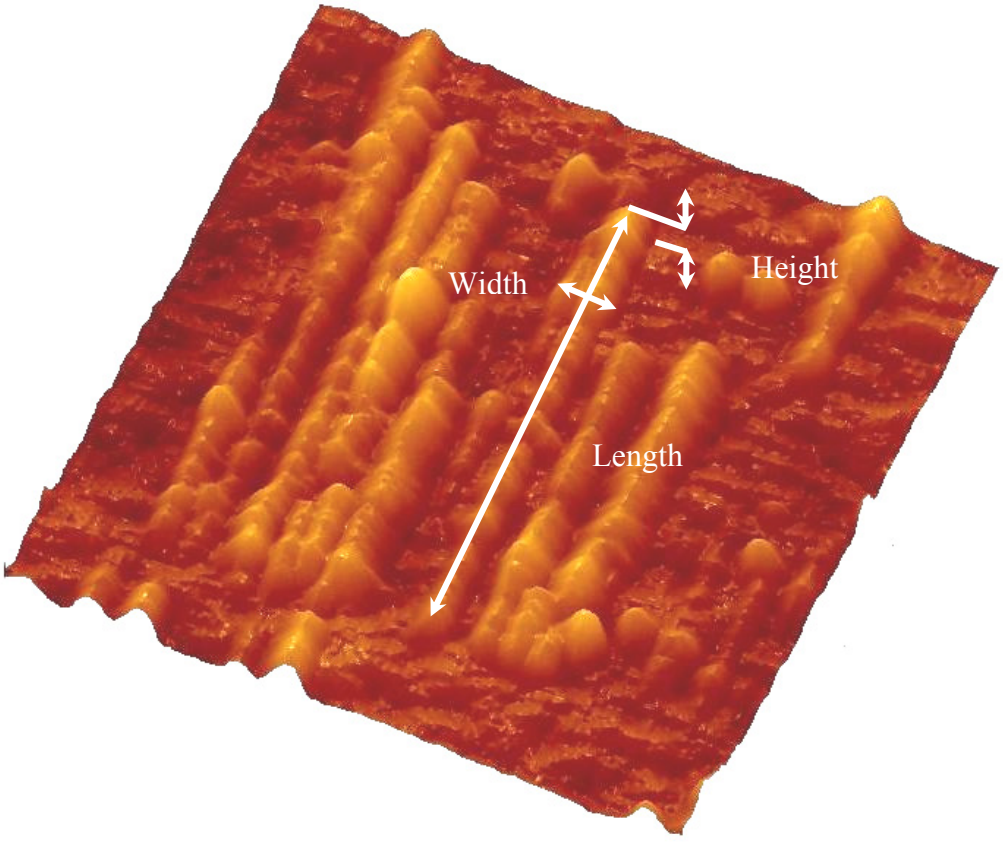

Figure 4. 10 *1.5x1.5µm scan showing fully developed 1D structures. Notation in white shows how the dimensions were measured*

In the second set of samples at low ZnS:Mg flux ratio of ~1:1 the wires are long, narrow and with similar height to the 100Å sample of the previous set. As the flux ratio is increased further, the wires broaden and increase in height, but still occur in patches which never cover the entire sample. This is shown in a line profile when comparing a sample grown with a high ZnS:Mg flux ratio with a thicker layer produced with a lower flux ratio (figure 4.11). Although the wires are comparable in size, it is clear that the thicker sample has an increased number of wires.

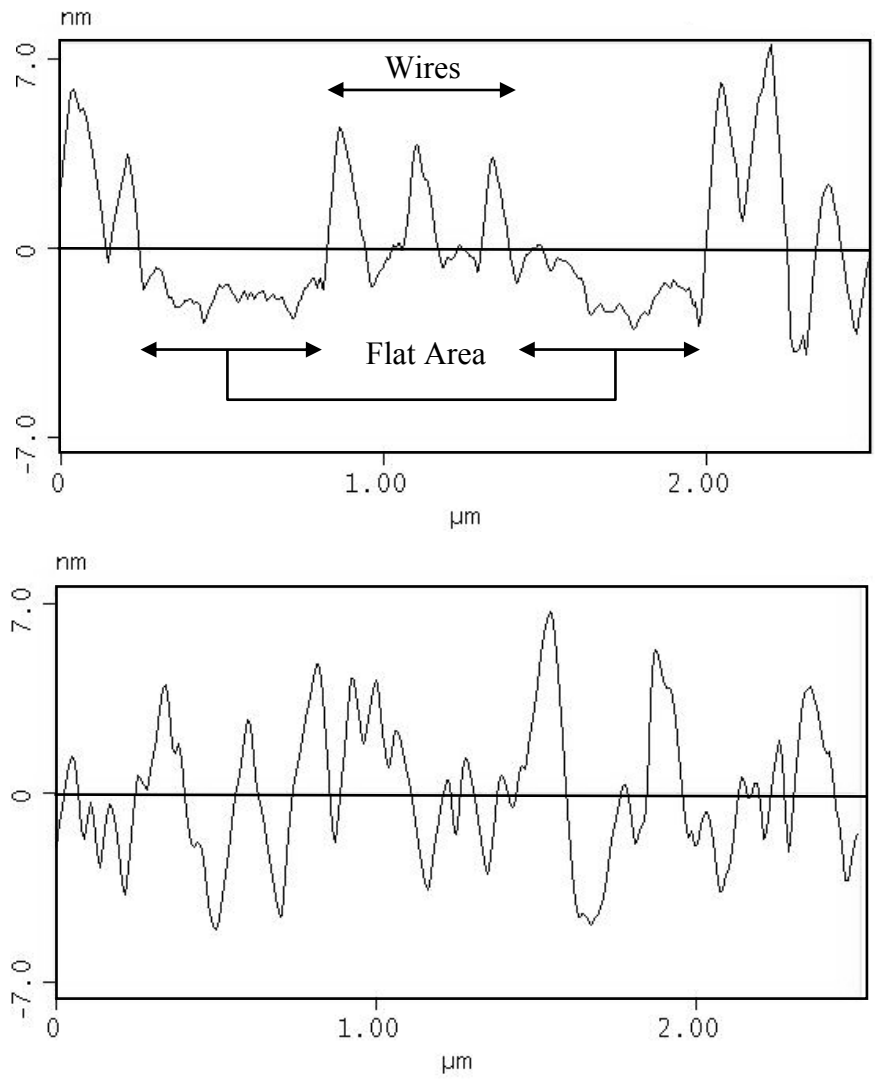

Figure 4. 11 *Cross section of MgS wires showing: Top, this sample with high ZnS flux; Bottom, Thick layer with low ZnS flux.*

For all samples in the second set the RMS roughness has been measured in the flat areas between the wires and has values of ~ 4Å indicating that it is atomically flat.

20µm scans were used to determine the distribution of the bunches of wires, and their orientation and propagation directions. By ignoring any information below a threshold height on the AFM scan the uppermost peaks of the wires were isolated from the underlying background. This was achieved by only displaying the top peaks of the wires. The image was then converted to greyscale and inverted to display the wires in black. In figure 4.12 it can be seen that the wires within one bunch are not aligned side by side, but are offset, such that the bunches have preferred directions which are roughly <100>.

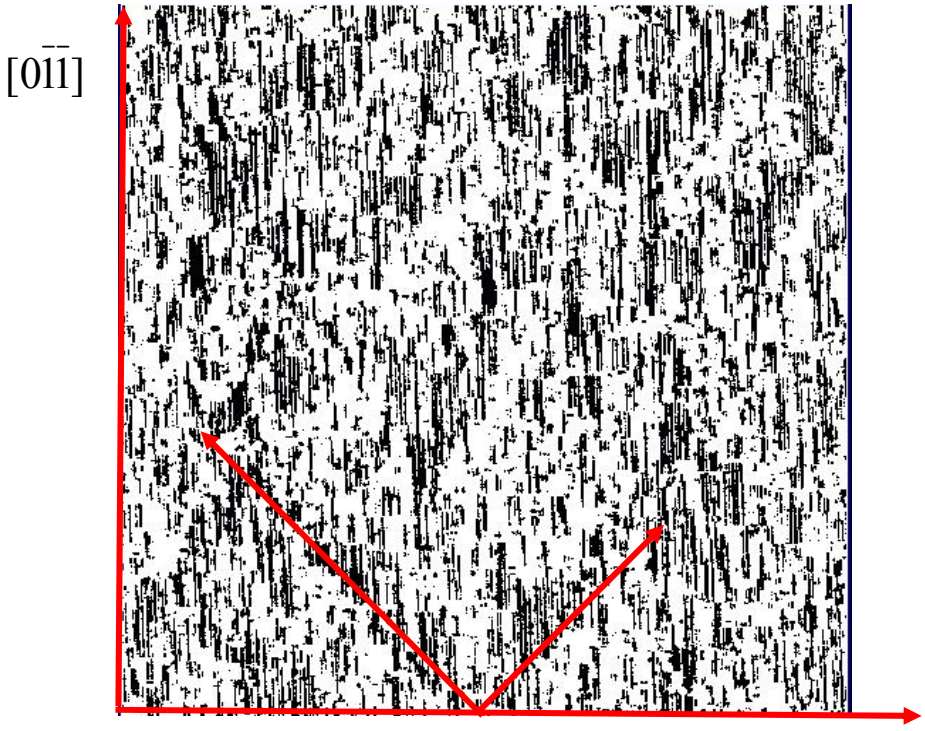

Figure 4. 12 *Inverted, greyscaled and intensity clipped AFM image used to highlight the bunching of wires along the <100> directions*

This distribution has been seen before in ZnSe when observed under a UV microscope (figure 4.13), it is also similar to X-ray topography done on ZnSe [14]. This shows that dislocations at high densities will preferentially adopt approximately <100> orientations.

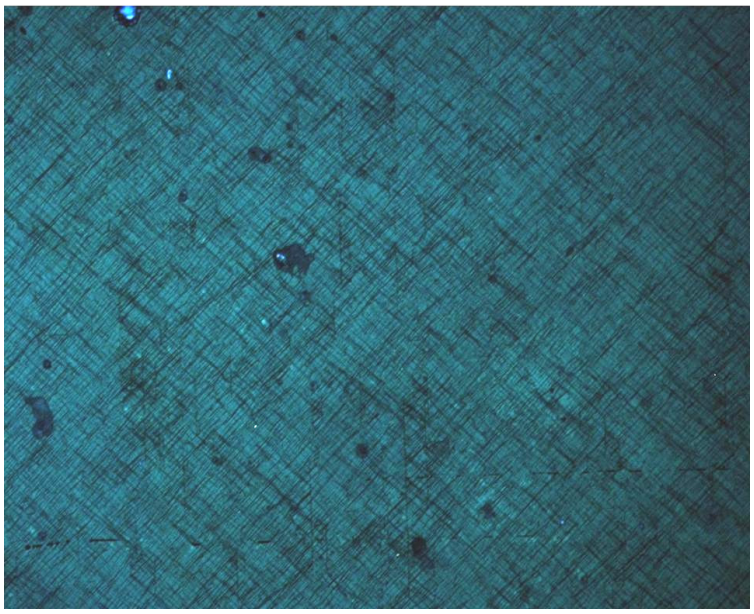

Figure 4. 13 *UV PL Microscope image of ZnSe. Dark regions indicative of dislocations. Similar cross hatching pattern as seen in figure 4.12*

Although these dislocation orientations have been seen in ZnSe it is not possible to confirm that the distribution is consistent with this orientation when MgS is deposited on top. It may be possible to investigate the distribution of the dislocations by X-ray topography.

4.4.3 Discussion.

The 1D wires described have been previously observed in many different strained epitaxial materials [15]. Two models have been developed to explain their formation, which differ fundamentally in the emphasis they give to kinetic and thermodynamic processes. Both models require anisotropic relaxation of the epitaxial layer with a network of mismatch dislocations oriented preferentially along just one of the two <110> orthogonal directions. Anisotropic strain is common in semiconductor structures where underlying dislocations modify the strain in a layer above. Under normal

conditions, dislocations have a preference to lie along certain orientations, generating strain relief. This causes a reduction in strain perpendicular to the line of the dislocation, and if the dislocation densities in orthogonal directions are different then this generates an anisotropic strain.

Mechanism 1 relies on the fact that mismatch dislocations are known to repel adsorbed atoms diffusing over the surface, thereby acting as templates for the confined nucleation of nanostructures from adatoms [16]. Here, the dislocation network increases the anisotropy of the diffusion coefficient for material transport on the surface, and generates a series of 1D features. In this system the wires would run in parallel to the dislocations.

An alternative, thermodynamic, explanation (mechanism 2) has been suggested to apply to the formation of wires in InGaAs [17]. In this alloy, and in the MgS layers shown here, the height of the wires increases with layer thickness, which is compatible with stress driven mass transport of material from the regions between the wires. The spontaneous generation of surface undulations with a preferred periodicity under stress is known as the Asaro-Tiller-Grinfield instability [18,19].

Recently this model has been developed further by Zhang [20] who has performed finite element calculations of the evolution of surface morphology and has modelled the formation of 1D features when the surface stress or strain is anisotropic. For certain anisotropy ratios these are similar to the ones which we see.

Zhang [16] has set a range of conditions to model the onset of 1D nanostructures. ε_x^0 and ε_y^0 are defined as the strains in two orthogonal directions. As the choice of x and y directions is arbitary, we chose $\left|\varepsilon_y^0\right| < \left|\varepsilon_x^0\right|$ and $-1 \le \varepsilon_y^0 / \varepsilon_x^0 < 1,\ \varepsilon_y^0 / \varepsilon_x^0 \neq 0$

Cases with negative strain ratios correspond to unphysical cases where one component is tensile and the other is compression.

The various conditions modelled by Zhang are shown in figure 4.14

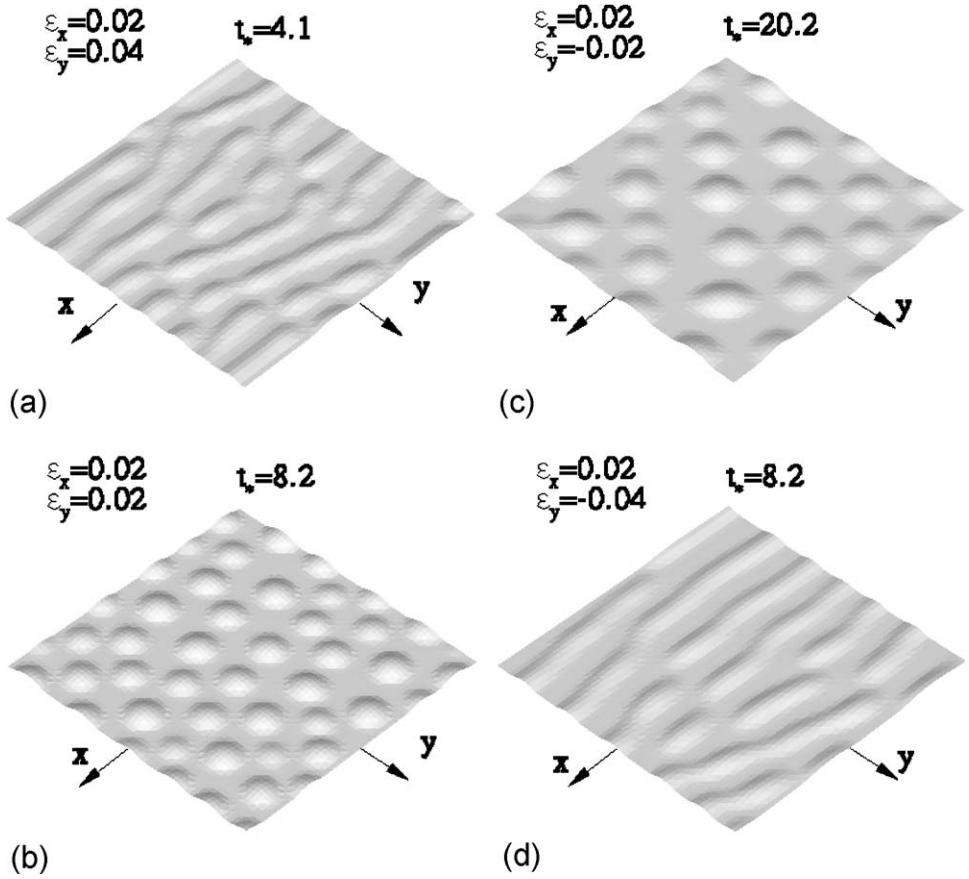

Figure 4. 14 *Surface morphologies for different values of* $\varepsilon_y^0 / \varepsilon_x^0$ *after certain time of surface evolution. (a)* $\varepsilon_y^0 / \varepsilon_x^0$ *=2, (b)* $\varepsilon_y^0 / \varepsilon_x^0$ *=1, (c)* $\varepsilon_y^0 / \varepsilon_x^0$ *=-1, (d)* $\varepsilon_y^0 / \varepsilon_x^0$ *=-2 [13]*

It can be seen in figure 4.14 that section (a) is the most like the AFM results that have been shown in this section.

X-ray diffraction shows that very thick (1300Å) MgS layers are relaxed, although it is not possible to determine the presence of any anisotropy in this material. If the initial relaxation of thinner layers, such as the ones investigated here, is anisotropic, then both of the above mechanisms (1 and 2) predict that 1D wires form on the surface. However for a given ridge direction, the models predict that the relaxation is in orthogonal directions, making it possible to distinguish between them using a technique such as reciprocal space mapping [21].

At present it can not be determined which mechanism is correct, although the Asaro-Tiller-Grinfield model appears to fit our observations better. Thus, in thin samples with

low dislocation densities, we expect to see relaxation around the dislocations leading to bunches of nanowires, while between the dislocations the surface remains smooth. As the thickness of the strained MgS layer increases, the dislocation density will increase and the flat areas eventually disappear.

Changing the ZnS:Mg flux ratio changes the ridge size but does not change the underlying dislocation distribution, and hence the wavelength of the wires is constant and the flat areas between the wires do not change in size. Again, the constant ridge wavelength is compatible with the Asaro-Tiller-Grinfield model, in which the most favourable wavelength is dependent only on bulk crystal parameters and does not depend on the surface stoichiometry.

The development of the wires does however require material to be transported across the surface, and the amplitude of the wires which develop during a given period of growth must increase in proportion to the diffusion coefficient. Larger wires on a surface exposed to a higher ZnS flux implies that the diffusion coefficient is higher on that surface. Measurement of the diffusion coefficients could be made to determine if this hypothesis is correct.

There then remains the question of the orientation of the bunches of nanowires, which we find are preferentially oriented along <100>. Although isolated dislocations in ZnSe lie along <110>, at higher concentrations the dislocations interact and adopt an overall <100> orientation to avoid one another [22]. Similar dislocation orientations have also been observed in ZnSe by X-ray topography [14] and by UV microscopy in both ZnSe epilayers and in ZnSe/ZnCdSe quantum wells [23]. It is likely, therefore, that the prevailing <100> orientation reflects the underlying average dislocation direction.

4.5 Conclusions.

The RHEED patterns from MgS surfaces have been observed during growth, annealing and both during and after irradiation with an Mg flux. A c(2x2) pattern was observed during growth which was stable during annealing, but was removed by a flux of Mg atoms. High temperature Mg irradiation creates a rough 1x1 surface. At lower temperatures the surface remains flat and a 4x1 reconstruction is observed with Mg irradiation changing to a 2x1 on annealing *in vacuo*. These results are compatible with the c(2x2) surface being a ZnMgS alloy which converts to a pure MgS 4x1 on Zn irradiation. The conversion from 4x1 to 2x1 results from the evaporation of excess Mg.

This set of investigations into the surface morphology during growth of MgS has yielded results that better improve our understanding of the MgS system. The model first predicted for the growth mode has been confirmed by the RHEED patterns observed. As the patterns observed in our growth system are not seen when a flux of S_2 is used this suggests that the presence of the intermediate Zn layer was responsible for the c(2x2) pattern routinely observed during our MgS growth. This agreed with our model suggesting that Mg replaces Zn at the surface allowing growth of the ZB MgS.

During the topography study we have investigated the formation of 1D nanowires in MgS epitaxial layers. The wires increase in size with increasing ZnS:Mg flux ratio or with increasing layer thickness. At low layer thicknesses we see that the distribution of wires is not uniform which we believe reflects the underlying dislocation density. At larger thicknesses the distribution becomes more uniform. We are not able to determine absolutely the mechanism of formation of the wires, but it is consistent with the Asaro-Tiller-Grinfield instability.

4.6 Future Work.

4.6.1 RHEED.

As mentioned during the treatment of the RHEED study one of the downfalls was the inability to record changes in the RHEED pattern in real time. Although our study generated important information on the growth of MgS, the experimental setup was a proof of concept so that other materials could be studied as well. Having to go through the process described in this chapter is not only time consuming but does not allow for on the fly corrections or real time quality control to be achieved.

To overcome this issue, an investigation into the best way to record and analyse the RHEED was undertaken. Having contacted the IPP suppliers to ask for advice it became clear that this software was no longer fit for purpose and the installation of upgraded software was not only expensive but unnecessarily overcomplicated. A decision was made to move to LabView as this is an open ended development tool with a wide range of functions and inputs. However this is not a graphic tool so the functions needed to measure the RHEED dimensions needed to be programmed in. This task was passed to an MSc student to investigate and their project was promising and showed that LabView was more than capable of doing this task.

Moving to LabView also allows for any input device to be used, eliminating any driver or capture card issues. Having spoken to other MBE groups with similar setups a decision has been made to move to a USB webcam rather than expensive CCD camera as the resolution of the webcam is far in excess of our requirements and is far cheaper than a designated CCD. This is currently under development and plans are in place to incorporate this new RHEED measurement system in the new MBE laboratory that is due to be completed in the 2nd quarter of 2009.

4.6.2 AFM.

Future developments in this study involve the confirmation of what model is the accurate representation of the development of the 1D wires. As mentioned in this

chapter, reciprocal space mapping will be the best indication as to which model fits our observations best. However there are still more characterisation techniques that should be investigated on this material to further increase our understanding. TEM is one technique to explore as it would provide a side profile through the wire and would allow the tracing back of any wires to the dislocations below. As in QD, it would also show how the crystal as been modified from the original ZB structure.

Further structural information could be obtained from more detailed AFM scans. Using the "amplitude" function in the AFM rather than the height provides actual deflection measurements as the tip scans the surface. This reduces any smoothing inherent in AFM scans due to the tip dimensions. By measuring the amplitude the actual step size of the wire terraces can be measured, again improving our understanding of their development.

4.7 References.

[1] C. Bradford, C.B. O'Donnell, B. Urbaszek, A. Balocchi, C. Morhain, K.A. Prior and B.C. Cavenett, Appl. Phys. Lett, 76 (2000) 3929

[2] C. Bradford, C. B. O'Donnell, B. Urbaszek, K.A. Prior and B.C. Cavenett, Phys. Rev. B 64 (2001) 195309

[3] C. Bradford, T. C. M. Graham, K. A. Prior and B.C. Cavenett, Phys. Stat. Sol. (c) 1, 645, (2004)

[4] R.T. Moug, C. Bradford, K.A. Prior, J. Crystal Growth, 301-302, (2007) 289.

[5] C. Bradford, K. A. Prior, and B. C. Cavenett, Phys stat sol c, (2005) 1-4

[6] K.A. Prior, C. Bradforda, L. David, X. Tang, B.C. Cavenett, J. Crystal Growth, 275 (2005) 141–149

[7] C. O'Donnell, MBE Growth and Characterisation of ZnSe-based II-VI Semiconductors, (2000)

[8] L.H. Kuo, L. Salamanca-Riba, B.J. Wu, G.E. Höffer, J.M. DePuydt and H. Cheng, Appl. Phys. Lett, 67, 3298 (1995).

[9] W. Braun, Applied RHEED, Reflection High-Energy Electron Diffraction during Crystal Growth, Springer-Verlag, 1999, ISBN 3-540-65199-3

[10] P. J. Dobson, An Introduction to Reflection High-Energy Electron Diffraction, in Surface and Interface Characterisation by Electron Optical Methods, edited by A. Howie and U. Valdre, Plenum Press, 1988

[11] M. G. Lagally, D. E. Savage and M.C. Tringides, Diffraction from disordered surfaces, edited by P.K. Larson and P.J. Dobson, Plenum Press, 1988.

[12] H.-M. Wang, J.-H. Chang, T. Hanada, K. Arai, T. Yao, J. Crystal Growth, 208, 253 (2000)

[13] R. Arians, T. Kümmell, G. Bacher, A. Gust, C. Kruse, D. Hommel, Appl. Phys. Lett, 90, (2007) 101-114.

[14] G. Horsburgh, K. A. Prior, W. Meredith, I. Galbraith, B. C. Cavenett C. R. Whitehouse, G. Lacey, A. G. Cullis, P. J. Parbrooka) P. Mo¨ckb) K. Mizunoc). APL, 72, 24, (1998) 3248-3150

[15] H. Li, J. Wu, Z. Wang, T. Daniels-Race, Appl. Phys. Lett, 75, (1999) 8, 23

[16] H. Brune, M. Giovannini, K. Bromann, and K. Kern, Nature 394, (1998) 451

[17] P. Krapf, Y. Robach, M. Gendry, and L. Porte, J. Cryst. Growth, 181 (1997) 337

[18] R.J. Asaro and W.A. Tiller, Metall. Trans., 3 (1972) 1789

[19] M.A. Grinfeld, Sov. Phys. Dokl, 31 (1986) 831

[20] Y.W. Zhang, Appl. Phys. Lett, 87 (2005) 121916

[21] K.A. Prior, C. Bradford, L. David, X. Tang, and B.C. Cavenett, J. Cryst Growth, 275 (2005) 141

[22] L.H Kuo, L. Salamanca-Riba, J.M. DePuydt, H. Cheng and J. Qiu, Appl. Phys. Lett. 63, (1993) 3197

[23] K. Goss, L. David, K.A. Prior, unpublished.

Chapter 5

MgS-rich ZnMgSSe alloys: Growth, Characterization and epitaxial lift off.

5.1 Introduction.

This chapter describes the growth and characterization of MgS-rich ZnMgSSe alloys. By using PL, XRI, AFM, and TEM characterization techniques the composition is determined, and the structural and optical quality is discussed with a view to incorporating this alloy into new II-VI nanostructures.

The $Zn_xMg_{1-x}S_{1-y}Se_y$ alloy system is well studied as it permits lattice matching to both GaAs and GaP substrates with alloys over a wide range of bandgaps from 2.7 eV for ZnSe to ~5 eV for MgS. However, a limited range of compositions can be grown lattice matched to GaAs due to a region of phase immiscibility. This region is known in part experimentally and the entire composition range that is not permissible due to phase separation was defined by V.S. Sorokin, *et al.* [1]. In particular, they calculated the spinodal decomposition regime where alloys will spontaneously decompose. This is shown on the inner curve in figure 5.1. By considering the lattice match line for GaAs from ZnSe to MgS as shown in figure 5.1 (red line) there are only two regions where an alloy of $Zn_xMg_{1-x}S_{1-y}Se_y$ can be grown. Accordingly, most studies have occurred at the ZnSe-rich end of the phase diagram region (A) in alloys lattice matched to GaAs with both $x, y \geq 0.8$. However, the ZnMgSSe phase diagram contains another single-phase region (B) with low strain to GaAs substrates, with $x, y \leq 0.25$. In this chapter these will be referred to as MgS-rich alloys.

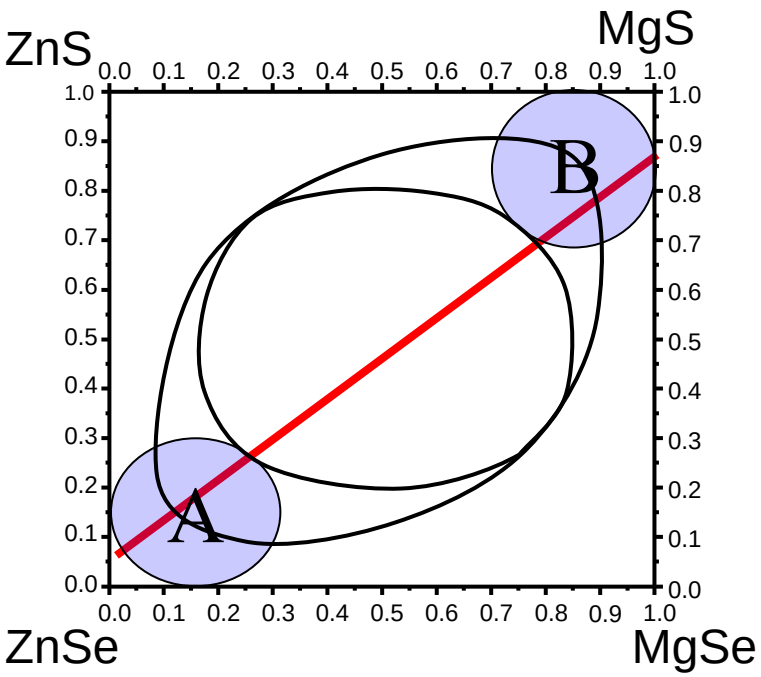

Figure 5. 1 *Phase diagram first demonstrated by Sorokin et al [1], defining the compositions that are a)thermodynamically stable (outside the outer curve) and b) will spontaneously decompose (inside the inner curve).*

The preponderance of studies in the first region (A) is due to ZnSe being a relatively easy material to grow with a fairly straight forward transition from binary, to quaternary. However, ZnMgSSe from region (A) has often been grown using a sulfur cracker, a technique that was abandoned at HW due to the high sulfur background pressure generated. The use of ZnS as a sulfur source is mentioned extensively in previous chapters and allows for the growth of metastable MgS. The group at HW has previously grown MgS in the metastable zinc blende crystal structure on GaAs substrates in layers up to 1400Å in thickness [2]. None of the properties of the MgS-rich ZnMgSSe alloys are well determined, as the stable crystal structure of MgS is rocksalt, and these alloys are all metastable Zinc Blende. However having characterized metastable MgS, region (B) can now be studied.

In this chapter it is demonstrated that the same growth conditions used for MgS can also be applied to MgS-rich quaternary alloys. Their use in lattice matched heterostructures as well as their structural and optical properties has been investigated. The growth of

MgS-rich alloys also confirms experimentally the position of the spinodal curve. Shown in figure 5.1. Furthermore, by examining the growth rate of ZnMgSSe the sticking coefficient of Mg in MgS can be estimated.

MgS-rich alloys have a number of potential advantages: they have much larger bandgaps than the ZnSe-rich alloys, while compared to MgS, they are less prone to oxidation and hydrolysis which should also provide a resistance to HCl etch used in epitaxial lift off.

The ability to separate an epitaxially deposited layer from the substrate on which it was grown and transfer it onto a different supporting material gives the potential for new device structures and is a necessary step for many applications. One simple method of accomplishing this is by means of an epitaxial lift-off technique, which was first demonstrated in GaAs/AlAs structures by Yablonovich *et al* [3]. For II-VI semiconductors a similar lift-off technology has not been available until recently. However, Mg chalcogenides are extremely soluble in dilute acids and our group have demonstrated that ZnSe/ZnCdSe quantum wells deposited on top of a MgS layer can be removed from the GaAs substrate without damage [4]. In these structures the MgS is used as a sacrificial layer due to its solubility in dilute HCl, with there being a difference in etch rates between MgS and ZnSe of approximately 10^8:1 [5]. Subsequently, the aim has been to develop a technology allowing II-VI multilayers containing either quantum wells (QW) or quantum dots (QD) to be removed from the substrate and transferred to materials of different functionality. This technique has been used to transfer ZnSe/ZnCdSe quantum wells onto Bragg dielectric mirror stacks, combining the benefits of commercially available dielectric mirrors with MBE grown active regions in hybrid devices which has enabled the observation of exciton-photon coupling in quantum wells [5, 6].

In addition to its use as a sacrificial layer in these devices, MgS has other useful applications, as it can be grown epitaxially on GaAs in conjunction with ZnSe based alloys. Also, having a bandgap of ~5eV, it forms an excellent barrier material for both ZnSe quantum wells [2, 7] and CdSe quantum wells and dots [8, 9]. Unfortunately, it is of course not possible to use MgS both as a large bandgap barrier and as a sacrificial layer for epitaxial lift-off in the same structure. Therefore MgS-rich, ZnMgSSe alloys

have been examined to determine suitable compositions which are acid resistant and provide the same confinement that MgS generates with the aim to incorporate both compounds into an epitaxial lift off structure.

5.2 Growth of MgS rich ZnMgSSe.

All samples were grown by molecular beam epitaxy in the growth chamber denoted HWC. The growth method used for the MgS-rich alloys was identical to that used for MgS (chapter 4) and the ZnMgSSe cap used in MgS containing nanostructures [7,8,9]. Elemental sources of Zn, Mg and Se 6N pure were used, and S was provided from a ZnS 6N pure compound source. No other source of S was used in the growth chamber. Cell temperatures used were: Zn 285°C, Se 177°C, Mg 375°C and ZnS 865°C. These cell temperatures were chosen as they generated the same fluxes as had been used in previous MgS and ZnSe studies. The cell temperatures remained constant, within experimental error, for every sample presented in this chapter.

At the start of growth, the GaAs substrate was heated to 580°C to desorb the surface oxide, and then cooled to 240°C under a Zn flux [10]. During growth, the substrate temperature was measured by a pyrometer and kept at 240°C for all layers. All samples commenced with a 500Å thick ZnSe buffer layer. The RHEED pattern became streaky before 20Å of ZnSe had been deposited and remained streaky throughout the growth of all layers. For all Mg containing layers a c(2x2) RHEED pattern was observed indicating a metal rich growth regime as demonstrated in chapter 4.

In the following sections the experiments will be split into two groups: Firstly in section 5.3, the structural properties of the material are investigated with the aim of obtaining alloy composition and growth rate. Subsequently in section 5.4, once a growth rate has been defined optical measurements of structures containing this alloy are discussed.

5.3 Structural investigation.

5.3.1 Initial determination of alloy composition and growth rate.

For this study two types of samples were grown as shown schematically in figure 5.2. First, a set of GaAs / ZnSe / ZnMgSSe / ZnSe samples were grown changing the ZnMgSSe growth time from 15s to 2 minutes. These were analyzed by X-ray Interference (XRI) [11,12]. The thicknesses of the layers in these samples were such that they could be compared directly with an almost identical set of ZnSe / MgS /ZnSe samples grown previously for analysis by XRI [7,13]. Subsequently, a sample was grown with a thicker ZnMgSSe layer with the structure GaAs / ZnSe / ZnMgSSe/ ZnSe which was used for AFM and HRTEM analysis.

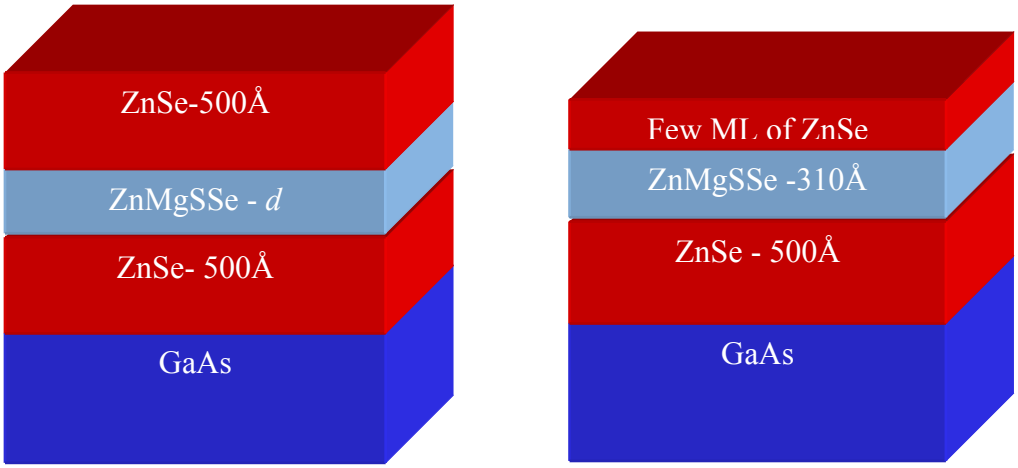

Figure 5. 2 *Schematic diagram of the two main sample types used in this study.*

In the structures above, the modulation in intensity observed in double crystal X-ray spectra arises from the two layers of ZnSe having a phase difference generated between them from the presence of the thin intermediate ZnMgSSe layer. This is discussed in more detail in chapter 2 section 2.2.4. 400 reflection double crystal X-ray spectra were obtained for all samples, and simulations were performed using the Bede RADS software. Figure 5.3 shows the initial XRI spectrum from samples with a ZnMgSSe layer *d* thick. In addition to the sensitivity of the central layer to layer thickness the

quality and number of the interference fringes observed in the XRI scan is important. High quality fringes can only be observed when the two 500Å thick ZnSe layers have nearly identical strains and parallel lattice planes, meaning the ZnMgSSe alloy has not relaxed or undergone any phase segregation into regions of different composition and strain. This point is returned to in section 5.3.2.

Reasonable fits were obtained for all structures, which could be improved in all cases with thin (10-40Å) interfacial layers of an intermediate alloy composition between the ZnSe layers and the quaternary. The table of results is shown below in table 5.1 with a composition for the quaternary alloy of $Zn_{0.2}Mg_{0.8}S_{0.64}Se_{0.36}$. This value obtained will be important in later sections of this chapter.

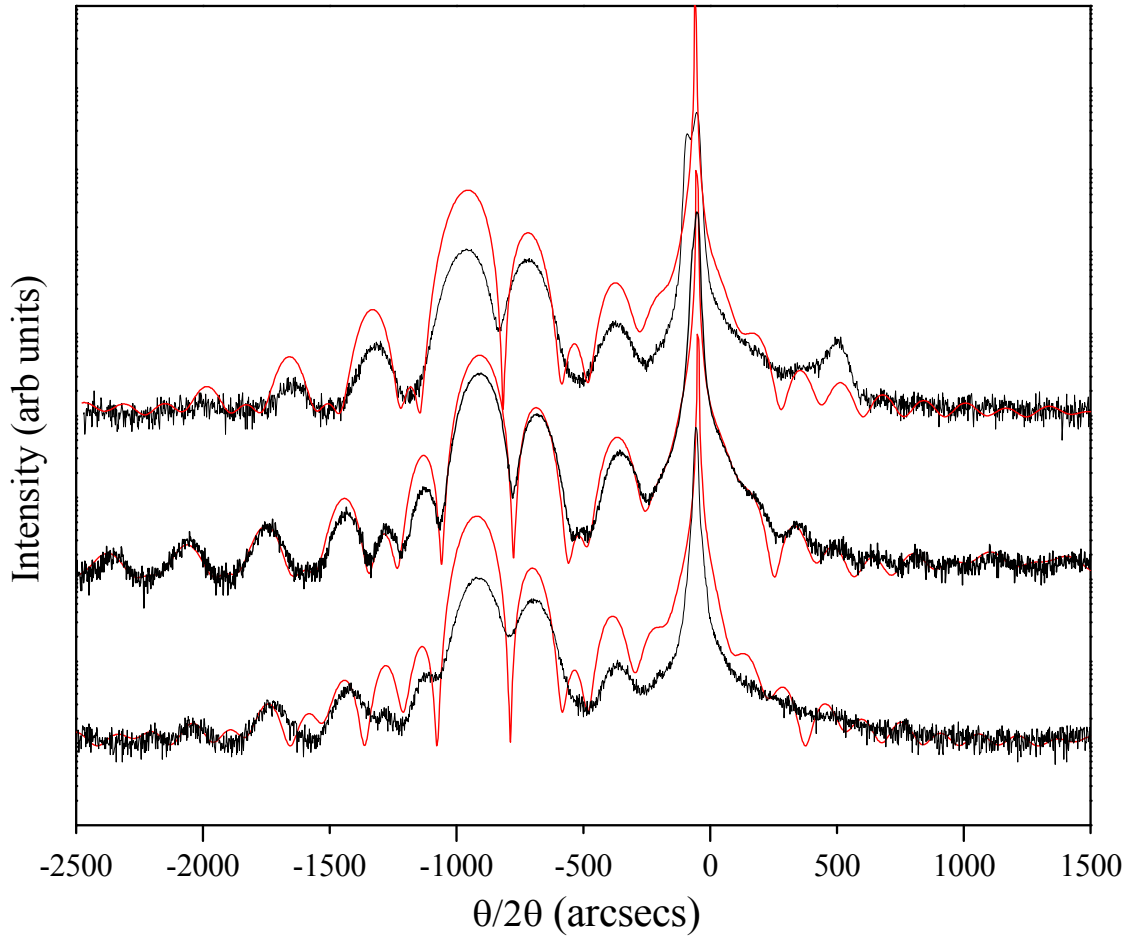

Figure 5. 3 *XRI scans of (in ascending order) HWC167, HWC178 and HWC180 with their respective simulations*

Sample Number HWC167			
Thickness (Å)	Material	Mg %	S %
490	ZnSe	0	0
43	$Zn_{1-x}Mg_xS_ySe_{1-y}$	0.12	0.10
169	$Zn_{1-x}Mg_xS_ySe_{1-y}$	0.80	0.66
10	$Zn_{1-x}Mg_xS_ySe_{1-y}$	0.30	0.20
535	ZnSe	0	0

Sample Number HWC178			
524	ZnSe	0	0
44	$Zn_{1-x}Mg_xS_ySe_{1-y}$	0.18	0.20
103	$Zn_{1-x}Mg_xS_ySe_{1-y}$	0.78	0.60
42	$Zn_{1-x}Mg_xS_ySe_{1-y}$	0.20	0.22
515	ZnSe	0	0

Sample Number HWC180			
550	ZnSe	0	0
13	$Zn_{1-x}Mg_xS_ySe_{1-y}$	0.29	0.15
59	$Zn_{1-x}Mg_xS_ySe_{1-y}$	0.78	0.63
10	$Zn_{1-x}Mg_xS_ySe_{1-y}$	0.23	0.13
535	ZnSe	0	0

Table 5. 1 *Best fits from the XRI simulations defining layer thickness and composition.*

Growth Time(s)	Sample no	Thickness (Å)	Zn comp %	Mg Comp %	S comp %	Se comp %
120	167	168	20	80	66	35
60	178	103	22	78	63	37
30	180	59	22	78	64	36

Table 5. 2 *Thickness values for growth time and their respective composition.*

By using the values determined by the XRI scans a growth rate of 1.2Å/s for ZnMgSSe was found. However when the thicknesses found using the above simulations were plotted against time (figure 5.4 red line), the intercept at $x = 0$ does not lie on the origin but rather at 26Å above. One concern is that the XRI technique is cyclic in thickness so there are multiple periodic solutions of specific repeat thickness available for a given XRI pattern. Using the ZnMgSSe strain and an estimate of the value of Poissions ratio, the phase shift in the diffracted amplitude of the 400 reflection can be determined as a function of layer thickness *d.* From this value, and the condition that the XRI pattern should repeat every 2π, the repeat thickness can be found. In the case of the quaternary alloy presented here the thickness is 220Å, far more than the discrepancy of 26Å highlighted in the data and therefore the thickness had not been overestimated by one whole period.

Error bars were added on the y axis to try and allow for the presence of the intermixed or graded layer in the thickness measurement. An error of 15Å was used, which was roughtly half of the thickness of the intermediate layers in the simulation and was a good first approximation. By introducing this small error in the thickness a gradient with the origin as it intercept was achievable. This generated a growth rate in the region of 1.48Å/s. (figure 5.4 blue line)

As mentioned, the highly resolvable Pendellösung fringes observed in all XRI scans are indicative of good quality material. To confirm this, a GaAs / ZnSe (500Å) / ZnMgSSe (310Å) / ZnSe (45Å) structure was grown and examined by TEM and AFM. These thicknesses were chosen to match a similar sample of MgS which was used as a comparison. The top ZnSe capping layer was used to inhibit oxidation of any Mg exposed to the air and did not interfere with the TEM and AFM measurements.

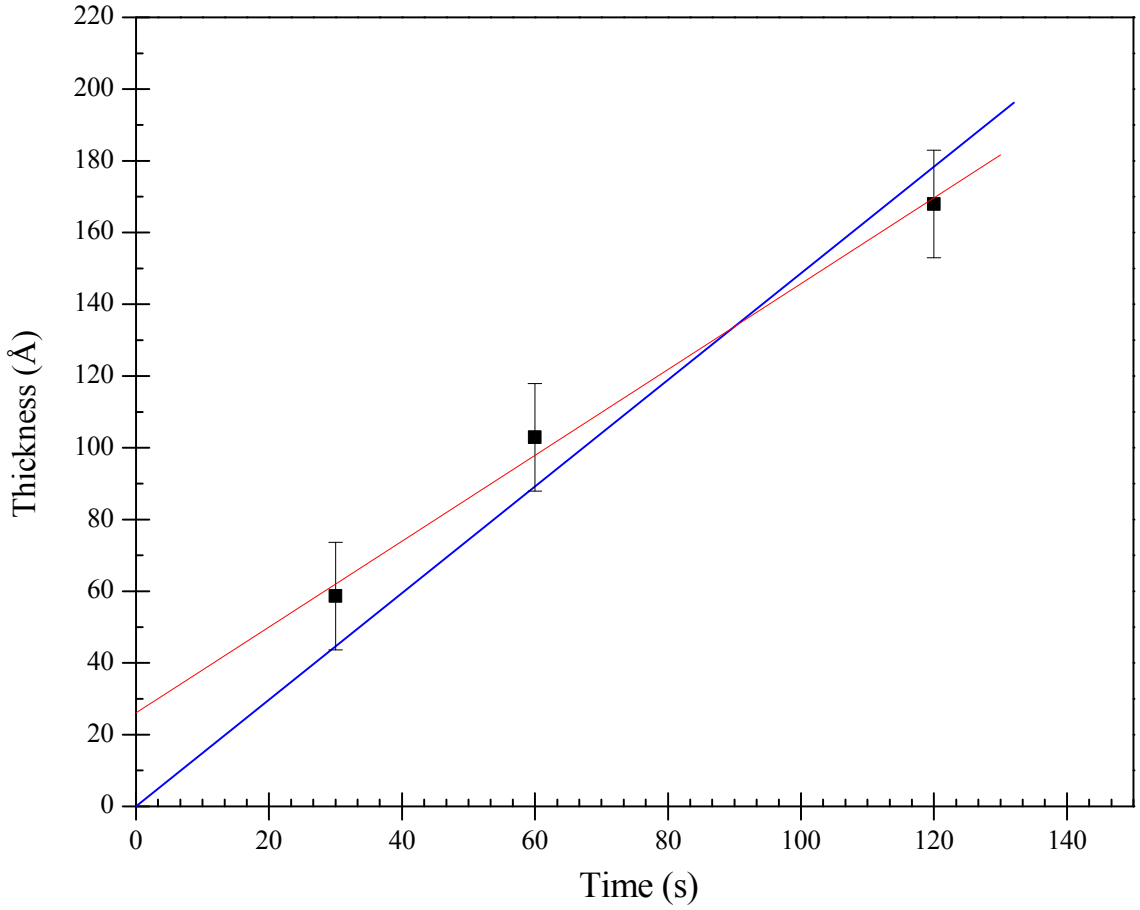

Figure 5. 4 *Graph of thickness of quaternary alloy layer vs time used to determine growth rate.*

5.3.2 HRTEM and AFM characterization.

The results can be summarized as follows: Electron diffraction patterns from the heterostructure showed only one resolvable set of diffraction spots, indicative of an epitaxial, pseudomorphic structure with no evidence of any second crystalline phase or phase decomposition. Figure 5.5 has a HR-XTEM micrograph of the ZnMgSSe/ZnSe boundary showing the atomic arrangement at this interface. There is complete continuity of the crystallographic planes of both structures and hence no evidence of misfit dislocations. In comparison, below, is a cross sectional view of the same structure showing the boundary between the MgS and ZnSe layers.

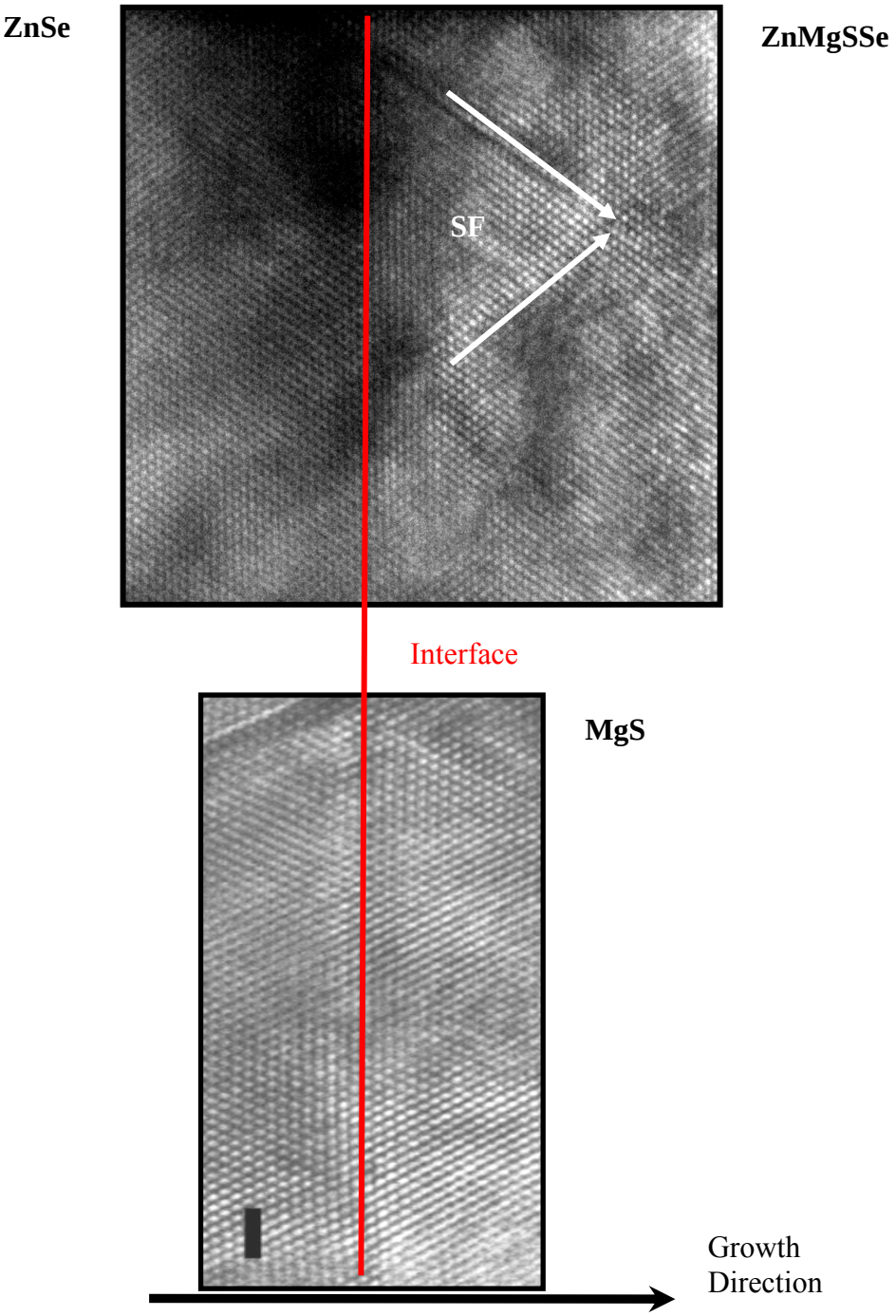

Figure 5. 5 *HRTEM micrographs of the GaAs / ZnSe (500Å) / ZnMgSSe (310Å) / ZnSe (45Å) sample showing the ZnSe/ $Zn_{0.2}Mg_{0.8}S_{0.64}Se_{0.36}$ (a) and the / ZnSe/MgS (b) interfaces where abrupt boundaries between layers with similar lattice parameter are visible.*

There is not a great deal of contrast between the $Zn_{0.2}Mg_{0.8}S_{0.64}Se_{0.36}$ and the ZnSe at these high magnifications used, but a boundary can still be determined. In general, the

boundary is sharp and flat, indicating a good quality interface with no significant intermixing, but in the example shown a triangular shape structural defect formed by two {111} approaching stacking faults (SF) which have propagated from the GaAs/ZnSe interface is visible in the bottom half of the figure. However, these defects are only occasionally observed and they are not intrinsic faults of the ZnMgSSe layer.

On investigation of the surface topography of the ZnMgSSe layer by AFM it was seen that for almost identical thickness the surface roughness was less that that of MgS. This is shown in figure 5.6. With an RMS roughness value of 5Å for the quaternary alloy and 6Å for the MgS it was clear that the material was growing with atomically flat layers. As mentioned in chapter 4 the strain anisotropy in the MgS system results in the surface buckling, resulting in the surface wires. It is possible that the introduction of more zinc in the quaternary alloy may harden the lattice, reducing dislocation motion and creating less strain anisotropy and thus an increase in thickness before observing surface features. This cannot be tested within our group as it requires reciprocal space mapping and TEM measurements to gain a better understanding of the strain anisotropy present. At this time why it is a better surface is not the main concern but more how this may be used.

The AFM data agrees with the TEM and XRI measurements as very flat surfaces will generate sharp interfaces between layers and thus well resolved fringes. One important point here is that in order to improve the XRI simulations, a 5 layer model was used with thick intermixed layers, however it is clear from the data presented that there is very little intermixing and that the interfaces are sharp. Intermixed layers have been used previously to generate better fitting simulations however in these cases the layers were only 1-2 monolayers thick, far less than used in the simulations presented here [14]. With the new data from the AFM and TEM measurements the XRI simulations had to be reviewed to remove the 10-40Å intermixed layers from the model. This was an opportunity to answer some other questions which arose from the simulations, including, is there a unique solution to the data? As this material is a quaternary alloy rather than a binary there are a range of compositions lying along a lattice match line that should produce the same XRI pattern. The next section will attempt to determine accurately the growth rate and composition by re-examining the data.

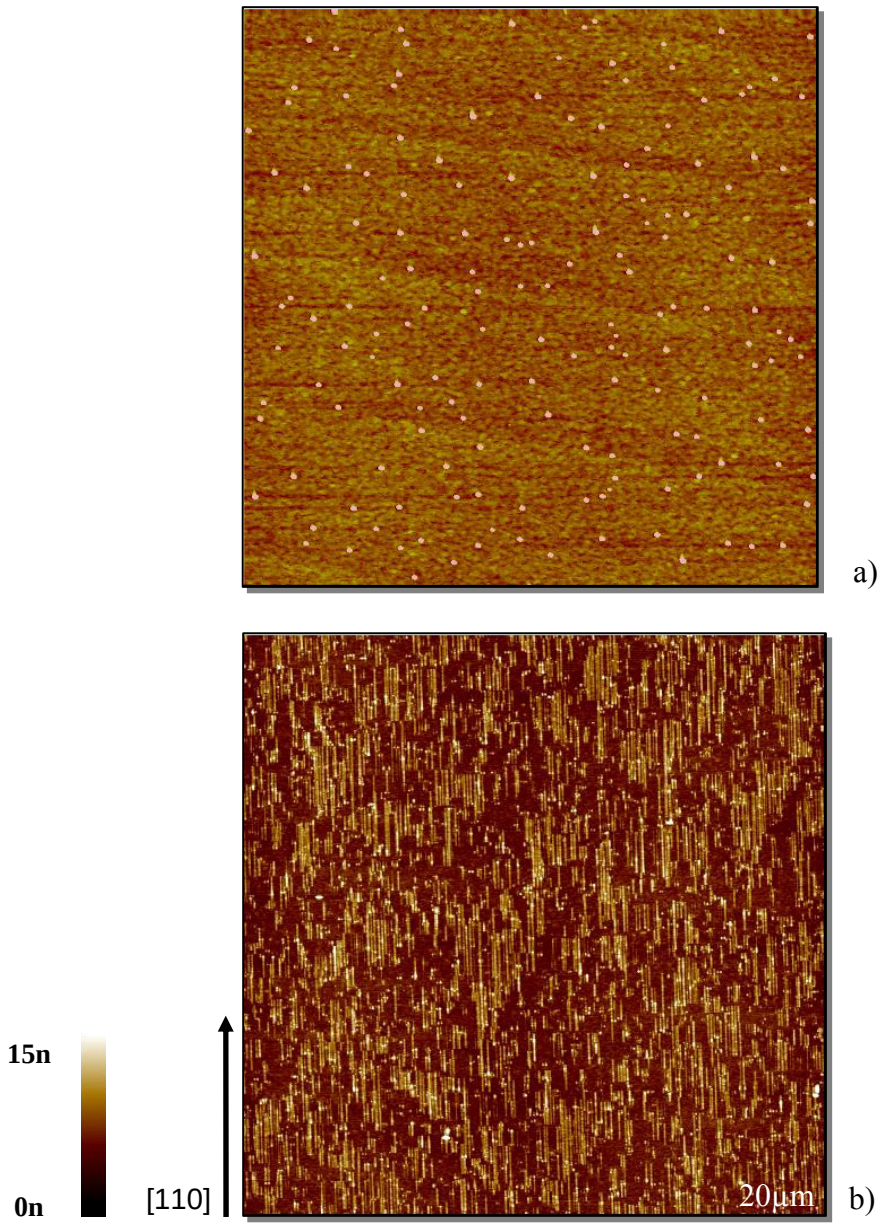

Figure 5. 6 *AFM 20 µm x 20 µm AFM scans of: (a) a GaAs / ZnSe (500Å) / ZnMgSSe (310Å) / ZnSe (45Å) structure. The dot like features are selenium clusters [15] and the surface in between has a RMS roughness of 5Å. (b) a GaAs / ZnSe (500Å) / MgS (250Å)/ ZnSe (40Å) layer, showing the pronounced 1D ridges.*

5.3.3 Refinement of Simulated Results.

New scans were taken of samples HWC167 and HWC180 as the original scans of these samples produced poorer goodness of fit (GOF) values than HWC178. In order to ensure the best possible scans, the X-ray system was re-optimized and re-aligned. Furthermore, the step size was reduced from 4 to 2 arcseconds and the count time increased from 20s to 60s in order to reduce noise and allow the best possible peak refinement. The new scans along with their simulations are shown in figure 5.7.

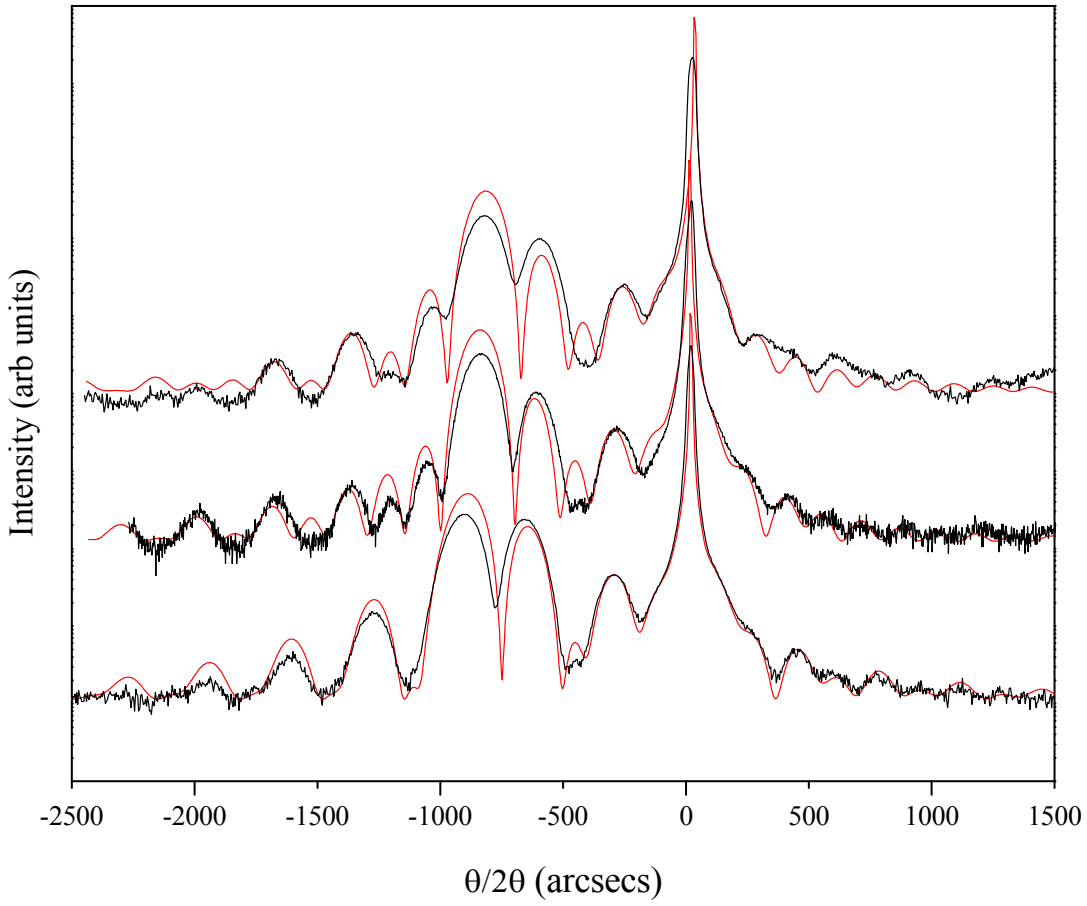

Figure 5. 7 *Re-scans/simulations of (in ascending order) HWC167, HWC178 and HWC180*

For these simulations a three layer model of ZnSe/ZnMgSSe/ZnSe was used as confirmed by the TEM results. It can be seen in the table of results that the GOF value is on average lower for this three layer system with a value of 0.14 compared to 0.18 for the previous set of simulations. The new material parameters are shown in Table 5.3 and 5.4.

Thickness (Å)	Material	Mg %	S %
HWC167			
506	ZnSe	0	0
179	Zn(1-x)Mg(x)S(y)Se(1-y)	0.77	0.64
506	ZnSe	0	0
HWC178			
571	ZnSe	0	0
85	Zn(1-x)Mg(x)S(y)Se(1-y)	0.79	0.64
565	ZnSe	0	0
HWC180			
559	ZnSe	0	0
45	Zn(1-x)Mg(x)S(y)Se(1-y)	0.82	0.60
539	ZnSe	0	0

Table 5. 3 *New data produced from rescanned and simulated results*

From these results the growth rate can be obtained along with conformation of the alloy composition. The compositions found using these new simulations are comparable to those found in section 1.

Growth Time(s)	Sample no	Thickness (Å)	Zn comp %	Mg Comp %	S Comp %	Se Comp %
120	167	179	23	77	64	36
60	178	85	22	78	64	36
30	180	45	18	82	60	40

Table 5. 4 *Thickness values for specific growth period and there respective compositions*

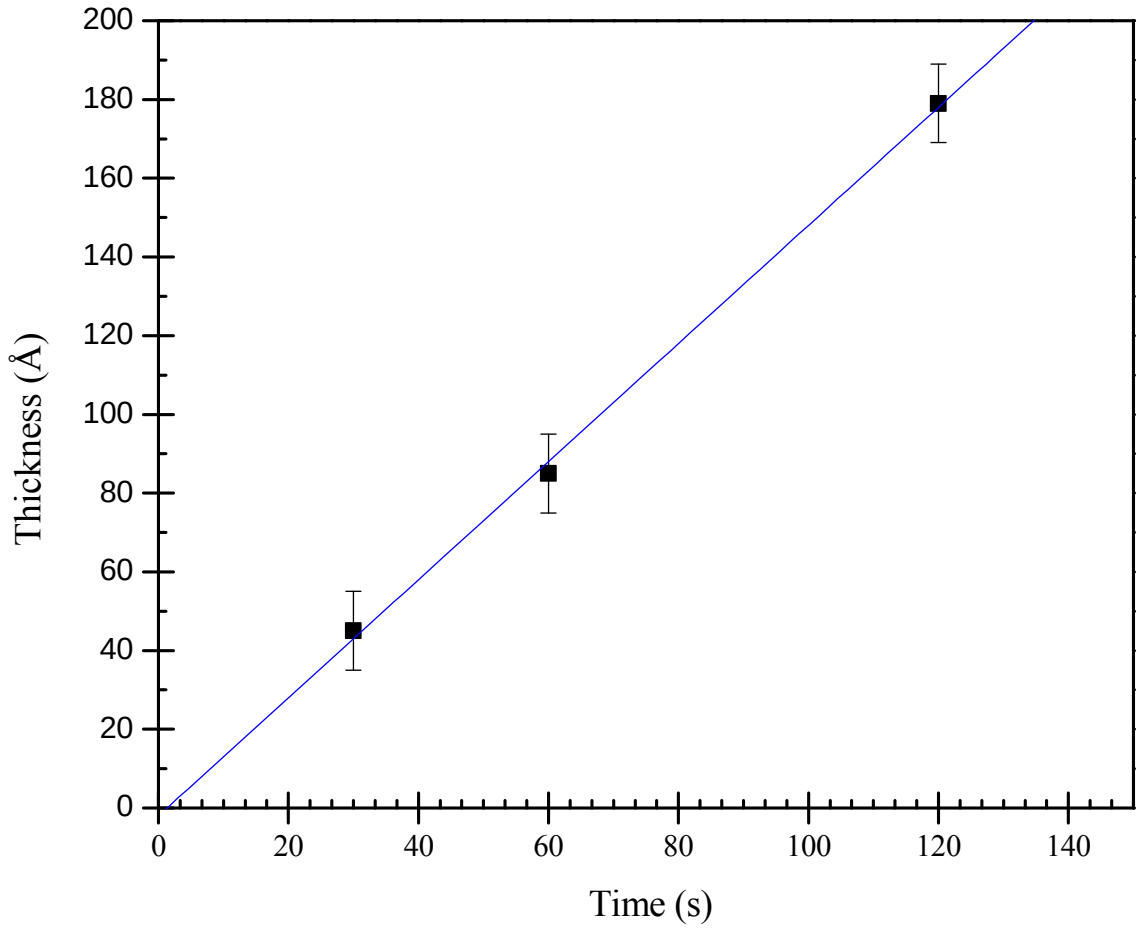

Figure 5. 8 *Graph of thickness vs time to determine growth rate.*

As with the figure 5.4 the line does not exactly intercept the origin, however in this instance this negative intercept of 2.3Å has a physical meaning arising from the boundary of intermixed composition, as shown in figure 5.9.

This would result in the negative intercept as in this model the simulation is only fitting for the central layer. It could also be simulated in a 5 layer model, but reducing the intermixed layer thickness by a factor of ten. However the value of 2.3Å found from the intercept already gives a rough idea of this mixed layer thickness, which is approximately one monolayer.

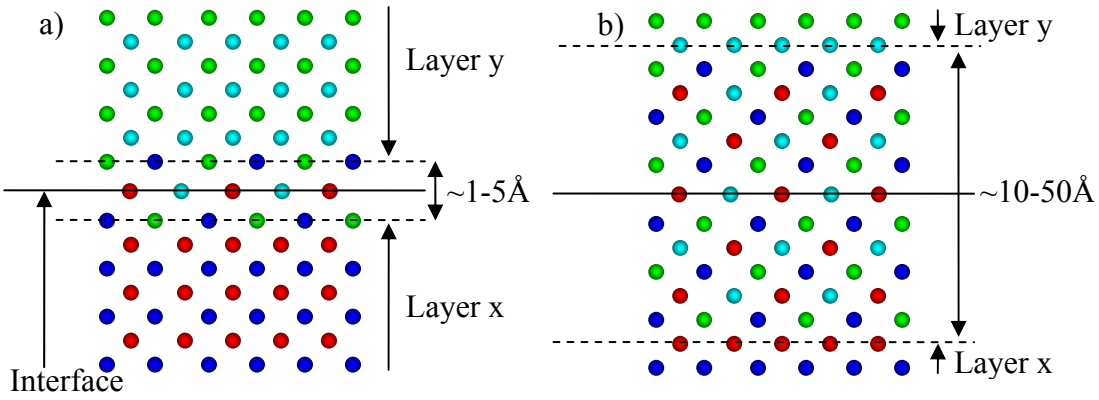

Figure 5. 9 *Schematic diagram of (left) boundary mixing, (right) diffusion intermixing. Layer x and y consist of two independent binary compounds.*

In this series of growths there were other samples grown that were found to be too thick for XRI. These were the first growths based on a growth rate estimated from MgS (~0.6Å/s). A final sample with a 15 second growth period has not been included with the rest of the group as it did not match the composition previously determined. It was first thought that the reason for this was a poor substrate clean up or failed shutter operation. Now the growth rate for the material is better defined it can be calculated that for 15s of growth the ZnMgSSe layer thickness should be approximately 22.5Å.

If it is assumed that there are graded boundaries at both the top and bottom of the alloy layer with total thickness equal to four times the value found from figure 5.8 (twice to include both the ZnSe and ZnMgSSe layers, and twice for top and bottom interfaces) then the thickness of unknown composition is in region of 10Å. So in a layer approximately 20Å thick around half of the layer thickness does not have the defined composition. The sample could be reanalyzed using the 5 layer model, however, it has been shown in chapter 3 that at the 10Å scale the XRI technique is no longer accurate [16] due to insufficient phase change introduced by the central layer. Thus, this sample can be interpreted simply as having boundary mixing in the region of 10Å. Knowing this value allows for further refinement of the structure model and may improve the simulations generated still further.

5.3.4 Determination of Alloy composition.

The previous section deals with the determination of the composition, sample thickness and thus the growth rate. However as mentioned previously, there is a continuum of compositions that lie on a lattice match line, so for a specific thickness there should be many differing compositions that will generate the same XRI pattern. This section will present an argument as to why we believe the composition determined previously is correct.

One of the parameters that is generated by the simulation software is a measure of the goodness of fit (GOF) between the simulated model and the acquired data. This GOF is used to indicate if a specific model is a realistic fit or not. A more detailed explanation of the GOF is given in chapter 2 section 2.2.6.

In normal operation when simulating an XRI scans there is more than one variable that the software has to iterate through in order to successfully model the structure. However it is possible to fix some of the variables in order to probe specific parameters and their impact on the GOF. This technique utilizes a function within the simulation software that generates a graph of the variation in GOF vs the simulation variable. By concentrating on the effect on the simulation of one specific layer and only varying one mole fraction at a time the composition of the alloy could be more confidently assigned to one specific set of values. As the alloy thickness has been previously calculated, this parameter was fixed during the simulations of the other variables which in this case were the Mg and S mole fractions.

Initially the Mg mole fraction was varied using HWC178 as the comparison sample scan. The sulfur mole fraction was fixed at 0.64 and the layer thickness at 84Å. Previously, it was mentioned that there is only a small range of composition ratios that can grow before phase decomposition occurs, although for this simulation all possible compositions were simulated, which allows us to see why many of the better GOF values must be ignored. Thus, the Mg concentration was varied from 0.1-1 to encompass the entire range. The resultant graph is shown in figure 5.10. It can be seen from this graph that there are several values for the Mg concentration that give similar if not identical GOF values in the region of 0.18 which is comparable to the average GOF from the second set of simulations (B) in table 5.5.

The periodicity observed in the GOF is due to the range of compositions for a given thickness that will give the same phase in the X-ray amplitude. As there are composition ratios that are not permitted due to the phase decomposition, some of the lower GOF's shown in figure 5.10 are disallowed. These are highlighted in red, with the allowed concentrations in green. The boundary between two regions has a degree of uncertainty as the phase decomposition region as defined by Sorokin *et al* [1] used some poorly known values for MgS and MgSe thermodynamic data (see section 5.6)

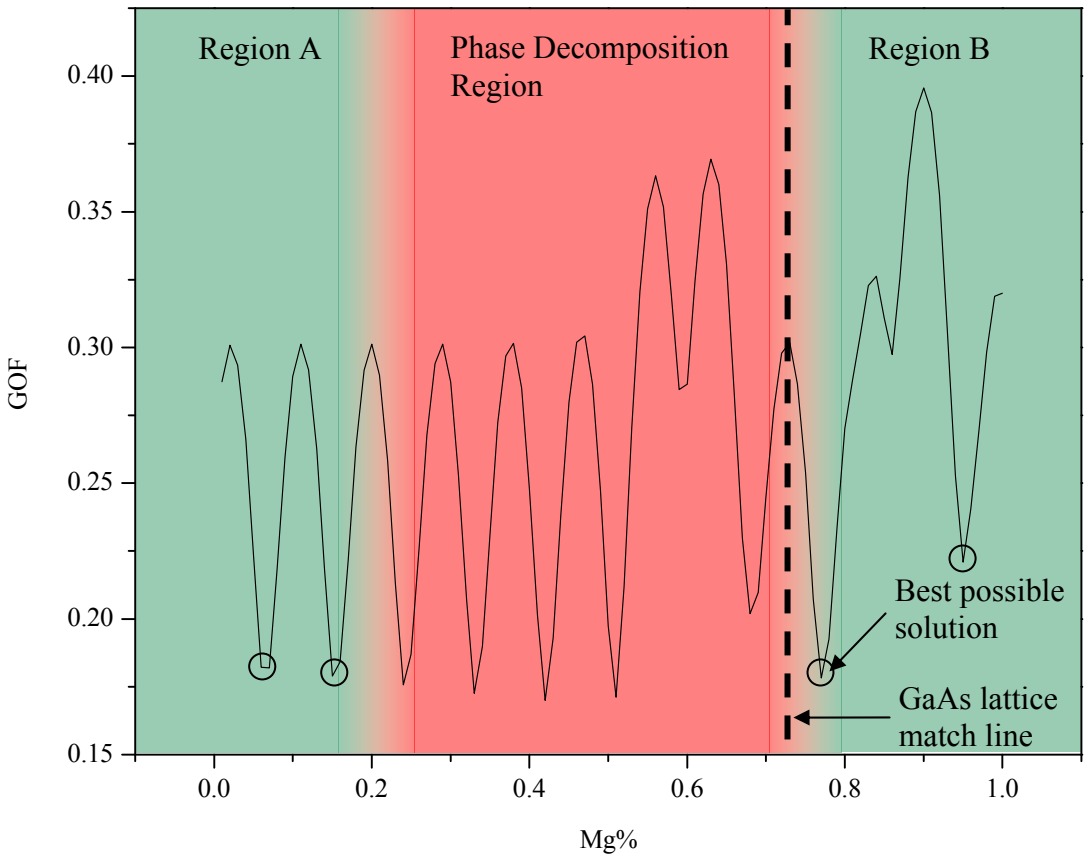

Figure 5. 10 *GOF values for ZnSe(500Å)/$Zn_{1-x}Mg_xS_{0.64}Se_{0.36}$(85Å)/ ZnSe(500Å). Green areas are the allowed compositions with the red region containing those compositions not permissible due to phase separation.*

Sample no	GOF (A)	GOF (B)
180	0.22	0.12
178	0.13	0.13
167	0.19	0.17

Table 5. 5 *GOF comparison between, (A) 5 layer model and (B) 3 layer model.*

It can be deduced from this graph that there are 4 possible Mg mole fractions with similar low GOF values (figure 5.10 circles). As this alloy was deliberately grown to reside in the upper region B of the phase diagram and is close to lattice matching we therefore deduce that the most likely value of the Mg mole fraction is approximately 0.78.

Subsequently, varying the non metal mole fractions was investigated. This was undertaken on sample no HWC180. By fixing the Mg mole fraction to 0.78 and varying the sulfur mole fraction over range 0.1-1 a similar graph could be plotted. When this data was investigated it was clear that there was a definite "best fit" from a sulfur mole fraction of approximately 0.64. The procedure above was then repeated for incremental values of thickness to observe any changes in the S concentration arising in samples of different thickness.

It can be seen in figure 5.11 that the thickness changes had no effect on the position of the best GOF, i.e. it remains fixed at 0.64, whereas the other low GOF values require changes in the sulfur concentration in order to maintain a good GOF. Noted on the graph are dashed lines, which represent lines of equal GOF as the data curves have been separated vertically for ease of interpretation. It can be seen from these simulations that for an MgS-rich alloy then the composition $Zn_{0.2}Mg_{0.8}S_{0.64}Se_{0.36}$ is the best possible fit to the experimental data.

To prove that this assumption is correct, a second characterization technique is required. By using optical characterization (either PL or absorption) the band gap can be determined and gives a clear picture of the alloy composition region. Region A on the phase diagram is the ZnSe rich region and therefore will have a band gap closer to ZnSe than MgS. This is discussed further in section 5.4.

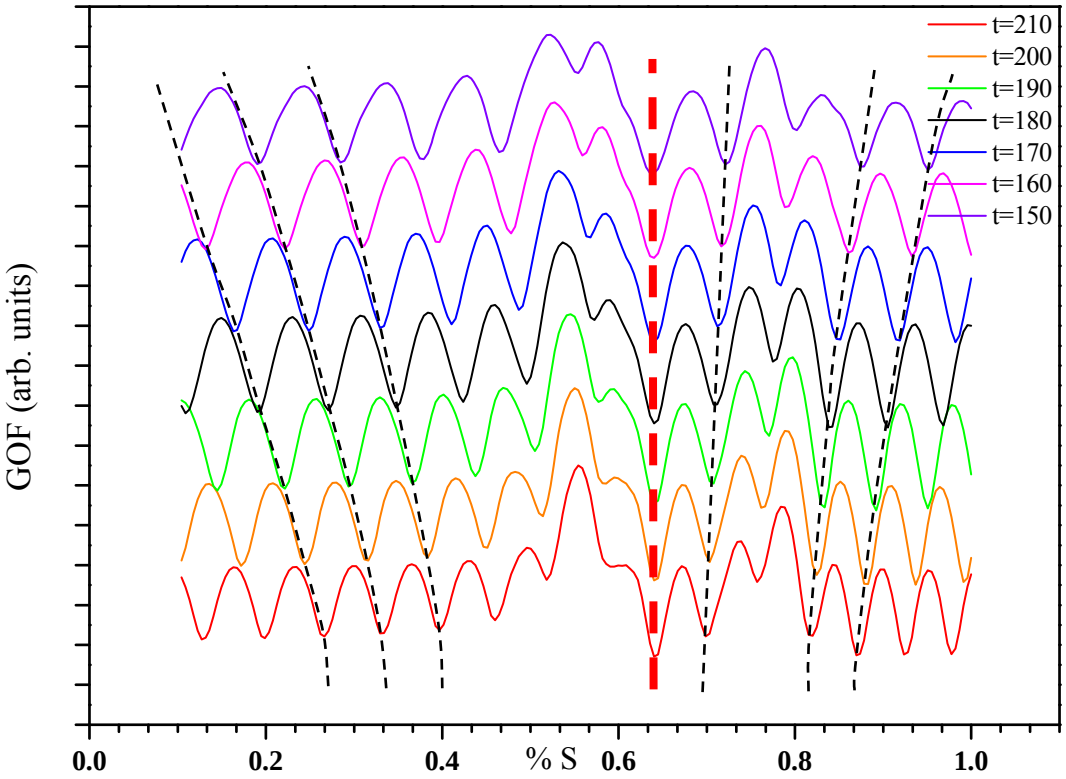

Figure 5. 11 *Graphs of simulated S concentration and GOF for range of thickness values (t measured in Å). For clarity, the curves have been separated vertically.*

Further analysis of the X-ray spectra was made to extract as much information as possible from this new material. The parameters of composition and growth rate generated by the previous investigations allow for the values for the lattice constants of all the binary compounds in the alloy, a_{MgSe} in particular, to be refined.

The simulated quaternary alloy composition obtained was found to be very sensitive to changes in $a_{MgSe,}$. Of the four binary compounds, this material had by far the widest range of experimentally determined values. In a similar manner to Sohel *et al.,* [17], a value of 5.90Å was used for a_{MgSe}, which is the mean of the reported experimental values. In our simulations by varying a_{MgSe} from 5.89 to 5.90Å it was observed that the Zn and the Se mole fractions changed by less than one percent, but varying a_{MgSe} from 5.90 to 5.91Å almost doubled the Se mole fraction, producing almost identical simulated rocking curves with very similar goodness of fit values. However, the simulations performed with the largest a_{MgSe} are regarded as unrealistic for two reasons. Firstly, they required unacceptably large interfacial regions, over 40Å wide, while the

simulations with smaller a_{MgSe} had much sharper interfaces. This is in agreement with the TEM data showing no observable intermixing. Secondly, the alloy produced had a very large strain (1.7%) to the GaAs substrate, and it is unlikely that much thicker structures, such as the sample used for TEM and AFM, could be grown without observable lattice relaxation (again not observed in TEM). Using a_{MgSe} = 5.90Å, the alloy composition $Zn_{0.22}Mg_{0.78}S_{0.64}Se_{0.36}$ was obtained for all samples grown.

5.4 Optical Characterization.

To complete the characterization of the alloy PL measurements were required in order to determine the confinement properties of the material. X-ray analysis suggests that this alloy resides in the upper region (B) of the phase diagram shown in figure 5.1 [2]. Now by examining the confinement of excitons in ZnSe QW and CdSe QD the band gap of ZnMgSSe barriers can be estimated. As MgS has a higher band gap than both ZnSe and CdSe, higher concentrations of MgS in the alloy should generate confinement analogous to that of MgS barriers, and would support the prediction of the alloy being situated in the upper region (B).

For PL measurements the ZnMgSSe was used as a barrier in sample no HWC176 in the form of a GaAs / ZnSe (500Å) / ZnMgSSe (310Å) / ZnSe (40Å) / ZnMgSSe (310Å) structure. The resulting structure and PL emission graph is shown in figure 5.12. PL spectra were taken at 77 K by using the 350nm line from an Ar-ion laser and were collected by using a 0.88-m Spex monochromator, details are discussed in chapter 2 section 2.4.

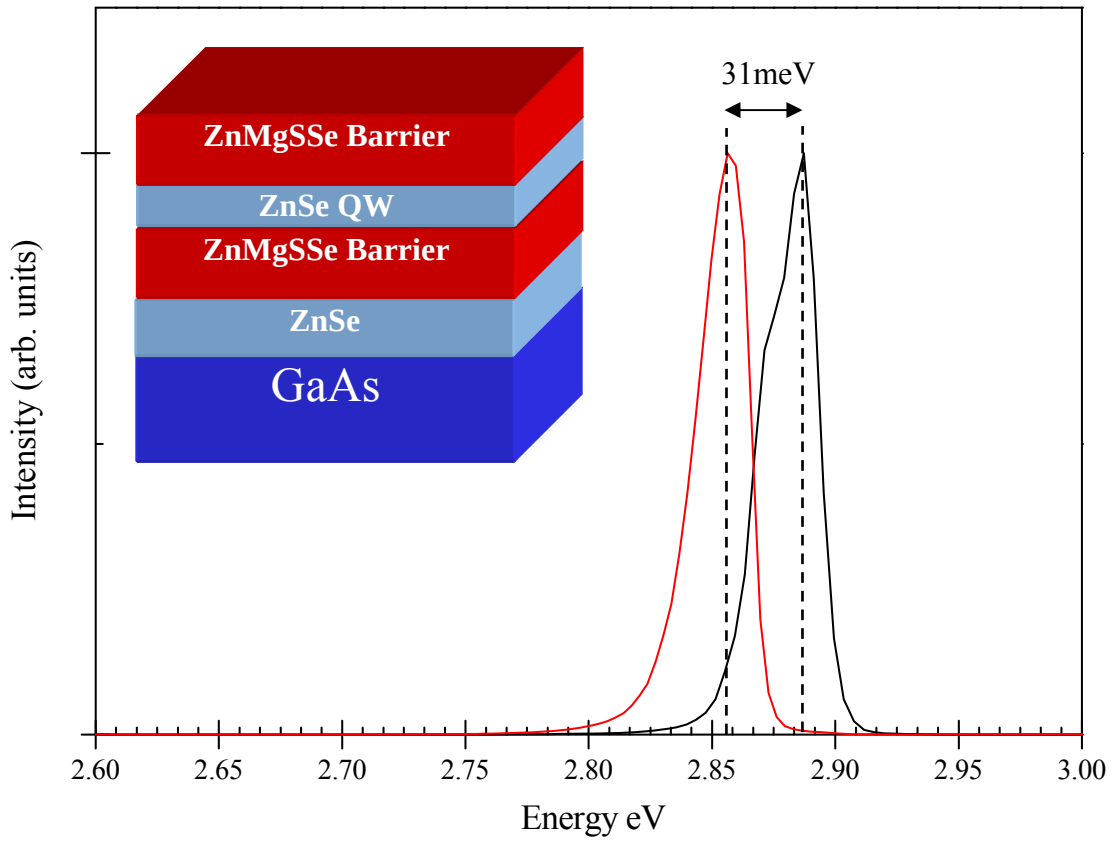

Figure 5. 12 *Structure of HWC176 and resultant PL emission. FWHM of this peak was found to be ~15.1 meV. Graph in red is a comparison structure of MgS/ZnSe/MgS with similar QW thickness.*

The PL obtained from the HWC176 was compared with PL from a similar sample with a similar 40-50Å ZnSe well and MgS barriers. It can be seen that there is little change in spectral positions between the two wells, with strong excitonic emission observed in both cases. The small change in position of 31meV can be attributed to Å variations in the well width between the two samples. However emission from the well with the MgS barriers shows a slightly larger FWHM (16 meV) than with the ZnMgSSe barriers (15.1 meV) with possibly some contribution from the interface roughness generated from the surface corrugations observed on MgS surfaces. Based on these results, it is concluded that when used with ZnSe quantum wells as a barrier material, the alloy is as good, if not slightly better than MgS.

The quaternary alloy was also used as a barrier for CdSe QD which were grown by Migration Enhanced Epitaxy (MEE). Unlike MBE, where all source material is incident

on the surface simultaneously, MEE separates the fluxes so only one source is open at any given time. By doing this improvements in the structural quality of the material are achievable [18]. During normal MBE growth the migration distance of adatoms is limited, resulting in surface roughness that may be more than a ML thick. The MEE technique, however, leads to an enhancement of the adatom migration, by exposing the growing surface to alternating beams of group II and group VI materials. A short time delay between the group II and group VI flux exposures not only enhances surface atom migration but also eliminates background interaction between the fluxes at the surface of the growing film. Sorokin *et al.* [19] found that the nominal thickness deposited increases linearly with the amount of Cd supplied up to ~0.5ML per cycle before saturating, showing that the growth rate for MEE with excess source material supplied is self-limiting at 0.5ML per cycle.

Samples grown for this study were similar in structure to previous structures which were produced for PL with the obvious replacement of ZnSe with CdSe. The Cd cell temperature during growth was set at 200^{o}C. Two samples were generated for this demonstration. The first had 11 cycles of MEE growth and the second, 9 cycles. The first sample did not successfully generate the desired emission. The 9 cycle sample did however demonstrate QD emission, shown in figure 5.13. This was a successful result as this FWHM and peak position correlated with similar QD samples grown using MgS as a barrier material, shown in red in figure 5.13 [8].

It can be concluded that the quaternary alloy has the same if not better confinement qualities compared to those of MgS. Furthermore, by exhibiting large exciton confinement, the alloy is confirmed as being from region B in figure 5.1. Now it can be confidently stated that the composition of the alloy is, $Zn_{0.22}Mg_{0.78}S_{0.64}Se_{0.36}$ with a growth rate of 1.5Å/s.

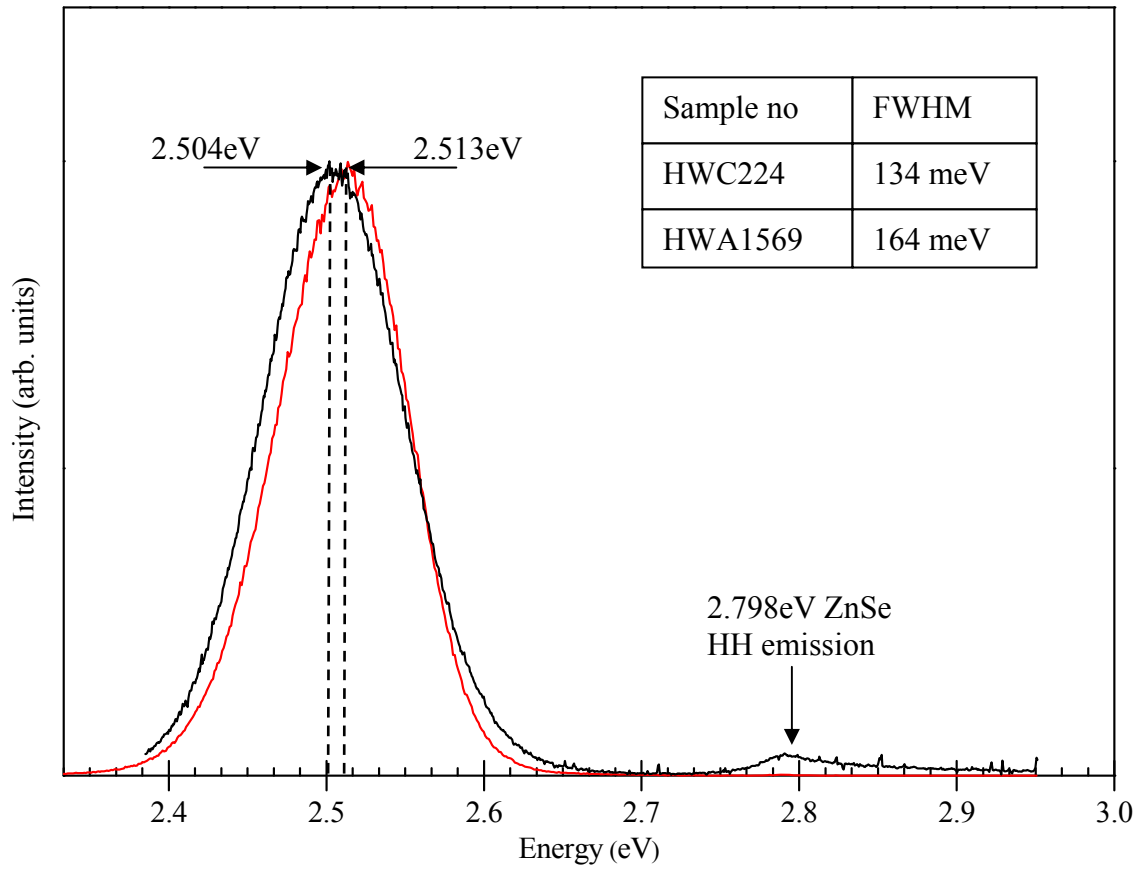

Figure 5. 13 *77k PL emission spectra from QD sample HWC224 in black compared to previously grown sample HWA1569 MgS/CdSe/MgS sample in red.*

With the information gathered from the characterization of the material the next stage of the development could be undertaken. This involved investigating the resistance of the alloy to etching in HCl with an aim of generating a lift off structure containing an MgS sacrificial layer, ZnMgSSe barriers and ZnSe QW. The next section deals with this investigation.

5.5 Lift off structure Development.

The aim of this study is to try and incorporate both the quaternary alloy and MgS into a lift off sample for the development of a polariton structure. It has been previously demonstrated that MgS is soluble in HCl and allows for II-VI epitaxial hetrostuctures to be removed from the GaAs substrate [4], but the inclusion of MgS in the structure as a sacrificial layer inhibits its use as a barrier material in the nanostructure. As demonstrated in the previous sections $Zn_{0.22}Mg_{0.78}S_{0.64}Se_{0.36}$ is a suitable replacement

for MgS so structures were grown incorporating both MgS and ZnMgSSe in order to test the alloy's solubility in HCl. Polariton structures produced at HW typically require the use of ZnSe/ZnCdSe QW, however due to the ZnSe QW peak position being at a well defined energy and strain sensitive, a ZnSe emission region was chosen to give a clear indication that the sample has been removed from substrate.

Sample growth was carried out at 240ºC using the standard growth method as described previously for MgS [2] and ZnMgSSe in section 5.2 [20], The sample had the structure GaAs / ZnSe (buffer, 600Å) / MgS (sacrificial layer, 100Å) / ZnSe (spacer, 800Å) / ZnMgSSe (barrier, 720Å) /ZnSe (well, 40Å) ZnMgSSe (barrier, 720Å).

After growth, small pieces of the sample approximately 3mm x 3mm were cleaved and then subject to the standard epitaxial lift off procedure [5,21] shown in figure 5.14. Once detached from the substrate, the epitaxial layers were transferred to a glass slide.

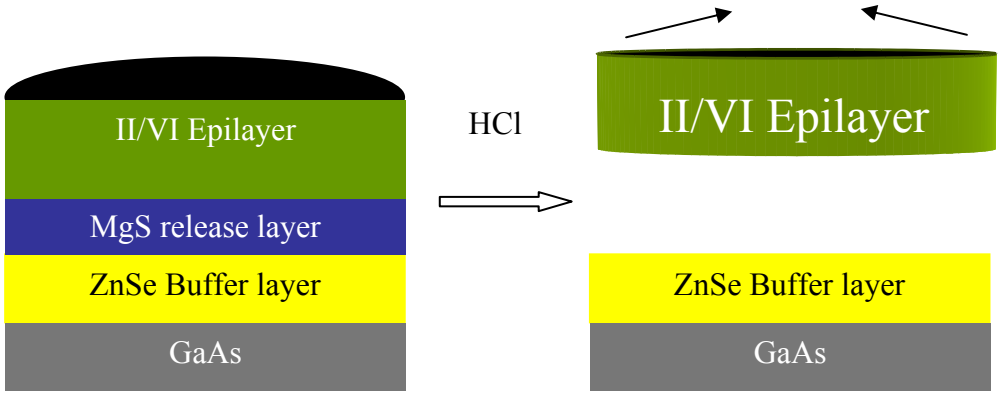

Figure 5. 14 *Schematic diagram showing the method used for the lift off technology. The black section on top is wax. Surface tension from the wax pulls uniformly on the top layer, allowing HCl to penetrate into centre of the MgS layer.*

PL spectra before (a) and after (b) epitaxial lift-off are shown in figure 5.15. In order to show the weaker peaks which are present, the data has been plotted on a logarithmic scale and the two spectra are separated vertically. In the unetched structure, the strongest peak does not arise from the 40Å ZnSe quantum well, at 2.867eV, but from the much wider ZnSe spacer layer, which shows intense emission from the heavy hole state at 2.795 eV and weaker emission from the higher energy light hole state at 2.807

eV. On the low energy side of the peak are a series of poorly resolved shoulders with a separation of approximately 30meV which are most likely phonon replicas. Also visible, centred at 2.7122 eV is a very weak peak which we attribute to defect related emission from the ZnSe buffer layer. As the peak is weak, its exact origin can not be determined, however it is in the correct position for an acceptor bound exciton, and could therefore be associated with arsenic doping or zinc vacancies close to the GaAs/ZnSe interface [22].

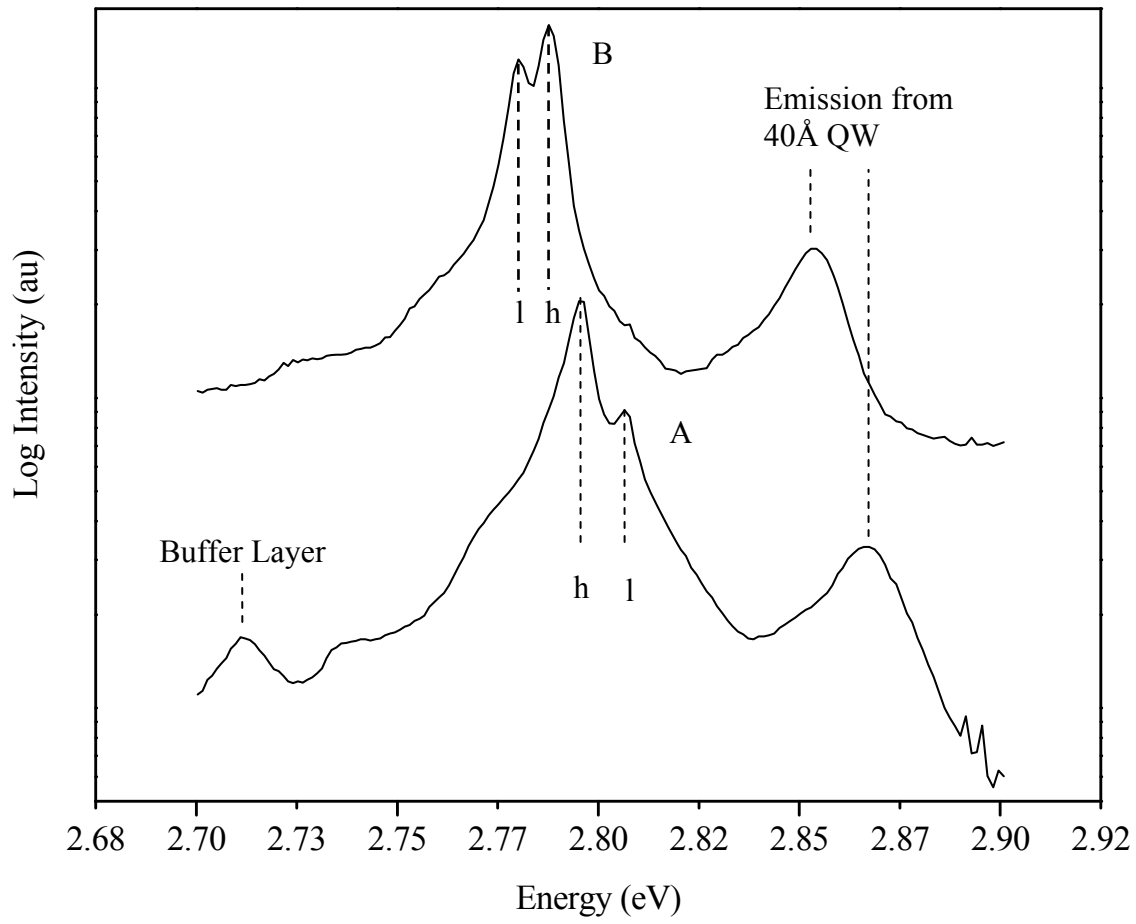

Figure 5. 15 *77K PL spectra from sample HWC186 (a) before and (b) after lift-off. Emission from the ZnSe buffer and 40Å quantum well layers is indicated. Emission from the spacer layer is shown as h (heavy hole exciton) and l (light hole exciton).*

Comparison with the spectrum from the etched layer shows that this peak has completely disappeared, and therefore must arise from the ZnSe buffer layer which is removed in the etching process. All other peaks remain in the etched layer, although there are changes in intensity and also a shift in peak positions. Comparison of the

intensities from before and after etching shows that there is no reduction in intensity from the ZnSe quantum well.

The wider ZnSe spacer layer however is significantly affected with a reduction in emission intensity of over one order of magnitude. During the etching procedure and subsequent sample mounting, the layer loses one of its barriers, acquires a free surface which is exposed to an acidic solution and is subsequently placed in contact with glass. PL spectra are routinely obtained from epitaxial ZnSe layers of comparable thickness, which also have one free surface, but this layer has been in contact with an acidic etching solution and then been transferred to a glass substrate. Despite this, the signal from the top ZnSe layer remains and is not associated with enhanced defect emission, indicating that the mechanical stresses introduced in the transfer process are not significant.

After the etching procedure it can be seen that the entire spectrum is shifted to lower energy. While attached to the GaAs substrate, the ZnSe wells are under a compressive in-plane strain of approximately 0.27%. With the substrate removed, reduction in the bandgap shows that the lateral strain in the well is reduced, but is still not eliminated. The peak positions and intensities in the ZnSe spacer layer suggest that the lowest energy peak is now the light hole exciton, which indicates that there is still a residual strain in the ZnSe layers, but it is now tensile [23]. A residual tensile strain has not been observed in our previous work on ZnSe/ZnCdSe lift off structures [6,22], and the origin in this case has not been determined. Residual wax deposits on the samples are known to cause significant strains when samples are cooled to 77K, but have been eliminated as the cause in the present case. A more likely explanation is that the structure has adopted a minimum energy configuration with the ZnSe under tension and $Zn_{0.2}Mg_{0.8}S_{0.64}Se_{0.36}$ remaining under compressive strain. As the stiffness coefficients of the alloy have not been determined, this can not be confirmed without the growth of a larger set of samples with different barrier widths.

To achieve the goal of polariton observation, the Nano-Optics group at Heriot-Watt, working in conjunction with our group have designed a suitable structure. However before growth two quaternary alloy parameters, the band gap and the refractive index were needed. Previously, PL showed that the alloy band gap is very large, ~4eV, as the

alloy has confinement behavior similar to MgS. As the laser used for PL emits at ~350nm, band gap emission could not be observed.

A transmission measurement could be obtained for the alloy if it was grown as part of a lift off sample, thus allowing the removal of the GaAs substrate. By using the Shimadzu uv3100 spectrometer the absorption curve over a wide range of wavelengths could be obtained. An epitaxial lift off sample of GaAs/ZnSe(500Å)/MgS(50Å)-/ZnSe(100Å)/ZnMgSSe(*thick layer*) (HWC200) was grown using the same growth conditions as before. The 100Å ZnSe layer is present to prevent any intermixing between the MgS and the quaternary alloy. Once grown, the sample was placed in the HCl and removed from the substrate. The epitaxial layer was attached to a glass slide for analysis. Using a deuterium lamp and an array of PbS, InGaAs, and Photomultiplier tube detectors, the Shimadzu has the ability to scan over a very large energy range (in region of 1.7-6.5eV).

Figure 5.16 (inset) shows the transmission spectra for 4 separate parts of the wafer. It can be clearly seen from this graph that there is a distinct energy where there is no longer any transmission. The reason for the wide spread in transmission intensity can be explained by changes in the initial intensity of the incident light. Importantly, if all 4 graphs are scaled independently and normalized they provide a single absorption curve, figure 5.16. The best estimate of the band gap is obtained by continuing the gradient of the straightest part of the graph and where this intercepts the energy axis is the value of the band gap.

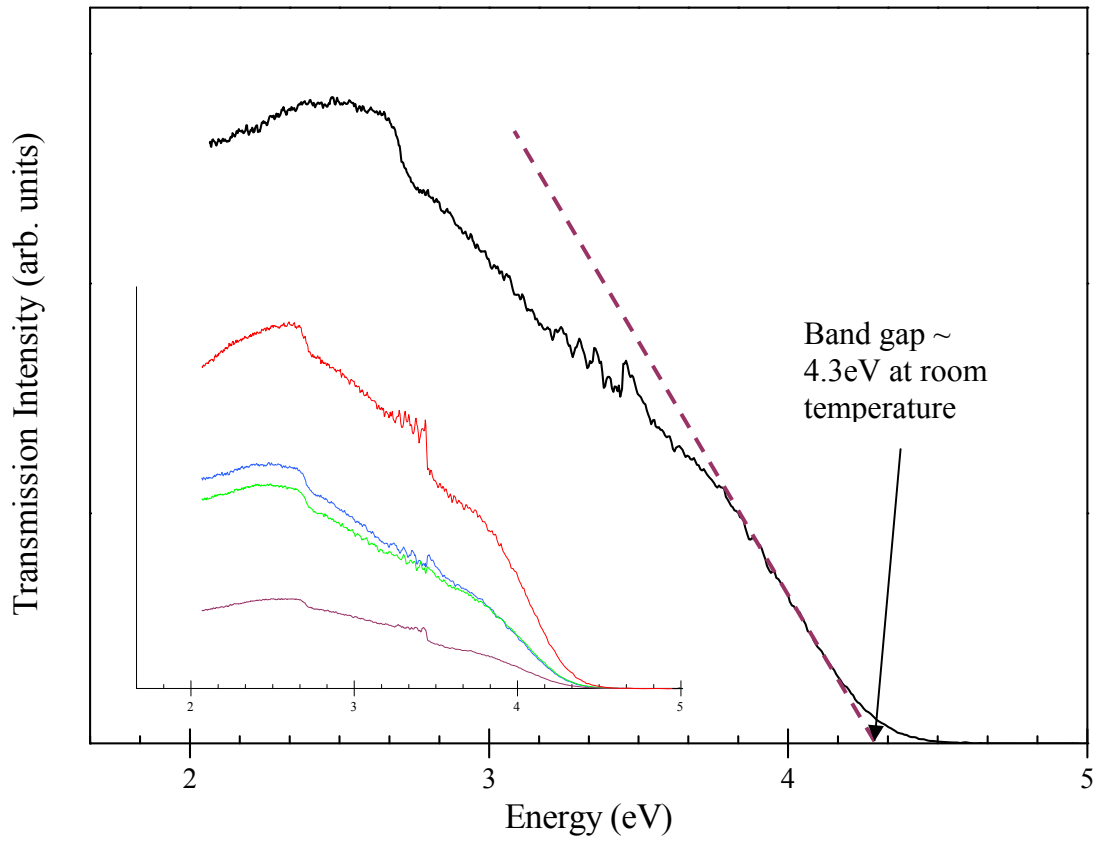

Figure 5. 16 *Band edge measurements from the transmission measurements taken. Insert is raw data with same axis as normalized plot (black)*

The best estimate of the band gap for the quaternary alloy is 4.3eV. Unfortunately the sample was not thick enough to determine the refractive index and this will need to be revisited in order to progress with further polariton studies. This value for the band gap of the material does however concur with our previous interpretation that this is a MgS-rich alloy.

5.6 Mechanism of formation of ZnMgSSe.

The majority of the work presented in this chapter has been conducted with the aim of characterizing the optical and structural properties of the material. However, there is more information that can be extracted concerning the structural and growth mechanism of the material under study. Workers at the Ioffe Institute, St Petersburg [1] have calculated the binodal and spinodal decomposition phase map for ZnMgSse. Similarly this group has determined an accomodation coefficient for Zn on ZnSe and ZnMgSSe [24] under stoichiometric growth conditions and predicted the accommodation coefficient of Mg on ZnMgSSe. In this section these studies will be used to recalculate the upper boundary for the enthalpy of formation and used to estimate an incorporation coefficient for Mg in MgS.

5.6.1 Upper boundary for the Enthalpy of formation of MgS.

The ZnMgSSe phase diagram was determined previously by using a regular solution model at a growth temperature of 300ºC [1]. These calculations showed that $Zn_{0.20}Mg_{0.80}S_{0.64}Se_{0.36}$ lies inside the spinodal decomposition curve, meaning that it should spontaneously phase separate into MgS-rich and ZnSe-rich components as shown in figure 5.17.

The resultant phase-separated alloys should have different lattice constants and would therefore generate a periodic strain field within the ZnMgSSe layer. Such a strain field is incompatible with the well-resolved fringes observed in the XRI spectrum (figure 5.7), so therefore $Zn_{0.20}Mg_{0.80}S_{0.64}Se_{0.36}$ must be a single phase. Also cross sectional TEM images (figure 5.5) showed that the material is single phase and has not undergone phase separation.

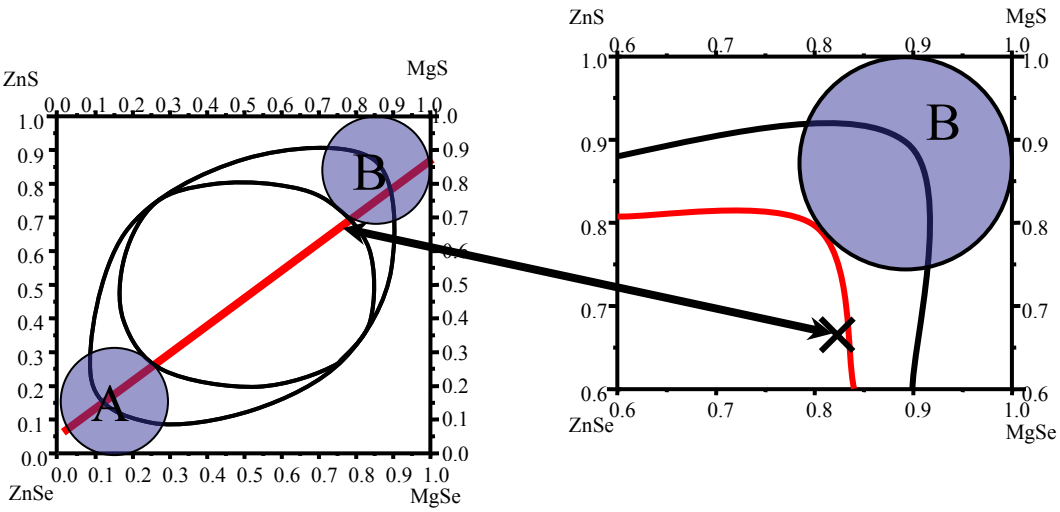

Figure 5. 17 *Expansion of the initial phase diagrapm [1] to highlight that the quaternary alloy* $Zn_{0.20}Mg_{0.80}S_{0.64}Se_{0.36}$ *lies within the phase decomposition region.*

The original model used in the calculations of the phase diagram was rerun as a Mathcad program in to alter some of the model's parameters. The model requires the values of the lattice constants, the enthalpies, and the entropies of formation for all four binary compounds. The only other adjustable parameter was the temperature. In our calculations, a slightly different value for the MgS lattice constant than used previously was (5.622Å) which was obtained from our samples. The larger values for the MgSe lattice constant, which increase the Se mole fraction, as mentioned during the structural investigation (section 5.3), also make the spontaneous phase separation more likely. The calculations were then repeated at a lower growth temperature of 240°C as well as 300°C, which was used originally [1]. Even allowing for these changes, $Zn_{0.20}Mg_{0.80}S_{0.64}Se_{0.36}$ should spontaneously phase separate (indeed, a lower growth temperature actually makes this slightly more likely).

The exact position of the spinodal curve is sensitive to the values of the thermodynamic parameters used, in particular the enthalpy. In their calculation, Sorokin *et al.* [1] estimated a value for the unknown enthalpy of formation of zinc-blende MgS from the known enthalpy of formation of the rocksalt phase of MgS. The new value was estimated from the 1/3rd reduction in the number of atomic bonds from rocksalt to Zinc

Blende, meaning the estimated enthalpy of formation for MgS is 2/3rd that of rocksalt. Because of this estimation the value of the enthalpy of formation of ZB MgS is poorly defined and is open to refinement.

By varying the entropy of MgS in the model it was observed that a very large increase in the accepted value was required in order to change significantly the position of the decomposition region. However it was found that reducing the enthalpy of formation (MgS) by less than 2%, from -235 to -231 kJ mol^{-1}, was sufficient to place $Zn_{0.20}Mg_{0.80}S_{0.64}Se_{0.36}$ outside the spinodal decomposition curve. The growth of this alloy composition can, therefore, be used to determine an upper bound for the magnitude of the enthalpy of formation of zinc-blende MgS.

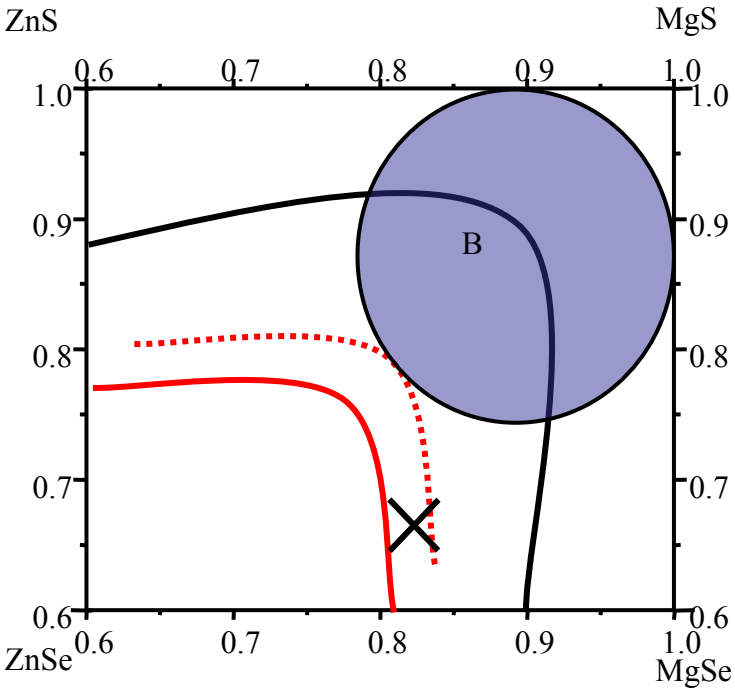

Figure 5. 18 *New boundary for the phase decomposition region determined by changing the enthalpy of formation of MgS.*

5.6.2 Determination of the value of the Mg accommodation coefficient.

The accommodation coefficient of a particular element is the fraction of the atoms that incorporate into the epilayer for a given flux arriving at the surface. Changes in growth temperature and II-VI flux ratio can affect the accommodation coefficient so the values determined here are specific to our growth conditions. Previously there have been few studies on the accommodation coefficient of Zn in ZnSe and Mg in ZnMgSSe and these will be used in this section to determine the accommodation coefficient of Mg in MgS.

In the work by Sorokin *et al* [24] on the growth of ZnMgSSe under non-metal rich conditions the accommodation coefficient for Mg in ZnMgSSe was assumed to be 1. This section will look at the growth rates of ZnSe, ZnMgS, and ZnMgSSe to investigate weather this assumption is true when the Mg containing materials are grown under metal rich conditions and generate an upper bound for the Mg accommodation coefficient in MgS.

From the growth rate the incorporated atomic flux of any element can be determined by the relationship:

$$I_{x(y)} = \frac{4g}{a^3} \qquad \text{Equation 5.1}$$

Where, $I_{x(y)}$ is the incorporation flux for species x incorporated into material y, g is the growth rate and a is the lattice parameter. In a similar manner, the notation $J_{x(y)}$ is used to define the arrival flux at the surface. All materials presented here have similar lattice parameters within the error associated with the measurement of the growth rate therefore $a=a_{GaAs}$ (5.6Å). The samples used in this section to determine the growth rates were the ZnMgSSe samples discussed in section 5.3.2 and the MgS samples discussed in chapter 4.

If this is applied to the growth rate for ZnSe then an incorporation flux of $1.367\times10^{14}\,\mathrm{cm^{-2}s^{-1}}$ is found. Sorokin et al [23] demonstrated that under stoichiometric growth conditions only 0.67 of the Zn flux arriving at the surface would incorporate into the epilayer, giving an Zn arrival flux $J_{Zn(ZnSe)}$ of $2.04\times10^{14}\,\mathrm{cm^{-2}s^{-1}}$.

In the quaternary alloy growth Zn is supplied to the surface from both the Zn and ZnS sources, which must both be considered when evaluating the Zn incorporation in ZnMgSSe. Therefore the arrival flux of Zn on the MgS surface $(J_{Zn(MgS)})$ has to be determined as this will give the total Zn available for incorporation.

5.6.2.1 MgS accommodation coefficient.

By determining $I_{Zn(MgS)}$ and $I_{S(MgS)}$ the minimum incident Zn flux from the ZnS source can be found. $I_{S(MgS)}$ is found from the growth rate of 0.5Å/s for MgS. However the incorporation of the individual mole fractions of Zn and Mg are needed to determine how much Zn is incident at the surface from the ZnS source. From previous studies of MgS the mole fraction of Zn in the compound is a maximum of 0.03 [2] so the incorporation of Zn and Mg can be found from:

$$I_{Mg(MgS)} = I_{S(MgS)}(1-0.03) = 1.105\times10^{14}\,\mathrm{cm^{-2}s^{-1}} \qquad \text{Equation 5.2}$$

$$I_{Zn(MgS)} = I_{S(MgS)}\times(0.03) = 0.03\times10^{14}\,\mathrm{cm^{-2}s^{-1}} \qquad \text{Equation 5.3}$$

To obtain estimates of the accommodation coefficients, we will assume initially that all sulfur is incorporated, i.e. α_s=1. This allows us to calculate the fluxes impinging on the surface:

$$J_{Zn(MgS)} = I_{S(MgS)} = 1.14\times10^{14}\,\mathrm{cm^{-2}s^{-1}} \qquad \text{Equation 5.4}$$

From this the minimum Zn flux incident on the surface of MgS is $1.14E^{14}\mathrm{cm^{-2}s^{-1}}$ and the minimum Zn accommodation coefficient $\alpha_{Zn(MgS)}$ can be found from the ratio of arrival flux to incorporated flux so that;

$$\alpha_{Zn(MgS)} = \frac{I_{Zn(MgS)}}{J_{Zn(MgS)}} = \frac{0.03\times10^{14}}{1.14\times10^{14}} \approx 0.03 \qquad \text{Equation 5.5}$$

5.6.2.2 Accommodation coefficients in ZnMgSSe.

Knowing $J_{Zn(ZnS)}$, and the Zn flux arriving at the surface from the Zn source, the total amount of Zn arriving at the surface during the growth of the quaternary alloy can be found by:

$$J_{Zn(ZnMgSSe)} = J_{Zn(ZnSe)} + J_{Zn(MgS)} = (2.04 + 1.14) \times 10^{14} = 3.18 \times 10^{14}\,\mathrm{cm^{-2}s^{-1}} \qquad \text{Equation 5.6}$$

From this the accommodation coefficient of Zn in the quaternary alloy can be found. As determined in sections 5.3.2 the mole fraction of Zn incorporated into the alloy is 0.2 so:

$$I_{Zn(ZnMgSSe)} = I_{(ZnMgSSe)} \times (0.2) = (3.43 \times 0.2) \times 10^{14} = 0.7 \times 10^{14}\,\mathrm{cm^{-2}s^{-1}} \qquad \text{Equation 5.7}$$

Giving an accommodation coefficient for Zn in the alloy of:

$$\alpha_{Zn(ZnMgSSe)} = \frac{I_{Zn(ZnMgSSe)}}{J_{Zn(ZnMgSSe)}} = \frac{0.7 \times 10^{14}}{3.44 \times 10^{14}} = 0.2 \qquad \text{Equation 5.8}$$

When this accommodation coefficient is compared to that of Zn in ZnSe grown under non metal rich conditions (0.67) and MgS which is grown under very metal rich conditions it is seen that it is an intermediate value between the two. This is as expected for an alloy of these two materials and shows that the growth conditions, although still in the metal rich regime, are closer to stoichiometric.

In the previous section the arrival flux of Mg was not known and therefore the accommodation coefficient could not be determined for this material. However assuming $\alpha_{Mg(ZnMgSSe)}$ is one for all compositions, even those slightly metal rich (as in the present case) then the arrival flux of Mg on the surface can be determined. As the same Mg flux is used for both MgS and ZnMgSSe the accommodation coefficient of Mg in MgS can then be found.

Again, from section 5.3.2 the mole fraction of Mg in the alloy is 0.8 therefore

$$I_{Mg(ZnMgSSe)} = I_{(ZnMgSSe)} \times (0.8) = 3.34 \times (0.8) = 2.7 \times 10^{14}\,\mathrm{cm^{-2}s^{-1}} \qquad \text{Equation 5.9}$$

And assuming $\alpha_{Mg(ZnMgSSe)}$=1 gives:

$$J_{Mg(MgS)} = J_{Mg(ZnMgSSe)} = I_{Mg(ZnMgSSe)} \qquad \text{Equation 5.10}$$

This value for $J_{Mg(MgS)}$ can be used with the $I_{Mg(MgS)}$ found from equation 5.2 to give;

$$\alpha_{Mg(MgS)} = \frac{I_{Mg(MgS)}}{J_{Mg(ZnMgSSe)}} = \frac{1.105 \times 10^{14}}{2.7 \times 10^{14}} = 0.4 \qquad \text{Equation 5.11}$$

This gives the accommodation confident for Mg in MgS as 0.4 when grown under the normal growth conditions used at Heriot-Watt.

Although some assumptions have been made, this is the first time that this value for the accommodation coefficient of Mg in MgS has been estimated.

5.7 Conclusion and Future work:

It has been found that MgS-rich samples of ZnMgSSe can be grown in the zinc-blende crystal structure lattice matched to GaAs by using molecular beam epitaxy. Analysis by XRI showed that the alloy's composition was $Zn_{0.20}Mg_{0.80}S_{0.64}Se_{0.36}$ with a growth rate of 1.5Å/s. Unlike MgS layers previously grown under similar conditions, this alloy did not develop pronounced growth ridges. 77K PL from ZnSe quantum wells and CdSe QD with $Zn_{0.2}Mg_{0.8}S_{0.64}Se_{0.36}$ barriers is comparable in intensity to wells with MgS barriers. PL from the resulting structure showed a sharp peak.

Our analysis, especially TEM and XRI, showed that $Zn_{0.20}Mg_{0.80}S_{0.64}Se_{0.36}$ was a single phase material whereas previous calculations suggested that an alloy of this composition should phase separate. The discrepancy with the calculation can be removed if the estimated value of the enthalpy of formation of zinc-blende MgS is reduced slightly too less than -231.1 kJ mol^{-1}. By investigating the accommodation coefficients of MgS, ZnSe, and ZnMgSSe an estimate for the accommodation coefficient of Mg in MgS was determined to be 0.4.

As a stage towards the development of a viable lift-off technology it has been demonstrated that the alloy $Zn_{0.2}Mg_{0.8}S_{0.64}Se_{0.36}$ can be successfully used as a barrier material with ZnSe quantum wells, in structures grown by MBE on top of MgS sacrificial layers. The $Zn_{0.2}Mg_{0.8}S_{0.64}Se_{0.36}$ layers resist the etching solution and trial structures have been successfully transferred onto glass substrates. This procedure has not resulted in the introduction of defect levels observable in the PL and after lift off the etched structure shows no decrease in intensity in the quantum well emission. Changes in the emission wavelength are attributable to the change in the strain state of the ZnSe layers.

This allows future development of the material including the possibility of using the material as a recombination region. Until now, MgS can only confine excitons in materials with smaller band gaps, limiting its use as a recombination region. It is however now possible to use the quaternary alloy as the recombination region with MgS barriers. This would in theory provide strong PL emission in the 4.3eV region.

The estimation of the enthalpy and accomodation coefficients are obtained from a small sample series and as such to better define these a larger study of the alloys is required where by the relative ratios of material are varied along with there respective growth rates to see if the assumptions and accommodation values still hold true. Subsequently, this work may be of use in improving the growth of other metastable compounds such as MnS and CrS.

5.8 References.

[1] V. S. Sorokin, S. V. Sorokin, V. A. Kaygorodov, and S. V. Ivanov, J. Crystal Growth 214/215, 130 (2000).

[2] C. Bradford, C. B. O'Donnell, B. Urbaszek, A. Balocchi, C. Morhain, K. A. Prior, and B.C. Cavenett, Appl. Phys. Lett. 76, 3929 (2000).

[3] E. Yablonovitch, T. Gmitter, J.P. Harbison, R. Bhat, Appl. Phys. Lett., 51 (1987) :2222

[4] C. Bradford, A. Balocchi, A. Curran, R.J. Warburton, K.A. Prior, B.C. Cavenett, J Crystal Growth, 278 (2005) 325

[5] A. Curran, J.K. Morrod, K.A. Prior, A.K. Kar, R.J. Warburton, Semiconductor Sci. and Technol. 22 (2007) 1189

[6] A. Curran, R. Barbour, J.K. Morrod, K.A. Prior, A.K. Kar, R.J. Warburton, J Korean Phys Soc, 53, 5, 2008, 3007-3011

[7] C. Bradford, C.B. O'Donnell, B. Urbaszek, K.A. Prior, B.C. Cavenett, Phys. Rev. B, 64 (2001) 195309

[8] M. Funato, A. Balocchi, C. Bradford, K.A. Prior, B.C. Cavenett, Appl. Phys. Lett. 80 (2002) 443

[9] M. Funato, K. Omae, Y. Kawakami, Sg. Fujita, C. Bradford, A. Balocchi, K.A. Prior, B.C. Cavenett, Phys. Rev. B, 73 (2006) 245308

[10] L.H. Kuo, K. Kimura, S. Miwa, T. Yasuda, T. Yao, Appl. Phys. Lett., 69 (1996) 1408

[11] L. Tapfer and K. Ploog, Phys Rev. B 40 (1989) 9802

[12] B.K. Tanner, J. Phys. D: Appl. Phys. 26 (1993) A151

[13] K.A. Prior, X. Tang, C. O'Donnell, C. Bradford, L. David, B.C. Cavenett, J. Crystal Growth, 251 (2003) 565

[14] C. O'Donnell, MBE Growth and Characterization of ZnSe-based II-VI Semiconductors

[15] K. Leonardi, H. Heinke, K. Ohkawa, D. Hommel, H. Selke, F. Gindele, U. Woggon, Appl. Phys. Lett. 71, 1510 (1997), 1510-1512

[16] H. Holloway, J. Appl. Phys. 67, (1990), 6229

[17] M. Sohel, M. Munoz, and M. C. Tamargo, Appl. Phys. Lett. 85, 2794 (2004).

[18] Y. Horikoshi, J. Crystal Growth, 201/202 (1999) 150.

[19] S. Sorokin, T. Shubina, A. Toropov, I. Sedova, A. Sitnikova, R. Zolotareva, S. Ivanov and P. Kop'ev, J. Crystal Growth 201/202 (1999) 461

[20] R.T. Moug, C. Bradford, D. Thuau, A. Curran, R.J. Warburton, K.A. Prior, J. Korean Phys. Soc., 53 (2008) 3004-3006

[21] C. Bradford, A. Balocchi, A. Curran, R.J. Warburton, K.A. Prior, B.C. Cavenett, J Cryst Growth, 278, (2005), 325-8

[22] J. Gutowski, N. Presser, G. Gudlek, phys stat sol, 120, (1990), 11-59

[23] K. Mohammed, DA. Cammack, R. Dalby, P. Newbury, BL. Greenberg, J. Petruzzello, RN. Bhargava, Appl Phys Lett 50, (1987), 37-39

[24] S. Ivanov, S. Sorokin, I. Krestnikov, N. Faleev, B. Ber, I, Sedova, Yu Kudryavstev, P. Kop'ev. J Cryst Growth .184-185. (1998). 70-74

Chapter 6

Conclusions and Further work.

6.1 Introduction.

In the previous chapters the growth and characterisation of II-VI metastable sulphides have been presented. In this chapter the results are discussed and summarised. The growth of metastable sulphides is still of importance to the group at Heriot-Watt so future work that could further develop these materials is also discussed.

6.2 Chapter 3: (Zn,Mg)S/CrS multilayers.

6.2.1 Summary.

Initial studies into this material were motivated by the possibility that CrS would exhibit ferromagnetism with a high Curie temperature [1]. A Collaboration began in 2006 with the Polish Academy of Sciences (PAS) to investigate the magnetic properties of this material. It was suggested by the PAS that a thickness of 100Å was required in order to probe the samples magnetism accurately. The work presented in chapter 3 of this thesis is an attempt to satisfy the needs of the PAS.

The ability to grow ZB CrS arose from the previous successful demonstration of ZB MnS layers grown on GaAs substrates [2]. The lattice parameter for CrS was determined experimentally [3] and indicated that CrS would be lattice matched to GaP substrates. Initial studies on this substrate using ZnMgS/CrS structures showed promising results, with a possible 30Å of ZB CrS grown.

At the start of this thesis a succession of repeat growths was tried and characterized using XRI. It became apparent that, although initial simulations would fit the data, there

were differing simulations of equal merit that contained only ZnCrS layers with low Cr concentrations. Reasons for this were not easy to initially determine.

In an attempt to obtain better resolved interference fringes, thus a more unique simulation, a multilayer superlattice of ZnMgS/CrS was grown and characterised using XRI. The data collected from this experiment showed that small fluctuations in substrate temperature (derived from growth technique employed) changed the Mg mole fraction in ZnMgS enough to obscure any interference fringes. Subsequently samples of ZnS/CrS were grown in similar superlattice structures, but when these were examined using XRI still no resolvable interference pattern could be obtained. Both ZnMgS and ZnS superlattices were designed to contain the 100Å required by the PAS and on completion were sent for analysis (Results are still pending).

The remainder of the chapter investigated possible reasons why well resolved XRI spectra were unattainable with this material. XRD scans of the barrier layers were obtained and compared with simulations generated. Notable asymmetry in the XRD peak was observed which prevented the generation of a unique simulation. This appeared to be one of the contributory factors in the obscuring of the superlattice fringes. One of the crucial conditions for fringe formation is the similarity of upper and lower barrier layers in thickness, strain, and composition.

It was determined that the cause of the asymmetry in the XRD scans of ZnS and ZnMgS was non uniform layer relaxation which was inherent when using GaP substrates in a II-VI environment with no phosphorus source. The use of Zn to protect the substrate after heat clean has proved successful in other samples and is regularly used in the growth of ZnSe, CdSe, MgS and MnS on GaAs substrates. However the low growth temperatures required for this set of samples did not allow for this technique to prove successful.

6.2.2 Further work.

Recently, interest has revived in transition metal sulphides with strong sessions at the last international II-VI conference and an invited paper from Prof Heimbrodt (Philipps University Marburg) investigating lifetime decays in our MnS samples [4] This increased interest means it is imperative to resolve the problems mentioned in this section.

As the main source of difficulty stems from the initial substrate/epilayer interface it is clear that an investigation into the preservation of the substrate surface post heat clean is required. A few suggestions have been described in chapter 3 and will be summarised briefly here.

One solution may be to cap the substrate with a layer of As prior to entry into the II-VI chamber. This would allow for a low temperature heat clean and reduce the risk of excess phosphorus desorption. There are no reported studies using As capping on GaP and is not a facility currently available at Heriot-Watt so external collaborators would need to be found.

Alternatively passivation of the GaP using ammonium sulphide would protect the surface by depositing a monolayer of S on the surface. This again allows for a low temperature heat clean and reduces the risk of S attack on the surface. However previous studies have demonstrated that this technique is not reproducible as the ammoniumsulphide degrades with time [5].

6.3 Chapter 4: The MgS (100) surface.

6.3.1 Summary.

First grown by the HW MBE group in 2000 [6], MgS has been shown to be a versatile material and is an excellent barrier material for the confinement of exitons in low dimensional structures [7,8]. The solubility of MgS in HCl has allowed for the development of an epitaxial lift off technology that was first demonstrated by the HW MBE group. Chapter 4 of this thesis uses both AFM and RHEED to investigate the surface of MgS under different growth and annealing conditions.

There were two distinct experimental studies dealt with in this chapter. First RHEED measurements were taken, and then AFM topography scans were obtained.

The RHEED patterns from the MgS surfaces were observed during growth, annealing and both during and after irradiation with an Mg flux. A c(2x2) pattern is observed during MgS growth which was seen to be stable during annealing, but disappears with an impinging Mg flux. High temperature Mg irradiation creates a rough 1x1 surface. At lower temperatures the surface remains flat and a 4x1 reconstruction is observed with

Mg irradiation changing to a 2x1 on annealing *in situ*. These results are compatible with the c(2x2) surface being a ZnMgS alloy which converts to a pure MgS 4x1 on Mg irradiation. The conversion from 4x1 to 2x1 results from the evaporation of excess Mg. This was consistent with the work by Yang *et al* [9] and by observations of groups growing MgS using S_2 rather than compound ZnS [10].

The formation of 1D nanowires on MgS epitaxial layers was investigated using AFM. The wires were found to increase in size with increased ZnS flux or with increasing layer thickness. At low layer thicknesses it was seen that the distribution of wires is not uniform which is believed to be a reflection of the underlying dislocation density. At larger thicknesses the distribution becomes more uniform. Typical wire dimensions were on average 0.6μm (length), 900Å (width), and 20Å (height). Currently it is not feasible to determine absolutely the mechanism of formation of the wires, but it is consistent with the Asaro-Tiller-Grinfield instability arising from anisotropic strain in the MgS [11,12].

6.3.2 Future work.

There is still a large amount of information to be extracted from the MgS surface using RHEED, AFM and other characterisation techniques.

One of the major downfalls in the RHEED study was the inability to acquire measurements in real time. Also the resolution of the CCD was so poor that in some cases the measurements of the RHEED patterns were ambiguous due to the minimum resolvable pixel size. Improvements are in place, as a result of the work done in chapter 4, to replace the standered CCD camera with a high resolution webcam and to collect the data using Lab View. This has proven to be successful at other universities [13] so a new PhD student is currently setting up this experiment.

There is little more that can be obtained from the current AFM setup in order to determine the correct model for wire formation however by using reciprocal space mapping and TEM a more detailed study could be generated. However the work presented in Chapter 5 is an investigation into a direct replacement for MgS as a barrier material, so the necessity to determine the exact model for wire formation is now unnecessary.

6.4 Chapter 5: Growth and Characterisation of Mg rich ZnMgSSe.

6.4.1 Summary.

Previous research on ZnMgSSe focused on ZnSe rich alloys with Mg and S mole fractions ≤ 0.25. In chapter 5 by replicating the same growth technique used for MgS, ZnMgSSe alloys with Mg and S mole fractions ≥ 0.8 are be obtained. Characterisation of the MgS-rich alloy was obtained by XRI, TEM, AFM, and PL measurements. The successful incorporation of MgS-rich ZnMgSSe alloys into novel lift off structures is the final topic of discussion in chapter 5.

6.4.2 Conclusion.

Structures containing ZnMgSSe were designed for examination by XRI. Initial XRI simulations using a 5 layer model demonstrated alloys with a composition of $Zn_{0.20}Mg_{0.80}S_{0.64}Se_{0.36}$. Well defined and highly resolvable fringes indicated that the structure was single phase with well defined interfaces and little intermixing. This was confirmed using HRTEM with results showing little contrast change, single phase, and little or no intermixing. The use of AFM topography measurements also showed that the surface of the $Zn_{0.20}Mg_{0.80}S_{0.64}Se_{0.36}$ alloy was atomically flat. As the structural data at this point indicated that there was little intermixing, a second set of simulations were attempted using only a 3 layer model.

Better fits were obtained using a 3 layer model allowing a more accurate calculation of the growth rate which was found to be 1.5Å/s. The composition of the alloy remained constant between both the 5 and 3 layer models. Using the simulation software the individual ZnMgSSe layer was modelled to investigate any alternative solutions to the data. It was seen from the data that there was a unique solution and it was the $Zn_{0.20}Mg_{0.80}S_{0.64}Se_{0.36}$, which was consistent with optical absorption measurements.

PL measurements were used to confirm that this was a MgS-rich alloy by comparing the emission from a ZnSe QW with $Zn_{0.20}Mg_{0.80}S_{0.64}Se_{0.36}$ barriers to a similar structure with MgS barriers. It was seen that the confinement properties were almost identical between both structures indicating that the alloy must have a large MgS mole fraction.

With the alloy demonstrating similar confinement properties as MgS an investigation into the incorporation of the $Zn_{0.20}Mg_{0.80}S_{0.64}Se_{0.36}$ into an epitaxial lift off structure was undertaken. A lift off structure was generated using MgS as a sacrificial layer and $Zn_{0.20}Mg_{0.80}S_{0.64}Se_{0.36}$ as the barrier for a ZnSe QW. PL data was compared before and after lift off. It was seen that the PL emission from the QW remained similar after the sacrificial layer and substrate were removed with the emission having similar quantum efficiency and intensity. A change in strain state post lift off was observed by the transposition of the ZnSe HH and LH emission.

The determination of a unique composition for the ZnMgSSe allowed for the refinement of the upper bound for enthalpy of formation for MgS by ~1% while also allowing for a more accurate phase decomposition boundary to be determined. By looking at the growth rate of this material and comparing to ZnSe and MgS a measure of the accommodation coefficients for the alloys constituents could be obtained. It was found from this, based on the work by Sorokin *et al*, [14] that using the growth conditions mentioned in chapter 4 the accommodation coefficient for Mg in MgS is only 0.4.

6.4.3 Further work.

From the work presented in chapter 5 a transition is currently being made by the HW MBE group to replace standard MgS-containing structures with ZnMgSSe. The alloy has demonstrated better structural properties, oxide resistance, acid resistance, excellent confinement properties, and can be grown using the same growth conditions as MgS. Future work on this material will investigate the band gap and refractive index of the alloy for the production of several different device structures including a full polariton structure. The inclusion of this material as an emitter region between MgS barriers is a possibility; however its practical uses are limited so an investigation would be undertaken purely as interesting science.

6.5 References.

[1] T. Dietl, F. Matsukura, H. Ohno, Phys Rev B, 63, (2001), 195-205

[2] L. David, C. Bradford, X. Tang, T.C.M. Graham, K.A. Prior, B.C. Cavenett, J Cryst Growth, 251, (2003), 591–595

[3] L. David, K.A. Prior, Phys Stat Sol, 243, 4, (2006), 778–781

[4] W. Heimbrodt, L. Chen, H.A. Krug Von Nidda, A. Loidl, P.J. Klar, L. David, K.A. Prior, J Korean phys sol 53, 5, (2008), 2852-2856

[5] K. Prior, personal communication

[6] C. Bradford, C.B. O'Donnell, B. Urbaszek, A. Balocchi, C. Morhain, K.A. Prior and B.C. Cavenett, Appl. Phys. Lett, 76 (2000) 3929

[7] C. Bradford, C.B. O'Donnell, B. Urbaszek, A. Balocchi, C. Morhain, K.A. Prior, B.C. Cavenett, J Cryst Growth 227–228 (2001) 634–638

[8] C. Bradforda, B. Urbaszeka, M. Funato, A. Balocchia, T.C.M. Grahama, E.J. McGhee, R.J. Warburton, K.A. Prior, B. Cavenet. J of Cryst Growth 251 (2003) 581–585.

[9] Y.W. Zhang, Appl. Phys. Lett, 87 (2005) 121916

[10] R. Arians, T. Kümmell, G. Bacher, A. Gust, C. Kruse, D. Hommel, Appl. Phys. Lett, 90, (2007) 101-114.

[11] R.J. Asaro and W.A. Tiller, Metall. Trans., 3 (1972) 1789

[12] M.A. Grinfeld, Sov. Phys. Dokl, 31 (1986) 831

[13] Personal communication, Richard Campion, Nottingham University.

[14] S. Ivanov, S. Sorokin, I. Krestnikov, N. Faleev, B. Ber, I, Sedova, Yu Kudryavstev, P. Kop'ev. J Cryst Growth .184-185. (1998). 70-74